

## A Stochastic Model for Correlations between Central Black Hole Masses and Galactic Bulge Velocity Dispersions

V. I. Dokuchaev and Yu. N. Eroshenko\*

*Institute for Nuclear Research, Russian Academy of Sciences,  
pr. Shestidesyatiletiya Oktyabrya 7a, Moscow, 117312 Russia*

Received April 10, 2001; in final form July 5, 2001

**Abstract**—We consider a cosmological model in which part of the Universe,  $\Omega_h \sim 10^{-5}$ , is in the form of primordial black holes with masses of  $\sim 10^5 M_\odot$ . These primordial black holes were the centers for growing protogalaxies, which experienced multiple mergers with ordinary galaxies and with each other. The galaxy formation is accompanied by the merging and growth of central black holes in the galactic nuclei. We show that the recently discovered correlations between central black hole masses and galactic bulge parameters naturally arise in this scenario. © 2001 MAIK “Nauka/Interperiodica”.

Key words: *theoretical and observational cosmology*

### INTRODUCTION

Recent observations have shown that no less than 20% of the regular galaxies contain supermassive black holes (SMBHs) in their nuclei (Kormendy and Richstone 1995; Ho 1998). Various scenarios were proposed for the origin of the central SMBHs: (i) the gravitational instability and collapse of a supermassive star (e.g., Gurevich and Zybin 1990; Lipunova 1997); (ii) the collapse of a dynamically evolving dense star cluster (e.g., Rees 1984; Dokuchaev 1991); or (iii) the collapse of the central part of a massive gaseous disk (e.g., Eisenstein and Loeb 1995). In all these scenarios, the SMBHs are formed deep inside the gravitational potential well of galactic or protogalactic nuclei. A specific possibility is the formation of primordial SMBHs in the early Universe (Zel'dovich and Novikov 1967; Carr 1975).

Three types of correlations are observed between the mass of the central SMBH  $M_{BH}$  in a galactic nucleus and (i) the stellar mass of the galactic bulge  $M_b$  (Kormendy and Richstone 1995; Ho 1998),  $M_{BH} \simeq (0.003 - 0.006)M_b$ , (ii) the bulge luminosity  $L_B$  (Richstone 1998),  $M_{BH}/L_B \simeq 10^{-2} M_\odot/L_\odot$ , and (iii) the velocity dispersion  $\sigma_e$  at the bulge half-optical-radius (Gebhardt *et al.* 2000):

$$M_{BH} = 1.2(\pm 0.2) \times 10^8 \left( \frac{\sigma_e}{200 \text{ km s}^{-1}} \right)^{3.75(\pm 0.3)} M_\odot. \quad (1)$$

The correlations of types (i) and (ii) are indistinct, and there is a large scatter of data about the mean

values of  $M_{BH}$ . Therefore, recent observations are only consistent with correlations (i) and (ii), despite the absence of a proportionality between  $L_B$  and  $M_b$ . On the other hand, correlations (iii) are more definite.

The origin of the discussed correlations is quite uncertain. The simplest assumption that the growth of the SMBH mass depends on the bulge processes runs into the problem of different scales: the galactic bulge scale is several kpc, whereas the linear scale of the accretion disk around SMBHs is much less than 1 pc. Some deterministic mechanism is needed for a huge mass transfer from the bulge to its innermost part. Silk and Rees (1998) proposed a feasible solution of this problem by considering a self-adjusting accretion flow from the bulge under the radiation pressure on the early quasar phase of galactic evolution. However this model predicts a definite type of correlation,  $M_{BH} \propto \sigma_e^5$ , with the power index differing from the observed one.

The presumed primordial BHs are mixed with dark matter due to their cosmological origin. Therefore, the total mass of these BHs in any galaxy  $\sum M_h$  is proportional to the galactic dark matter halo mass  $M$ . As a result, the correlation  $\sum M_h \propto M$  is primary in this model, but the aforementioned observed correlations  $M_{BH} \propto M_b$ ,  $L$  and  $\sigma_e^\alpha$  are secondary and approximate in origin due to the complex process of galactic formation. We show below that the required relation  $M_{BH} \propto \sigma_e^\alpha$  with a power index  $\alpha$  close to the observed one follows from our primary relation  $\sum M_h \propto M$  with the value of  $\sigma_e$  determined by the dark matter halo mass  $M$ . The model considered

\*E-mail: [erosh@ns.ufn.ru](mailto:erosh@ns.ufn.ru)

also reproduces the correlation  $M_{BH} \propto M_b$  but with a lower accuracy.

Another necessary requirement of our model is the multiple merging of primordial BHs with mass  $M_h$  into a single SMBH with mass  $M_{BH}$  in the Hubble time. In Section 4, we justify this requirement. It is well known that for a single BH with mass  $M_h \ll 10^7 M_\odot$ , the dynamical friction in the galactic halo is ineffective (Valtaoja and Valtonen 1989). Nevertheless, for the early formed primordial BHs, the process of dark matter secondary accretion is possible. As a result, the primordial BHs are enveloped by a dark matter halo with the mass of a typical dwarf galaxy and a steep density profile,  $\rho \propto r^{-9/4}$ . Indeed, the gravitationally bound objects formed at redshifts  $z \sim 10$  from the density fluctuations  $\delta \sim 10^{-3}$  (at the recombination epoch). In a homogeneous Universe, BHs with mass  $M_h \sim 10^5 M_\odot$  produce this fluctuation inside a sphere containing the total mass  $M_h/\delta \sim 10^8 M_\odot$ . We will call this combined spherical volume BH +halo an induced halo. The characteristics of these induced halos are defined in Sections 2 and 3. Our assumption of the multiple merging of primordial BHs may break down in galaxies of the late Hubble types. In fact, observations (Zalucci *et al.* 1998) show that the masses of the central BHs in these galaxies are less than in the E and S0 galaxies, and there are no correlations (i)—(iii).

Here, we consider for simplicity a flat cosmological model without the cosmological constant. We use the subscript *i* for quantities at the time  $t_i \simeq 6 \times 10^{10}$  s of the transition from a radiation dominated to a matter (dust) dominated phase. The subscript 0 is used for quantities at the recent time  $t_0$ . We call all BHs existing at the recombination epoch the primordial ones. The other possible mechanisms of BH formation are important only in Section 2. We use the term bulge both for elliptical galaxies and for the central spheroidal parts of spiral galaxies that resemble dwarf ellipticals.

## 1. PRIMORDIAL BLACK HOLES

Noncompact objects (NCOs) of the mass  $\sim (0.1-1)M_\odot$  composed of weakly interacting nonbaryonic dark matter particles such as neutralinos were proposed by Gurevich *et al.* (1997) to explain microlensing events in the Large Magellanic Clouds (Alcock *et al.* 2000). The hypothesized NCOs or neutralino stars originate from the cosmological fluctuations with a narrow sharp maximum  $\sim 1$  in the spectrum on some small scale. In addition to neutralino stars, the same maximum in the spectrum of cosmological fluctuations also produces massive primordial BHs with the mass  $\sim 10^5 M_\odot$  (Dokuchaev

and Eroshenko 2002). Therefore, the hypothesized dark matter NCO and primordial BHs may be indirectly associated with their common origin from the same cosmological fluctuations. The spectrum with a sharp maximum on some scale arises in some inflationary models (Starobinsky 1992; Ivanov *et al.* 1994; Yokoyama 1995; Garcia-Bellido 1996). At the same time, the spectrum beyond the maximum may be of the standard Harrison-Zel'dovich form and reproduces the ordinary scenario for the large-scale structure formation in the galactic distribution.

Adiabatic density fluctuations of matter on a scale smaller than the horizon grow logarithmically with time at the radiation-dominated epoch. These fluctuations with amplitude  $\delta_i \sim 1$  at the time  $t_i$  correspond to radiation density fluctuations  $\sim 0.05$  at the time  $t_h$  when the disturbed region goes under the horizon (Dokuchaev and Eroshenko 2002). Therefore, large fluctuations at the radiation-dominated epoch produce BHs near the time  $t_h$  (Zel'dovich and Novikov 1967; Carr 1975).

BHs are formed at the tail of the Gaussian fluctuation distribution, whereas most NCO are formed from the rms fluctuations. Therefore, only a small fraction of the fluctuations which result in the formation of NCO can produce BHs at the radiation-domination epoch. In other words, due to the large threshold of BH formation, most fluctuations do not collapse into BHs and evolve continuously up to the end of the radiation-dominated epoch. At the radiation-dominated epoch, the mass in the comoving volume varies as  $M(t) = M_x a(t_i)/a(t)$ , where the scale factor of the Universe  $a \propto t^{1/2}$  and  $M_x$  is the comoving mass at the time of transition to the matter domination. The mass  $M_x$  is approximately equal to the mass of nonrelativistic matter inside the fluctuation, i.e., the mass of NCO that can be formed from this fluctuation. On the other hand,

$$M(t) = \frac{4\pi}{3}(2ct)^3 \rho(t), \quad (2)$$

where  $\rho(t) = 3/32\pi Gt^2$ . From these relations for  $M(t)$ , we derive the BH formation time  $t_h$  and mass  $M_h$  as a function the NCO mass

$$t_h = (M_x G)^{2/3} c^{-2} t_i^{1/3} \quad (3)$$

$$= 1.1 \left( \frac{M_x}{M_\odot} \right)^{2/3} \left( \frac{t_i}{6 \times 10^{10} \text{ s}} \right)^{1/3} \text{ s},$$

$$M_h = c M_x^{2/3} G^{-1/3} t_i^{1/3} \quad (4)$$

$$= 2.3 \times 10^5 \left( \frac{M_x}{M_\odot} \right)^{2/3} \left( \frac{t_i}{6 \times 10^{10} \text{ s}} \right)^{1/3} M_\odot.$$

In our model, the NCOs and BHs originate from fluctuations of the same type but at a different time. Whereas the large difference in the masses of NCOs

and BHs is accounted for by the mass variation with time inside the fixed comoving volume: the mass of the radiation at the radiation-dominated epoch (e.g., at  $t \sim 1$  s) far exceeds the cold dark matter mass at the matter-dominated epoch in the same comoving volume.

There are definite astrophysical limitations on the number and mass of primordial BHs. (1) It follows from the Universe age limit that the fraction of BHs is  $\Omega_h \leq 1$ . In addition, PBHs with  $\Omega_h \sim 1$  would disturb the microwave background spectrum if they were formed  $\sim 1$  s after electron–positron pair annihilations (Carr 1975). (2) The possibility of the tidal destruction of globular clusters by primordial BHs gives a BH mass limit  $M_h \leq 10^4 M_\odot$  if these BHs mainly contribute to the dark matter (Moore 1993). (3) Model-dependent calculations of the contribution from matter accretion by PBHs at the pre-galactic and recent epochs to the background radiation give approximately  $\Omega_h \leq 10^{-3} \div 10^{-1}$  for  $M_h \sim 10^5 M_\odot$  (Carr 1979). (4) The absence of reliable gamma-ray burst (GRB) lensing events yielded a limit  $\Omega_h < 0.1$  for PBHs in the intergalactic medium with masses  $10^5 M_\odot < M_h < 10^9 M_\odot$  (Nemiroff *et al.* 2001). An even more stringent limit  $\Omega_h < 0.01$  for  $10^6 M_\odot < M_h < 10^8 M_\odot$  is obtained from VLBI observations of the lensing of compact radio sources (Wilkinson *et al.* 2001).

In this paper, we consider the case  $\Omega_h \sim 10^{-5}$  where none of the above constraints breaks down.

## 2. THE FORMATION OF AN INDUCED HALO

A massive induced halo (IH) or a heavy dark matter envelope around a PBH is formed due to dark matter accretion in an expanding Universe. Spherical matter accretion onto a compact object (an SMBH or a galaxy) produces a stationary matter density profile of the form  $\rho \propto r^{-9/4}$  (e.g., Ryan 1972; Gunn 1977). Here, we reproduce similar calculations in a form suitable for relating the PBH mass to the mass of gravitationally trapped matter and the corresponding redshift.

The matter in a spherical layer of radius  $r$  around a PBH in a homogeneous Universe undergoes the acceleration

$$\frac{d^2 r}{dt^2} = -\frac{G}{r^2} (M_h + \frac{4\pi}{3} r_i^3 \rho_i), \quad (5)$$

where  $r_i$  and  $\rho_i = 4.4 \times 10^{-18} (h/0.6)^8 \text{ g cm}^{-3}$  are, respectively, the radius of the spherical layer and the Universe density at time  $t_i$  when a large growth of fluctuations begins; and  $h$  is the Hubble constant in units of  $100 \text{ km s}^{-1} \text{ Mpc}^{-1}$ . Let us multiply Eq. (5) by

$db/dt$  and integrate it using the normalization  $r(t) = r_i b(r_i, t)$  and the initial condition  $b(t_i) = 1, \dot{b}(t_i) = H(t_i)b$ . Let us introduce also the normalization  $\tau = (t - t_i)\alpha^{1/2}$ , where

$$\alpha = \left( \frac{2GM_h}{r_i^3} + \frac{8\pi G}{3} \rho_i \right), \quad (6)$$

the integrated Eq. (5) then takes the form

$$b(db/d\tau)^2 = 1 - bE, \quad (7)$$

with  $E \equiv (\alpha - H^2(t_i))/\alpha$ . An equation of this type admits an exact solution (Saslaw 1989). From this solution, we derive the expansion termination time of the layer under consideration

$$t_s \approx \frac{3\pi}{4} t_i \left( \frac{M_s}{M_h} \right)^{3/2}. \quad (8)$$

Here,  $M_s = 4\pi\rho_i r_i^3/3$  is the mass inside the layer except for the central PBH mass. At the time of expansion termination  $b(t_s) = 1/E$  and, subsequently, the layer contracts until  $t_{\text{col}} \approx 2t_s$ . From (8) using the relation  $t = t_0/(1+z)^{3/2}$  for a flat Universe without the cosmological constant, we obtain

$$z_{\text{col}} \approx 0.36 z_i \frac{M_h}{M_s} - 1 \approx 2 \times 10^3 \frac{M_h}{M_s} - 1, \quad (9)$$

where  $z_i = 2.4 \times 10^4 h^2$ .

We assume that the spherical layer is detached from the cosmological expansion and virialized and after its expansion termination and the subsequent contraction from radius  $r_i b(r_i, t_s)$  to radius  $r_{\text{col}} = r_i b(r_i, t_s)/2$ . For this virialization radius of the IH around the central PBH, we find

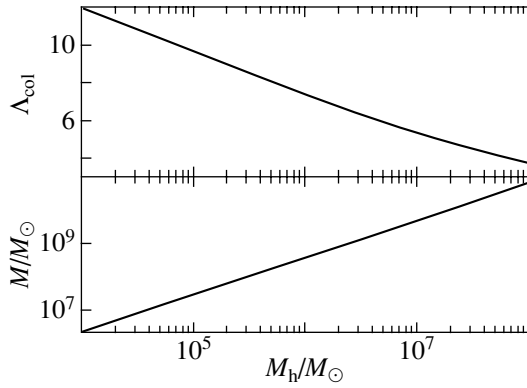
$$\begin{aligned} r_{\text{col}} &= \frac{r_i}{2E} = \frac{M_s^{4/3}}{2M_h} \left( \frac{3}{4\pi\rho_i} \right)^{1/3} \\ &= 0.45 \left( \frac{M_h}{10^5 M_\odot} \right)^{1/3} \left( \frac{15}{1+z_{\text{col}}} \right)^{4/3} \text{ kpc}, \end{aligned} \quad (10)$$

hence, we derive the required relation for the IH mass and radius

$$\begin{aligned} M_s(r_{\text{col}}) &= (2M_h r_{\text{col}})^{3/4} \left( \frac{4\pi\rho_i}{3} \right)^{1/4} \\ &= 3.7 \times 10^7 \left( \frac{M_h}{10^5 M_\odot} \right)^{3/4} \left( \frac{r_{\text{col}}}{1 \text{ kpc}} \right)^{3/4} \left( \frac{h}{0.6} \right)^2 M_\odot \end{aligned} \quad (11)$$

and the density distribution in the IH

$$\begin{aligned} \rho(r) &= \frac{1}{4\pi r^2} \frac{dM_s(r)}{dr} = 1.7 \times 10^{-25} \left( \frac{M_h}{10^5 M_\odot} \right)^{3/4} \\ &\times \left( \frac{r}{1 \text{ kpc}} \right)^{-9/4} \left( \frac{h}{0.6} \right)^2 \text{ g cm}^{-3}. \end{aligned} \quad (12)$$



The dependences  $z_{\text{col}}(M_h)$  and  $M(M_h)$  derived by solving the system of equations (17) and (19).

### 3. PROTOGALAXY GROWTH TERMINATION

The growth of IH terminates at the epoch of the nonlinear growth of ambient density fluctuations with mass  $M$  and radius  $R$  producing the same gravitational acceleration:

$$g = \frac{GM_s(r_{\text{col}})}{(2R_{\text{col}})^2} = \frac{GM}{(2R)^2}, \quad (13)$$

where the radii  $2r_{\text{col}}$  and  $2R$  correspond to the time of expansion termination. Under this condition, the capture of new spherical layers ceases [see (10)].

The rms fluctuation on the mass scale  $M$  is given by (Barden *et al.* 1986)

$$\sigma^2(M, z) = \frac{1}{2\pi^2(1+z)^2} \int dk k^2 P_0(k) W^2(k, M), \quad (14)$$

Here,  $W(k, M)$  is the filtering function and  $P(k)$  is the power spectrum

$$\langle \delta_k^* \delta_{k'} \rangle = (2\pi)^3 P(k) \delta_D^{(3)}(k - k'), \quad (15)$$

$$\delta_k = \int \delta(r) e^{ikr} d^3r,$$

where  $\delta_D^{(3)}(k - k')$  is the Dirac delta-function and the angular brackets denote an ensemble averaging. Let us choose  $P_0(k)$  for the model with cold dark matter (Barden *et al.* 1986) with the Harrison-Zel'dovich initial spectrum

$$P_0(k) = \frac{ak \ln^2(1 + 2.34q)}{(2.34q)^2} (1 + 3.89q + (16.1q)^2 + (5.46q)^3 + (6.71q)^4)^{-1/2}, \quad (16)$$

where  $q = k\Omega_d^{-1}h^{-2}$  is written in comoving coordinates with units  $\text{Mpc}^{-1}$ . For simplicity, we take the dark matter density parameter  $\Omega_d = 1$ . The normalization constant  $a$  is chosen from the condition

$\sigma_0 = 1$  on the scale  $8h^{-1} \text{ Mpc}$ . The condition for the formation of an object with mass  $M$  at redshift  $z_{\text{col}}$  is

$$\sigma(M, z_{\text{col}}) = \delta_c, \quad (17)$$

where for the model of spherical contraction  $\delta_c = 3(3\pi/2)^{2/3}/5$  (White 1994). The radius of an ordinary protogalaxy (without PBH) after its cosmological expansion termination and virialization is (Saslaw 1989; White 1994)

$$R = \frac{3R_i}{10\delta_i}, \quad R_i = \left( \frac{3M}{4\pi\rho_i} \right)^{1/3}. \quad (18)$$

Given (10), (17), and (18) and assuming  $\delta_i = \sigma_i(M)$ , condition (13) can be rewritten as

$$M = \left( \frac{3\pi}{2} \right)^{10/3} \left( \frac{3}{5} \right)^6 \frac{(1+z_i)}{(1+z_{\text{col}})} M_h \delta_c^{-6}. \quad (19)$$

It follows that  $M_s = M$ , because in (10) and (18), we assume that IHs and ordinary protogalaxies have the same coefficient of nonlinear contraction, 0.5. We solve numerically the system of equations (17) and (19) for the independent variables  $z_{\text{col}}$  and  $M$  with  $M_h$  as a parameter. Figure 1 shows the dependences  $z_{\text{col}}(M_h)$  and  $M(M_h) = M_s(M_h)$ . For  $M_h = 2.3 \times 10^5 M_\odot$  we find  $z_{\text{col}} = 8.8$  and  $M = 7.2 \times 10^7 M_\odot$ . As a result, up to the epoch  $z = 8.8$ , the PBHs with mass  $M_h = 2.3 \times 10^5 M_\odot$  had time to capture an additional mass, which is a factor of  $\sim 300$  larger than the PBH mass.

### 4. MERGING OF BLACK HOLES

In the preceding section, we showed that massive IHs with the mass  $M_s = 7.2 \times 10^7 M_\odot$  are formed around PBHs. These IHs are massive enough to sink to the galactic center in the Hubble time under the effect of dynamical friction. However, the fate of nested PBHs inside the central parsec of the host galaxy is unclear. Valtaoja and Valtonen (1989) considered the interaction of central BHs after the merging of galaxies. The late phase of two BHs merging in the galactic center depends on many factors (Menou *et al.* 2001). Without a detailed elaboration, we will follow Menou *et al.* (2001) by assuming that multiple PBHs merge into a single SMBH in the Hubble time.

Note that the density (12) dramatically grows toward the center and is smoothed out only at the distance  $r_h$  where  $M_s = M_h$ , as follows from (11). For  $M_h = 2.3 \cdot 10^5 M_\odot$ , we find  $r_h \sim 1 \text{ pc}$  and a density  $\rho \sim 10^4 M_\odot \text{ pc}^{-3}$ . By using the Chandrasekhar time for dynamical friction (see, e.g., Saslaw 1989) of a PBH with mass  $M_h = 2.3 \times 10^5 M_\odot$ , we obtain an estimate of the characteristic time for PBH merging  $M_h = 2.3 \times 10^5 M_\odot$ :

$$t_f \sim \frac{v^3}{4\pi G^2 \Lambda_B \rho M_h} \sim 5 \times 10^5 \text{ years}, \quad (20)$$

where  $v \sim (GM_h/r_h)^{1/2}$  is the PBH velocity,  $\Lambda \approx 10$ , and  $B \approx 0.426$ . A more massive PBH would merge even faster. As a result, the late phase of PBHs merging is very quick, and the probability of the simultaneous presence in the galactic nucleus of three or more BHs is low.

The merging of PBHs in galaxies must be accompanied by a strong burst of gravitational radiation. The LISA interferometric detector is capable of detecting merging events up to redshifts  $z \sim 10$  if the BH masses are no less than  $10^3 M_\odot$  (Menou *et al.* 2001). For the gravitational burst distribution to be calculated, hierarchical BHs and galactic merging must be numerically simulated. Menou *et al.* (2001) carried out such simulations for ordinary galaxies. The burst rate from the observable Universe is estimated to be

$$\dot{N}_{\text{grav}} \sim \frac{4\pi}{3} (ct_0)^3 n_g \frac{N}{t_0} \sim 10 \left( \frac{n_g}{10^{-2} \text{Mpc}^{-3}} \right) \times \left( \frac{t_0}{10^{10} \text{years}} \right)^2 \left( \frac{N}{100} \right) \text{year}^{-1}, \quad (21)$$

where  $n_g$  is the mean number density of structured galaxies and  $N$  is the mean number of mergings per galaxy. So, there is a principal possibility for the verification of the model under consideration by the LISA detector.

### 5. THE ORIGIN OF CORRELATIONS

The fluctuation spectrum (16) in a limited mass range can be fitted by a power law with the effective index  $n = d \ln P_0(k) / d \ln k$ . According to the formation condition (17) for a power-law spectrum, the effective galactic mass formed at redshift  $z$  is (White 1994)

$$M = M_0(1+z)^{-\frac{6}{n+3}}, \quad (22)$$

where  $M_0 = \text{const}$ . For the galactic mass  $M = 10^{10} M_\odot$ , we obtain  $n = -2.28$  and  $M_0 = 2.5 \times 10^{16} M_\odot$ ; for  $M = 10^{12} M_\odot$ , we find, respectively,  $n = -1.98$  and  $M_0 = 7 \times 10^{14} M_\odot$ . The velocity dispersion is estimated as

$$\sigma_e^2 \simeq \frac{GM}{R}, \quad R = \left( \frac{3M}{4\pi\rho(z)} \right)^{1/3}, \quad (23)$$

$$\rho(z) = \rho_0(1+z)^3.$$

For the PBH cosmological density parameter  $\Omega_h$  and effective PBH merging in galaxies, the preceding relation gives the final mass of the central BH

$$M_{\text{BH}} = \psi \Omega_h M = \psi \Omega_h \sigma_e^{\frac{12}{1-n}} M_0^{-\frac{n+3}{1-n}} \left( \frac{4\pi G^3 \rho_0}{3} \right)^{-\frac{2}{1-n}}, \quad (24)$$

where the factor  $\psi$  allows for the possible additional growth of the central BH via accretion. From (24) with  $h = 0.6$ , we have

$$M_{\text{BH}} = (1.1 - 1.7) \times 10^8 \left( \frac{\psi \Omega_h}{10^{-5}} \right) \times \left( \frac{\sigma_e}{200 \text{ km s}^{-1}} \right)^{(3.66-4.03)} M_\odot, \quad (25)$$

where the coefficients 1.1 and 3.66 correspond to  $M = 10^{10} M_\odot$ , and the coefficients 1.7 and 4.03 correspond to  $M = 10^{12} M_\odot$ . Thus, the model considered is in good agreement with the observational data (1). The fluctuation spectrum on the galactic scale,  $n \approx -2$ , completely determined the power index  $\alpha \approx 4$  in the relation  $M_{\text{BH}} \propto \sigma_e^\alpha$ . It is easy to verify that for  $\Omega_h \sim 10^{-5}$ , the contribution of IHs [their mass is determined in section (3)] to the total galactic mass is negligible.

A correlation of the form  $M_{\text{BH}} \propto M_b$  is explained by the common relation of dark matter mass in galaxies of all types with their total baryonic (star) mass with the main input from old stars. In the hierarchical model of galaxy formation, recent galaxies formed from the multiple merging of low-mass protogalaxies with on-going early star formation. In this case, the old star population of the spherical subsystem is protogalactic in origin.

The part of the galactic mass contained in stars becomes a fixed and independent part of the total galactic mass  $M$  due to the statistical averaging after a large number of protogalactic mergings. So, the total star mass in the galaxy is  $M_b = f_b f_s M$ , where  $f_b \approx 0.05$  is the baryonic mass fraction of the Universe,  $f_s$  is the fraction of baryons passing into stars. After sinking to the galactic center and the merging of all PBH, the resulting BH mass is

$$M_{\text{BH}} \simeq \frac{\psi \Omega_h}{f_b f_s} M_b \simeq 10^{-3} \left( \frac{\psi \Omega_h}{10^{-5}} \right) \left( \frac{f_b f_s}{0.01} \right)^{-1} M_b, \quad (26)$$

which, in order of magnitude, corresponds to observations  $M_{\text{BH}} \simeq (0.003 - 0.006) M_b$ .

The central BH masses in Sa, Sb, Sc galaxies are, on the average, smaller than those in E and S0 galaxies (Salucci *et al.* 1998). In our model, this is attributable to the relatively late formation of the Sa, Sb, Sc galaxies when most of the PBHs did not have enough time to sink to the galactic center. In particular,  $\sim 10^2$  PBHs of mass  $M_h \sim 10^5 M_\odot$  can inhabit our Galaxy.

## 6. CONCLUSIONS

We explain the observed correlations between bulge parameters and central BH masses in galaxies by the multiple merging of PBHs of mass  $\sim 10^5 M_\odot$  generated in the early Universe. This model predicts the existence of BHs with mass  $\sim 10^5 M_\odot$  beyond the dynamical centers of spiral galaxies and in the intergalactic medium. One of these BHs may have been detected by the Chandra Observatory in the galaxy M 82 (Kaaret *et al.* 2000). An observational signature for the verification of this model is a gravitational burst after BH merging in the galactic nuclei which can be detected by LISA-type laser interferometric detectors.

## ACKNOWLEDGMENTS

This work was supported in part by the INTAS (grant no. 99-1065) and the Russian Foundation for Basic Research (project nos. 01-02-17829, 00-15-96697 and 00-15-96632). We also wish to thank the referees for helpful remarks.

## REFERENCES

1. C. Alcock, R. A. Allsman, D. R. Alves, *et al.*, *Astrophys. J.* **542**, 281 (2000).
2. J. M. Barden, J. R. Bond, N. Kaiser, and A. S. Szalay, *Astrophys. J.* **304**, 15 (1986).
3. B. J. Carr, *Astrophys. J.* **201**, 1 (1975).
4. B. J. Carr, *Mon. Not. R. Astron. Soc.* **189**, 123 (1979).
5. V. I. Dokuchaev, *Usp. Fiz. Nauk* **161**, 1 (1991) [*Sov. Phys. Usp.* **34**, 447 (1991)].
6. V. I. Dokuchaev and Yu. N. Eroshenko, *Zh. Éksp. Teor. Fiz.* (2002) (in press).
7. D. J. Eisenstein and A. Loeb, *Astrophys. J.* **443**, 11 (1995).
8. M. Fukugita and E. L. Turner, *Astrophys. J. Lett.* **460**, L81 (1996).
9. J. Garcia-Bellido, A. Linde, and D. Wands, *Phys. Rev. D* **54**, 6040 (1996).
10. K. Gebhardt, R. Bender, G. Bower, *et al.*, *Astrophys. J. Lett.* **539**, L13 (2000).
11. J. E. Gunn, *Astrophys. J.* **218**, 592 (1977).
12. A. V. Gurevich and K. P. Zybin, *Zh. Éksp. Teor. Fiz.* **97**, 20 (1990) [*Sov. Phys. JETP* **70**, 10 (1990)].
13. A. V. Gurevich, K. P. Zybin, and V. A. Sirota, *Usp. Fiz. Nauk* **167**, 913 (1997) [*Phys. Usp.* **40**, 869 (1997)].
14. L. C. Ho, astro-ph/9803307 (1998).
15. P. Ivanov, P. Naselsky, and I. Novikov, *Phys. Rev. D* **50** (12), 7173 (1994).
16. P. Kaaret, A. H. Prestwich, A. Zezas, *et al.*, astro-ph/0009211 (2000).
17. J. Kormendy and D. Richstone, *Annu. Rev. Astron. Astrophys.* **33**, 581 (1995).
18. G. V. Lipunova, *Pis'ma Astron. Zh.* **23**, 104 (1997) [*Astron. Lett.* **23**, 84 (1997)].
19. K. Menou, Z. Haiman, and V. K. Narayanan, astro-ph/0101196 (2001).
20. B. Moore, *Astrophys. J. Lett.* **413**, L93 (1993).
21. R. J. Nemiroff, G. F. Marani, J. P. Norris, and J. T. Bonnel, *Phys. Rev. Lett.* **86**, 580 (2001).
22. D. Richstone, astro-ph/9810379 (1998).
23. M. P. Ryan, Jr., *Astrophys. J. Lett.* **177**, L79 (1972).
24. P. Salucci, C. Ratnam, P. Monaco, and L. Danese, astro-ph/9812485 (1998).
25. W. C. Saslaw, *Gravitational Physics of Stellar and Galactic Systems* (Cambridge Univ. Press, Cambridge, 1985; Mir, Moscow, 1989).
26. J. Silk and M. J. Rees, astro-ph/9801013 (1998).
27. A. A. Starobinskii, *Pis'ma Zh. Éksp. Teor. Fiz.* **55**, 477 (1992) [*JETP Lett.* **55**, 489 (1992)].
28. L. Valtaoja and M. J. Valtonen, *Astrophys. J.* **343**, 47 (1989).
29. S. D. M. White, astro-ph/9410043 (1994).
30. P. N. Wilkinson, D. R. Henstock, I. W. A. Browne, *et al.*, *Phys. Rev. Lett.* **86**, 584 (2001).
31. J. Yokoyama, astro-ph/9509027 (1995).
32. Ya. B. Zel'dovich and I. D. Novikov, *Astron. Zh.* **43**, 758 (1966) [*Sov. Astron.* **10**, 602 (1967)].

*Translated by Yu. Eroshenko*

## The Bulk Motion of Flat Galaxies on Scales of 100 Mpc in the Quadrupole and Octupole Approximations

S. L. Parnovsky<sup>1\*</sup>, Yu. N. Kudrya<sup>1</sup>, V. E. Karachentseva<sup>1</sup>, and I. D. Karachentsev<sup>2</sup>

<sup>1</sup>*Astronomical Observatory, Kiev National University, ul. Observatornaya 3, Kiev, 04053 Ukraine*

<sup>2</sup>*Special Astrophysical Observatory, Russian Academy of Sciences,  
pos. Nizhnii Arkhyz, Karachai-Cherkessia, Russia*

Received July 13, 2001

**Abstract**—The peculiarities of non-Hubble bulk motions of galaxies are studied by analyzing a sample of 1271 thin edge-on spirals with distances determined using a multiparametric Tully–Fisher relation that includes the amplitude of the galaxy rotation, the blue and red diameters, surface brightness, and morphological type. In the purely dipole approximation, the bulk motion of galaxies relative to the cosmic microwave background frame can be described by the velocity of  $336 \pm 96 \text{ km s}^{-1}$  in the direction  $l = 321^\circ$ ,  $b = -1^\circ$  within radius  $R_{\text{max}} = 10000 \text{ km s}^{-1}$ . An analysis of more complex velocity field models shows that the anisotropy of the Hubble expansion described by the quadrupole term is equal to  $\sim 5\%$  on scale lengths  $R_{\text{max}} = 6000 - 10000 \text{ km s}^{-1}$ . The amplitude within the Local Supercluster ( $R_{\text{max}} = 3000 \text{ km s}^{-1}$ ) is as high as  $\sim 20\%$ . The inclusion of the octupole component reduces the dipole amplitude to  $134 \pm 111 \text{ km s}^{-1}$  on scale lengths of  $\sim 8000 \text{ km s}^{-1}$ . The most remarkable feature of the galaxy velocity field within  $R_{\text{max}} = 8000 \text{ km s}^{-1}$  is the zone of minimum centered on  $l = 80^\circ$ ,  $b = 0^\circ$  (the constellation of Cygnus) whose amplitude reaches 18% of the mean Hubble velocity. © 2001 MAIK “Nauka/Interperiodica”.

Key words: *galaxies, large-scale motions*

### INTRODUCTION

Analyses of non-Hubble motions and of the velocity field of galaxies on various scale lengths require extensive galaxy samples with measured radial velocities  $V_h$  and redshift-independent distance estimates. The RFGC catalog of flat galaxies (Karachentsev *et al.* 1999) constitutes a homogeneous sample of 4236 edge-on spirals providing rather uniform coverage of the entire sky. Starting with the first version of FGC (Karachentsev *et al.* 1993), we carried out our own observations and compiled published radial-velocity and HI line width data for the galaxies in our catalog. In 1995 we estimated the absolute velocity and apex of the bulk motion of flat galaxies in the dipole approximation to be  $V = 260 \text{ km s}^{-1}$ ,  $l = 319^\circ$ ,  $b = +28^\circ$  based on observational data for about 800 FGC galaxies and the direct Tully–Fisher relation (Karachentsev *et al.* 1995). At the next stage (Karachentsev *et al.* 2000a), we used a generalized multiparametric Tully–Fisher relation to estimate redshift-independent distances to about 1000 flat galaxies, and inferred the parameters of the dipole solution for the bulk motion  $V = 300 \text{ km s}^{-1}$ ,  $l =$

$328^\circ$ , and  $b = +7^\circ$ , in good agreement with the results obtained for the entire MarkIII catalog:  $V = 370 \text{ km s}^{-1}$ ,  $l = 305^\circ$ , and  $b = +14^\circ$  (Dekel *et al.* 1999).

As of now, we have compiled observed radial velocities and HI widths for a total of  $\sim 1300$  RFGC galaxies (Karachentsev *et al.* 2000b), which we used in this paper to determine the parameters of the bulk motion of flat galaxies. We determined galaxy distances using a different form of relation from that adopted by Karachentsev *et al.* (2000b), and considered various approximations for bulk motion: simple dipole (D), quadrupole (DQ), and octupole (DQO) models.

Two groups of discrepant results are known concerning the characteristic velocities relative to the cosmic microwave background (the so-called 3K-frame) either equal to 400–700  $\text{km s}^{-1}$  or close to zero [Strauss and Willik 1995; Willik and Strauss 1998; Willik 2000]. We decided to analyze the effect of high-order multipole terms using the sample of flat galaxies as an example. We show below that the inclusion of the octupole term can substantially reduce the magnitude of the dipole velocity term for galaxies with  $cz > 7000 \text{ km s}^{-1}$ .

\*E-mail: par@observ.univ.kiev.ua

The role of the quadrupole component in the models of galaxy bulk motion was first discussed by Lilje *et al.* (1986) in their pioneering work and then by a number of other authors (Staveley-Smith and Davies 1989; Dekel 1994; Willik *et al.* 1997; Willik and Strauss 1998; Dekel *et al.* 1999; Hoffman *et al.* 2001). The quadrupole term is interpreted as the tidal component of the bulk velocity field due to the galaxies that are external to the sample considered. The estimates of the parameters of the quadrupole term reported in some of the works mentioned above point to its important role in the description of the dynamics of galaxy streams. As far as we know, no numerical estimates of the octupole term have been published so far.

## MULTIPOLE EXPANSION OF THE GALAXY BULK VELOCITY FIELD

### *Model of Bulk Velocity*

Let us assume that the field of velocity vector  $\mathbf{V}$  of bulk motion for the galaxy ensemble considered is a continuous analytic function of the radius-vector  $\mathbf{r} = r\mathbf{n}$  drawn from the observing point to the point at a distance  $r$  in the direction of unit vector  $\mathbf{n}$ . Let us expand  $\mathbf{V}$  in powers of Cartesian coordinates  $\mathbf{r} = \{x_1, x_2, x_3\}$  and limit our analysis to the first three terms of the expansion

$$V_i = D_i + A_{ij}x_j + B_{ijk}x_jx_k \quad (1)$$

(hereafter, summation is taken over repeated indices). Galaxy redshift observations give only the radial component of velocity (1)

$$V_r \equiv V_i n_i = D_i n_i + r A_{ij} n_i n_j + r^2 B_{ijk} n_i n_j n_k. \quad (2)$$

It is evident from this that tensors  $\mathbf{A}$  and  $\mathbf{B}$  can be considered symmetric with respect to their indices, thus implying the potentiality of the velocity field. Let us now decompose tensor  $\mathbf{A}$  into a sum of traceless tensor  $\mathbf{Q}$  and a tensor proportional to the unity tensor

$$A_{ij} = Q_{ij} + H\delta_{ij}, \quad H = \frac{1}{3}A_{ij}\delta_{ij}. \quad (3)$$

We then similarly decompose the third-order tensor  $\mathbf{B}$  into a traceless component  $\mathbf{O}$  and the component containing its vector trace  $\mathbf{P}$

$$B_{ijk} = O_{ijk} + P_i\delta_{jk}, \quad P_i = \frac{3}{5}B_{ijk}\delta_{jk} \quad (4)$$

(here indices in brackets are symmetrized). Substitution of formulas (3) and (4) into formula (2) yields the following model of galaxy bulk velocity field:

$$V_r = Hr + D_i n_i + r^2 P_i n_i + r Q_{ij} n_i n_j + r^2 O_{ijk} n_i n_j n_k. \quad (5)$$

### *The Physical Meaning of Individual Motion Components*

We now assume that  $V_r$  values in formula (5) are radial velocities of galaxies inferred from their observed redshifts  $z$  and reduced to the 3K reference frame according to Kogut *et al.* (1993). Relation (5) is a generalization of the Hubble law. The first term corresponds to the Hubble expansion with the Hubble constant  $H$ . The remaining terms in formula (5) determine the deviation from the Hubble law—the so-called non-Hubble bulk motions. The second term corresponds to the dipole approximation of this motion, i.e., to the averaged bulk motion of all galaxies at a constant velocity  $\mathbf{D}$  relative to the adopted 3K reference frame.

Hereafter, we refer to the model of galaxy velocity field including only the first and the second terms in formula (5) as the D-model.

Including the fourth term in formula (5) corresponds to the quadrupole approximation to the bulk motion, and its contribution can be interpreted as the measure of anisotropy of the expansion velocities. Such anisotropic expansion can be described by the direction-dependent “Hubble constant”

$$H(\mathbf{n}) = H + Q_{ij}n_i n_j. \quad (6)$$

If we drew a family of vectors of the length  $H(\mathbf{n})$  from the coordinate origin, their end points would lie on the surface of a three-axial ellipsoid whose axes coincide with the eigenvectors of tensor  $\mathbf{Q}$ . Expansion is fastest and slowest along the major and minor axis, respectively.

Hereafter, we refer to the bulk motion model described by the combination of the first, second, and fourth terms in formula (5) as the DQ-model.

The third term in formula (5), which is obtained by extracting the trace of tensor  $\mathbf{B}$ , acts effectively as a quadratic (in distance) addition to the dipole component, i.e., contributes to the variation of  $\mathbf{D}$  obtained in the dipole approximation for various sample depths.

In the linear approximation of the theory of perturbations (Peebles, 1980) the density of matter is proportional to the divergence of the velocity field. Assuming the potentiality of the velocity field, we see that in the approximation used [formula (1)], vector  $\mathbf{P}$  is proportional to the gradient of the matter density distribution.

Finally, the fifth term in formula (5) yields the octupole component of the bulk velocity. These two components are, like the dipole component, asymmetric and have opposite signs at opposite points of the sky. By contrast, the quadrupole component is symmetric.

Hereafter, we refer to the bulk motion model described by all five components in formula (5) as the DQO-model.

**Table 1.** The coefficients of the generalized Tully–Fisher relation, their errors, and statistical significance

$i$	D-model		DQ-model		DQO-model	
	$c_i$	$F_i$	$c_i$	$F_i$	$c_i$	$F_i$
$R_{\max} = 8000 \text{ km s}^{-1}$ (951 galaxies)						
1	$16.1 \pm 1.9$	70	$16.7 \pm 1.9$	75	$16.7 \pm 1.9$	74
2	$2.31 \pm 0.24$	90	$2.29 \pm 0.25$	86	$2.32 \pm 0.25$	86
3	$-0.796 \pm 0.152$	27	$-0.785 \pm 0.152$	27	$-0.777 \pm 0.153$	26
4	$8.24 \pm 1.64$	25	$7.79 \pm 1.65$	22	$7.70 \pm 1.65$	22
5	$(-4.79 \pm 1.80) \times 10^{-3}$	7.1	$(-5.45 \pm 1.80) \times 10^{-3}$	9.2	$(-4.99 \pm 1.92) \times 10^{-3}$	6.8
6	$-860 \pm 101$	72	$-871 \pm 101$	74	$-874 \pm 103$	72
$R_{\max} = 10000 \text{ km s}^{-1}$ (1134 galaxies)						
1	$18.2 \pm 1.6$	123	$18.8 \pm 1.7$	126	$18.8 \pm 1.7$	124
2	$2.03 \pm 0.22$	82	$1.99 \pm 0.23$	74	$2.02 \pm 0.23$	76
3	$-0.846 \pm 0.146$	34	$-0.851 \pm 0.146$	34	$-0.809 \pm 0.148$	30
4	$6.68 \pm 1.42$	25	$6.02 \pm 1.45$	17	$6.20 \pm 1.45$	18
5	$(-7.59 \pm 1.21) \times 10^{-3}$	39	$(-7.79 \pm 1.23) \times 10^{-3}$	40	$(-7.55 \pm 1.35) \times 10^{-3}$	31
6	$-815 \pm 98$	68	$-817 \pm 99$	68	$-873 \pm 100$	76

*Model Parameters*

*Associated with Multipole Components*

The first term in formula (5) characterizes the distances to individual objects of the sample. We determine this term using a generalized Tully–Fisher relation, which we describe below. This method does not allow the Hubble constant  $H$  to be determined, and, therefore, we use instead of distance  $r$  the coordinate  $R = Hr$ , i.e., the distance measured in  $\text{km s}^{-1}$  that is equal to the radial velocity of the galaxy in the absence of non-Hubble motions. Equation (5) then acquires the following form:

$$V_r = R + (D_i + R^2 P_i) n_i + R Q_{ij} n_i n_j + R^2 O_{ijk} n_i n_j n_k, \quad (7)$$

where tensors  $P_i$ ,  $Q_{ij}$ , and  $O_{ijk}$  are redenoted in an obvious way.

The dipole component is determined by three parameters  $D_i$  and the quadrupole component is determined by five parameters  $q_i$ :

$$V_r^{\text{quad}} = R \{ q_1 (n_1^2 - n_3^2) + q_2 (n_2^2 - n_3^2) + q_3 n_1 n_2 + q_4 n_1 n_3 + q_5 n_2 n_3 \}. \quad (8)$$

The octupole component is determined by seven parameters  $d'_i$ :

$$V_r^r = R^2 \{ d'_1 (3n_1 n_2^2 - n_1^3) + d'_2 (3n_1 n_3^2 - n_1^3) + d'_3 (3n_2 n_1^2 - n_2^3) + d'_4 (3n_2 n_3^2 - n_2^3) + d'_5 (3n_3 n_1^2 - n_3^3) + d'_6 (3n_3 n_2^2 - n_3^3) + d'_7 n_1 n_2 n_3 \}. \quad (9)$$

Together with three parameters of the vector part  $P_i$  of tensor  $\mathbf{B}$ , we have a ten-parameter, quadratic (in distance) component of the model. Hereafter, we refer to this component as the octupole component of the model. We hope that this will not lead to misunderstanding. We parametrize it as follows:

$$V_r^{\text{oct}+P} = R^2 \{ d_1 n_1^3 + d_2 n_2^3 + d_3 n_3^3 + d_4 n_1 n_2^2 + d_5 n_1 n_3^2 + d_6 n_2 n_1^2 + d_7 n_2 n_3^2 + d_8 n_3 n_1^2 + d_9 n_3 n_2^2 + d_{10} n_1 n_2 n_3 \}. \quad (10)$$

Parameters  $d_i$  in formula (10) can be expressed linearly in terms of  $d'_i$  and  $P_i$ .

Thus, if distances  $R$  are known, the most general DQO model is determined by eighteen parameters; the DQ model, by eight parameters, and the D-model, by three parameters of multipole expansions.

We use the 3K reference frame whose axes are associated with galactic coordinates  $l$  and  $b$ :

$$n_1 \equiv n_z = \sin b, \quad n_2 \equiv n_x = \cos l \cos b, \quad n_3 \equiv n_y = \sin l \cos b. \quad (11)$$

DETERMINATION OF DISTANCES TO GALAXIES

In our previous work (Karachentsev *et al.* 2000a), we analyzed the bulk motion of galaxies in the dipole approximation. We fitted the distance  $R$  to each galaxy using a set of regressors, which are some nonlinear combinations of galaxy parameters taken

**Table 2.** Statistical significance of the tensor components of the models according to Fisher’s test

Mo- del	Com- po- nent	Sample, $R_{\max}$ , km s <sup>-1</sup>									Quantiles, %	
		3000 <i>n</i> = 224	4000 <i>n</i> = 395	5000 <i>n</i> = 537	6000 <i>n</i> = 723	7000 <i>n</i> = 829	8000 <i>n</i> = 951	9000 <i>n</i> = 1064	10000 <i>n</i> = 1134	Entire <i>n</i> = 1271	99	99.9
D	D	5.54	4.25	3.60	3.12	5.37	9.83	9.33	8.16	5.96	3.78	5.42
DQ	D	4.58	3.60	4.07	3.95	4.89	7.96	7.36	6.62	6.12	3.78	5.42
	Q	3.35	2.59	3.05	2.38	1.86	4.36	2.82	2.53	1.78	3.02	4.10
	D + Q	4.28	3.24	3.28	2.67	3.19	6.48	5.29	4.66	3.36	2.51	3.27
DQO	D	3.41	2.91	2.66	2.81	1.85	0.49	1.12	2.31	4.59	3.78	5.42
	Q	2.65	2.80	3.38	2.14	1.38	2.58	2.07	2.58	2.49	3.02	4.10
	P	1.20	1.08	0.27	1.01	0.85	2.27	1.32	1.20	0.52	3.78	5.42
	O	1.41	1.70	4.60	2.00	4.34	2.62	2.11	2.49	5.64	2.64	3.47
	D + P	2.69	2.15	3.28	2.78	2.79	4.73	3.80	4.06	2.81	2.80	3.74
	O + P	1.30	1.57	3.43	1.65	3.32	2.36	2.04	2.23	4.84	2.32	2.96

**Table 3.** Parameters of the dipole component of the bulk velocity of galaxies in the galactic coordinate system

Model	$R_{\max}$	$D_z$	$D_x$	$D_y$	$D$	$l$ , deg	$b$ , deg	$\sigma$ , km s <sup>-1</sup>
	km s <sup>-1</sup>							
D	8000	17 ± 55	224 ± 68	-277 ± 69	356 ± 94	309	3	1065
DQ	8000	-32 ± 59	266 ± 73	-201 ± 73	335 ± 69	323	-5	1062
DQO	8000	-14 ± 90	116 ± 119	-65 ± 120	134 ± 111	331	-6	1054
D	10000	-7 ± 56	261 ± 68	-212 ± 71	336 ± 96	321	-1	1162
DQ	10000	-32 ± 61	263 ± 75	-173 ± 71	316 ± 71	327	-6	1159
DQO	10000	34 ± 87	121 ± 112	-248 ± 118	277 ± 105	296	7	1152

from the RFGC catalog. Our analysis of the statistical significance of possible regressors based on the Fisher tests led us to the following fit that generalizes the Tully–Fisher relation (in its “linear size–HI line width” form):

$$R = \frac{W}{a_r} (c_1 + c_2 B + c_3 B T) \quad (12)$$

$$+ c_4 \frac{W}{a_b} + c_5 \left( \frac{W}{a_r} \right)^2 + c_6 \frac{1}{a_r},$$

where  $W$  is the width of the HI line in km s<sup>-1</sup> measured at 50% level of its maximum value and corrected for cosmological expansion and turbulence;  $a_r$  and  $a_b$ , the angular major axes in arcmin as measured on red and blue copies of POSS and SERC plates, respectively, and corrected for the inclination to the line of sight and Milky-Way extinction;  $T$ , the centered index of morphological type of the galaxy equal to the type index  $I_t$  given in the catalog minus

the approximate mean index  $-T = I_t - 5.35$ ; and  $B$ , the centered index of surface brightness of the galaxy equal to the catalog surface brightness index  $I_{SB}$  minus the approximate mean value of this index  $-B = I_{SB} - 2$ .

We applied regression relation (12) to all RFGC galaxy samples considered and to all models. We obtained our subsamples by imposing upper limits on galaxy distances  $R < R_{\max}$  computed in terms of the dipole model. In our computations, we used the data for a total of 1271 galaxies.

Relation (12) differs somewhat from the one we used in our previous work (Karachentsev *et al.* 2000a). We excluded the term with the ratio of the major to minor axis, because its insignificance decreases substantially for the subsamples considered in this paper. We substituted the discarded term with the new regressor  $W/a_b$ , including the blue

diameter that proved to be statistically significant for all subsamples considered.

#### DETERMINATION OF THE PARAMETERS OF BULK MOTION AND OF THE GENERALIZED TULLY–FISHER RELATION

We estimate all model parameters using the least squares method and assuming that the deviations of galaxy velocities from the velocities computed in terms of the adopted model are exclusively due to chance fluctuations. Generally speaking, the latter assumption is not quite correct, because inhomogeneities of the matter density distribution inside and in the vicinity of the sample boundaries produce “small-scale” (compared to the 100 Mpc scale length) nonaccidental motions that are not considered in our models.

Note that substitution of model distances (12) into the DQ and QDO models of bulk motion makes them nonlinear in determined parameters. However, we do not linearize the models but determine their parameters via iterations in distances  $R$ .

The computed parameters and their errors for the subsamples with different  $R_{\max}$  are summarized in Tables 1–6, which also give the parameters  $F$  of statistical significance according to the Fisher test for the corresponding terms in the approximation of the velocity field.

## RESULTS

### *Generalized Tully–Fisher Relation*

Table 1 gives the parameters of the generalized Tully–Fisher relation (12) for all three models (D, DQ, and DQO) and two  $R_{\max} - R_{\min} = 8000$  and  $10000 \text{ km s}^{-1}$ . Parameters of regression (12) for all six versions considered agree well with each other. All deviations are within the  $1\sigma$  errors. The statistical significance according to the Fisher test exceeds 99.95% in all cases, except the fifth term in formula (12) for  $R_{\max} = 8000 \text{ km s}^{-1}$  whose statistical significance reduces down to 99.5%. The same trend can be seen for subsamples with lower  $R_{\max}$  for which we do not give the computational results. It is well known that the statistical significance levels of 95, 99, 99.5, 99.9, and 99.95% correspond to  $F = 3.8, 6.6, 7.9, 10.8,$  and  $12.1,$  respectively, for the case where the numerator has one degree of freedom and the denominator has an infinite number of degrees of freedom.

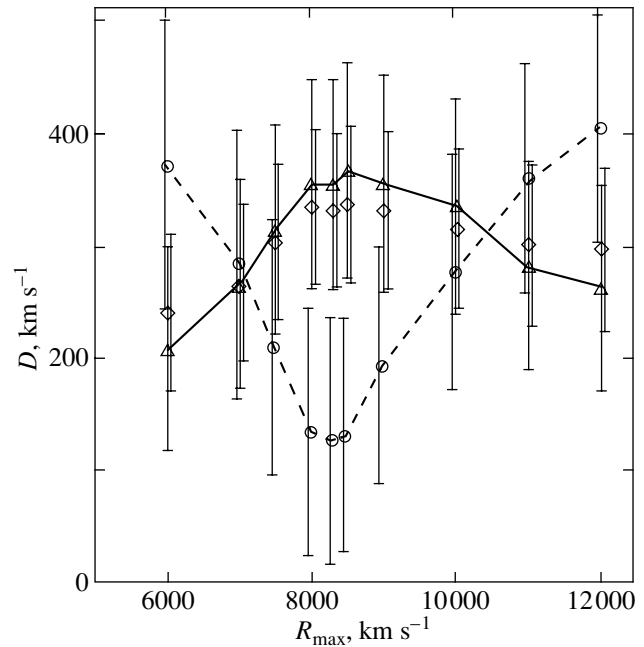


**Fig. 1.** The absolute value of the velocity of the dipole component as a function of the maximum distance to the galaxies of the subsample. Triangles, squares, and circles indicate the results of computations made in terms of D-model, DQ-model, and DQO-model, respectively. For convenience, the error bars of the latter two models are slightly shifted sideways.

### *Statistical Significance of Multipole Components*

The computed statistical significances of tensor multipole components using the Fisher test are listed in Table 2. For comparison, the last columns of the table give the quantiles of Fisher’s  $F$ -distribution for the case where the denominator has infinite number of degrees of freedom and the number of degrees of freedom of the numerator is equal to that of the model parameters tested for significance.

It also follows from Table 2 that:

- (1) The statistical significance of the dipole term in the D and DQ models exceeds 99.9%, at least for subsamples with  $R_{\max} > 7000 \text{ km s}^{-1}$ ;
- (2) The statistical significance of the quadrupole term in DQ model exceeds 95% for most of the subsamples;
- (3) The statistical significance of the quadrupole term in the DQO model changes substantially, with a minimum value close to 99%;
- (4) The statistical significance of the octupole term exceeds 95% for all samples and reaches values higher than 99.9% for some of the samples;
- (5) Octupole trace  $\mathbf{P}$  is statistically insignificant for all subsamples.

**Table 4.** Parameters of the quadrupole component of the bulk motion of galaxies in the galactic coordinate system

$i$	$R_{\max} = 8000 \text{ km s}^{-1}$				$R_{\max} = 10000 \text{ km s}^{-1}$			
	DQ-model		DQO-model		DQ-model		DQO-model	
	$q_i, \%$	$F_i$	$q_i, \%$	$F_i$	$q_i, \%$	$F_i$	$q_i, \%$	$F_i$
1	$5.5 \pm 1.8$	9.4	$4.0 \pm 2.2$	3.5	$4.3 \pm 1.6$	6.8	$5.7 \pm 2.1$	7.5
2	$1.8 \pm 1.9$	0.9	$3.3 \pm 2.3$	2.0	$0.8 \pm 1.7$	0.2	$1.0 \pm 2.1$	0.2
3	$-2.1 \pm 2.6$	0.7	$-1.5 \pm 2.9$	0.3	$2.9 \pm 2.2$	1.8	$2.6 \pm 2.6$	1.0
4	$-2.5 \pm 2.7$	0.9	$0.2 \pm 3.1$	0.0	$0.0 \pm 2.3$	0.0	$0.4 \pm 3.0$	0.2
5	$5.1 \pm 3.3$	2.4	$1.5 \pm 3.6$	0.2	$0.4 \pm 3.0$	0.0	$-1.0 \pm 3.5$	0.8

It thus follows that the dipole, quadrupole, and octupole components of the models are statistically significant, whereas the octupole trace  $\mathbf{P}$  can be dropped from the model.

#### *Dipole Component of Bulk Motion*

Table 3 gives the parameters of the dipole component of bulk velocity (velocity components and their errors, absolute velocity and its error, and the position of the apex) for all six cases, as well as the standard deviations  $\sigma$  of galaxy velocities from the corresponding approximation. All models yield similar apexes, which are close to that determined by Karachentsev *et al.* (2000a):  $l = 328^\circ \pm 15^\circ$  and  $b = 7^\circ \pm 15^\circ$ . The situation with the magnitude of velocity is quite different. To analyze it in more detail, let us study Fig. 1, which shows the magnitude of the velocity of the dipole component and its error for three models with different  $R_{\max}$ . It can be seen from this figure that the inclusion of the quadrupole term has virtually no effect on the magnitude of the dipole term for all  $R_{\max}$ . However, in the case of  $7000 \text{ km s}^{-1} < R_{\max} < 9000 \text{ km s}^{-1}$ , the inclusion of the octupole term significantly decreases the magnitude of the dipole component of velocity. The latter can be seen to have a minimum in the vicinity of  $R_{\max} = 8250 \text{ km s}^{-1}$ , and this minimum is almost three times lower than in the D- and DQ models. Note that the velocity given by the DQO model insignificantly exceeds its standard error and is, therefore, close to zero. It is evident from this that the reduction of the same data using the same technique in terms of models with and without the octupole component yields qualitatively different conclusions about the absolute value of the bulk velocity. This result is of interest for the estimates of the minimum scale length on which density inhomogeneities are smoothed out and the absolute bulk velocity converges.

The closeness of the dipole components of the D and DQ models and the strong sensitivity of these

components to the introduction of the octupole component are apparently due to the fact that the dipole and octupole terms are symmetric and the quadrupole is asymmetric with respect to spatial reflections. Identical symmetry properties result in strong dipole-octupole interaction (if the octupole component is dropped, the dipole component overtakes its role in describing the asymmetric properties of the velocity field), which can lead to overestimating the bulk velocity in the dipole approximation because of the inadequacy of the D-model.

#### *Quadrupole Component of Bulk Motion*

Table 4 lists the parameters  $q_i$  of the quadrupole component (8) of the velocity field, their errors and statistical significances according to the Fisher test. For better illustration, Table 5 gives the eigenvectors and eigenvalues of tensor  $\mathbf{Q}$ .

In the DQ-model with  $R_{\max} = 10000 \text{ km s}^{-1}$ , the maximum eigenvalue of  $4.8 \pm 1.5\%$  is associated with the eigenvector pointing toward  $l = 1^\circ$  and  $b = 70^\circ$  (Bootis, in the vicinity of Virgo) and its opposite (Cetus, in the vicinity of Pisces). The minimum eigenvalue of  $-5.1 \pm 1.7\%$  is associated with the direction  $l = 272^\circ$  and  $b = 0^\circ$  (Vela) and its opposite (Cygnus). The third axis is directed along  $l = 182^\circ, b = 20^\circ$  (Gemini) and its opposing constellation of Sagittarius is characterized by the statistically insignificant value of  $0.3 \pm 1.5\%$ . As follows from our analysis, the anisotropic ‘‘Hubble constant’’ varies from 94.9 to 104.8% of its mean value.

Table 5 gives the quadrupole eigenvectors and eigenvalues for  $R_{\max} = 10000, 9000, 8500, 8000, 6000, \text{ and } 3000 \text{ km s}^{-1}$ . It is evident from the data listed in the table that the amplitude of the quadrupole component increases with decreasing sample depth, because the tidal influence of external gravitating masses is more important for small volumes than for large ones. The directions corresponding to the

**Table 5.** Eigenvectors and eigenvalues of the tensor of quadrupole component

$R_{\max}$ , km s <sup>-1</sup>	Maximum			Minimum			Third axis		
	$Q_1$ , %	$l$ , deg	$b$ , deg	$Q_2$ , %	$l$ , deg	$b$ , deg	$Q_3$ , %	$l$ , deg	$b$ , deg
DQ-model									
3000 Staveley-Smith and Davies, 1989	24 ± 6	339	5	-17 ± 5	75	54	-7 ± 5	245	35
6000 Willick <i>et al.</i> , 1997	6.1	5	22	-9.7	166	66	3.6	272	8
3000 Willick and Strauss, 1998	15.9 ± 5.7	282	16	-21.1 ± 5.9	78	73	5.1 ± 7.0	191	7
6000	5.0 ± 1.9	168	45	-7.8 ± 2.3	69	10	2.9 ± 1.9	329	44
8000	6.1 ± 1.7	205	69	-8.1 ± 1.9	104	4	2.0 ± 1.9	13	20
8500	5.0 ± 1.5	294	84	-6.5 ± 1.9	107	6	1.5 ± 1.7	197	1
9000	4.7 ± 1.5	10	69	-6.2 ± 1.8	104	2	1.5 ± 1.6	195	21
10000	4.8 ± 1.5	1	70	-5.1 ± 1.7	92	0	0.3 ± 1.5	182	20
DQO-model									
3000	16.8 ± 6.1	304	15	-18.4 ± 6.4	88	72	1.5 ± 7.7	211	10
6000	5.4 ± 2.3	161	13	-7.7 ± 2.5	70	4	2.4 ± 2.4	324	76
8000	4.5 ± 1.9	183	58	-7.4 ± 2.1	274	1	2.9 ± 2.0	5	32
8500	3.9 ± 1.8	10	70	-6.6 ± 2.0	272	3	2.7 ± 2.1	182	20
9000	4.8 ± 2.1	50	85	-6.2 ± 2.1	274	4	1.4 ± 2.2	184	4
10000	6.1 ± 2.0	1	76	-6.7 ± 2.2	266	1	0.7 ± 2.0	176	14

**Table 6.** Parameters of the octupole component of the bulk velocity field of galaxies in the galactic coordinate system

$i$	$R_{\max} = 8000$ km s <sup>-1</sup>		$R_{\max} = 10000$ km s <sup>-1</sup>	
	$d_i \times 10^6$	$F_i$	$d_i \times 10^6$	$F_i$
1	3.2 ± 4.8	0.5	-7.5 ± 3.8	3.8
2	6.5 ± 6.7	1.0	7.7 ± 4.7	2.7
3	-2.8 ± 6.5	0.2	-2.0 ± 5.8	0.1
4	4.1 ± 8.2	0.2	13.3 ± 5.8	5.2
5	-14.4 ± 8.3	3.0	-2.8 ± 7.0	0.2
6	13.0 ± 8.8	2.2	7.7 ± 6.4	1.4
7	0.0 ± 11.2	0.0	-5.8 ± 9.3	0.4
8	0.0 ± 9.3	0.0	15.2 ± 7.0	4.7
9	-37.9 ± 10.9	12.2	-8.6 ± 8.2	1.1
10	20.1 ± 11.8	2.9	10.7 ± 8.6	1.6

maximum and minimum do not remain constant for different  $R_{\max}$ . As  $R_{\max}$  decreases, the shape of the ellipsoid  $H(l, b)$  approaches that of an oblate spheroid.

This effect manifests itself in the fact that the eigenvalues of the third axis are positive and the difference between these eigenvalues and the maximum eigen-

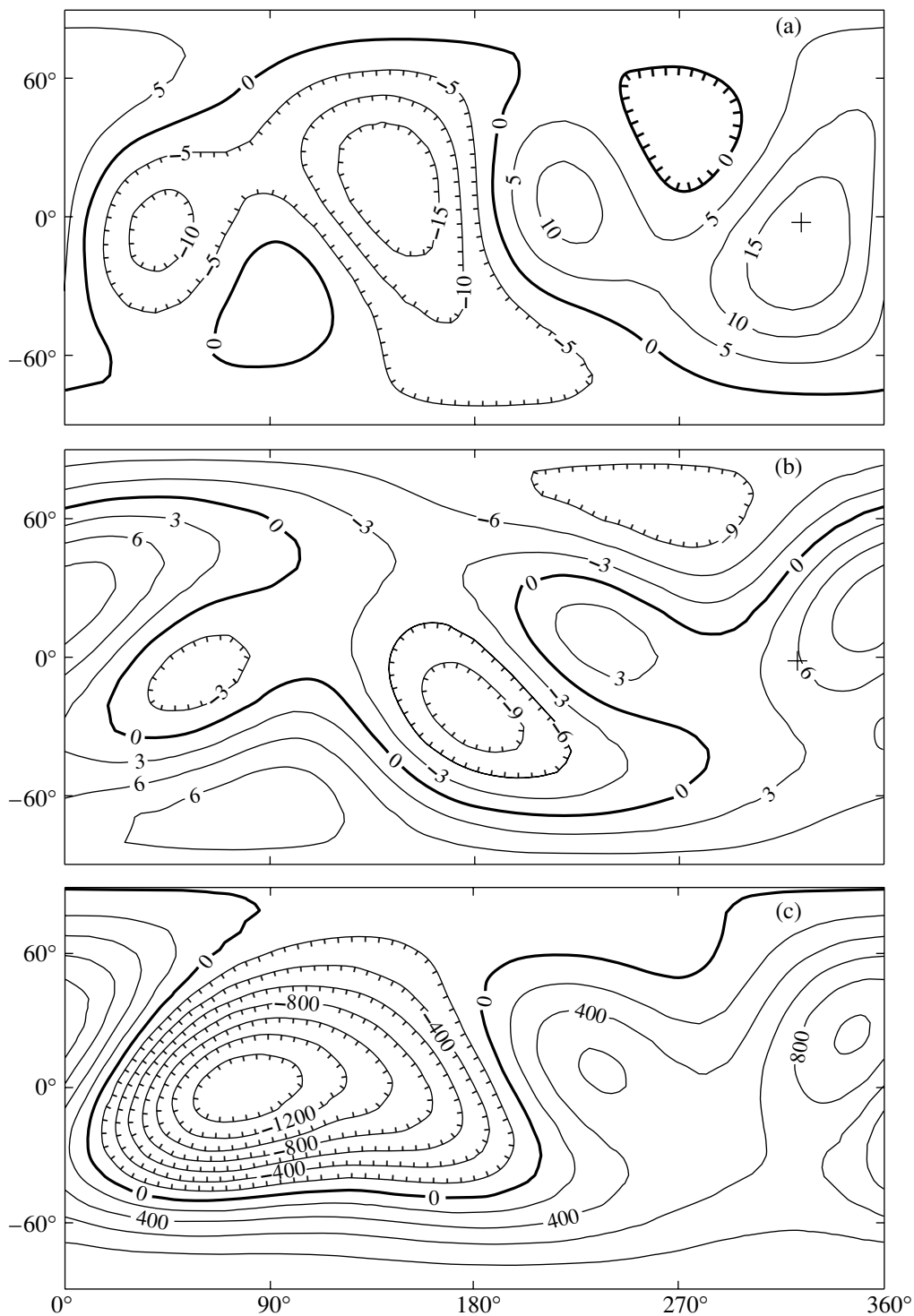


**Fig. 2.** Contours of the constant radial velocity of the octupole component of the bulk motion of galaxies for two subsamples with (a)  $R_{\max} = 8000 \text{ km s}^{-1}$  and (b)  $R_{\max} = 10000 \text{ km s}^{-1}$ . (c) Contours of the constant velocity for the entire bulk motion for  $R = 8000 \text{ km s}^{-1}$ . DQO-model with  $R_{\max} = 10000 \text{ km s}^{-1}$  is used.

value decreases in absolute value with decreasing  $R_{\max}$ .

Thus, all models yielded statistically significant quadrupole components of the velocity field. The

deviation from the Hubble law is equal to about 5% and 18% on the scale lengths 6000–10000  $\text{km s}^{-1}$  and that of the Local Supercluster (3000  $\text{km s}^{-1}$ ), respectively.

Staveley-Smith and Davies (1989) estimated the magnitude of the quadrupole effect for a sample with a characteristic depth of  $\sim 3000 \text{ km s}^{-1}$ . Willick and Strauss (1998) estimated the quadrupole component on a scale length of  $3000\text{--}6000 \text{ km s}^{-1}$  assuming that it is due to masses located beyond  $12800 \text{ km s}^{-1}$ . (These data are given in the first and second lines of Table 5). One can see that the magnitudes of the quadrupole effect determined by different authors agree satisfactorily with each other.

### *Octupole Component of Bulk Motion*

The parameters of the octupole component of the bulk velocity field are listed in Table 6 for two samples with  $R_{\text{max}} = 8000 \text{ km s}^{-1}$  and  $R_{\text{max}} = 10000 \text{ km s}^{-1}$ . To visualize the effect of the octupole component, we show in Fig. 2 the contours of function  $F(l, b) = 10^6(O_{ijk}n_i n_j n_k + P_i n_i)$ . According to equation (7), the latter quantity determines a contribution to the radial velocity of the galaxy that is quadratic in distance. It is evident from the figure that  $F(l, b)$  has two maxima at  $l > 210^\circ$  and two minima located symmetrically with respect to these maxima. The highest maximum lies at  $l = 320^\circ, b = -20^\circ$  and  $l = 355^\circ, b = 20^\circ$  for the subsamples with  $R_{\text{max}} = 8000 \text{ km s}^{-1}$  and  $R_{\text{max}} = 10000 \text{ km s}^{-1}$ , respectively. The second maxima associated with the directions  $l = 220^\circ, b = 0^\circ$  and  $l = 210^\circ, b = 10^\circ$  are even closer to each other. For the two subsamples in the southern circumpolar region, the third maximum is associated with directions  $l = 90^\circ, b = -40^\circ$  and  $l = 80^\circ, b = -70^\circ$ , respectively. For the subsample with  $R_{\text{max}} = 10000 \text{ km s}^{-1}$  this maximum is second in magnitude. Although the overall patterns of the contours of  $F(l, b)$  are rather similar to each other, their maxima differ by a factor of two to three.

As is evident from Table 6, the components of the octupole term of the bulk velocity differ more importantly from one subsample to another than do those of the quadrupole and dipole terms. This also applies to the statistical significance of the octupole—the fact that seems to be due to the higher sensitivity of the octupole to “small-scale” motions associated with the inhomogeneities of the field of matter density near the subsample boundary. This effect is especially conspicuous for large distances, because local field inhomogeneities have weights proportional to  $R^2$ .

Crosses in Figs. 2a and 2b indicate the directions of the dipole component of velocity. It is evident from the figure that the octupole component for this direction is positive and close to its maximum value over the sky. As a result, the deviation of the bulk velocity from the Hubble velocity for galaxies seen

toward the apex of the dipole component increases with distance. After averaging over the sample, the D-model yields larger magnitude of the bulk velocity than the DQO-model, as is evident from Fig. 1. For subsamples with  $R_{\text{max}} > 11000 \text{ km s}^{-1}$  and  $R_{\text{max}} < 7000 \text{ km s}^{-1}$ , function  $F(l, b)$  in the direction of the apex of the dipole component becomes negative, and, as a result, the relation between the results of computations made in terms of the two models reverses.

Since vector  $\mathbf{P}$  is proportional to the gradient of matter density, its statistical insignificance indicates that the data and velocity field models used in this paper allow no definitive conclusions to be made about large-scale density fluctuations.

### *Overall Pattern of Velocity Field*

We obtain the velocity field pattern in vectorial form (1), which allows us to compute not only the radial but also the tangential components of galaxy velocities. However, direct comparison with observational data is possible only for radial velocities (7). The field of radial velocities of the DQO model is rather complex. This fact is illustrated in Fig. 2c, which shows the contours of constant peculiar velocity computed by summing three radial components at  $R = 8000 \text{ km s}^{-1}$  for the DQO model with  $R_{\text{max}} = 10000 \text{ km s}^{-1}$ . Recall that to obtain the velocity of recession, one must add to the values shown in Fig. 2c the much greater Hubble velocity of  $R = 8000 \text{ km s}^{-1}$ . The velocity field pattern exhibits a conspicuous minimum at  $l = 80^\circ, b = 0^\circ$  (Cygnus) and a much more blurred maximum. The amplitude of the minimum is equal to about 18% of the Hubble velocity, whereas that of the maximum is smaller by a factor of 1.5.

At the distance corresponding to the Hubble velocity of about  $6000 \text{ km s}^{-1}$  the dipole, quadrupole, and octupole components are of comparable magnitude. This distance can be considered to be the scale length of velocity field irregularities in the models considered. At smaller distances, bulk velocities of galaxies are dominated by the dipole component.

## CONCLUSIONS

An analysis of the bulk velocities of galaxies from the RFGC catalog using new observational data (Karachentsev *et al.* 2000b) confirmed the apex direction of the dipole velocity component inferred in our earlier work. The transition to the DQ-model has virtually no effect on the magnitude of this velocity. Inclusion of the octupole component (DQO model) significantly decreases the magnitude of the velocity of the dipole component for subsamples with  $7000 \text{ km s}^{-1} < R_{\text{max}} < 10000 \text{ km s}^{-1}$ .

The quadrupole and octupole components of bulk velocity are statistically significant. The former results in a small (5–8%) anisotropy of galaxy expansion, which can be described by introducing a direction-dependent “Hubble constant” (5).

The amplitude of the quadrupole effect is equal to about 18% on the scale of the Local Supercluster and decreases to  $\sim 5\%$  on scales of  $R_{\max} = 6000\text{--}10000 \text{ km s}^{-1}$ , in accordance with the results of other authors.

The parameters of the octupole component depend significantly on the sample depth  $R_{\max}$ . This must be due to the intricate pattern of the distribution of matter in the volume considered. On the whole, the allowance for the octupole component reduces the amplitude of the dipole effect, which for the sample with  $R_{\max} = 8000 \text{ km s}^{-1}$  drops to  $134 \pm 111 \text{ km s}^{-1}$ . Thus, the analysis of the same data with and without allowance for the octupole can yield significantly different conclusions as to whether the amplitude of the dipole component of the bulk velocity of galaxies remains constant or decreases with increasing volume of the sample.

#### ACKNOWLEDGMENTS

This work was supported by the Russian Foundation for Basic Research (grant no. 97-02-16100).

#### REFERENCES

1. A. Dekel, *Annu. Rev. Astron. Astrophys.* **32**, 371 (1994).
2. A. Dekel, A. Eldar, T. Kolatt, *et al.*, *Astrophys. J.* **522**, 1 (1999).
3. Y. Hoffman, A. Eldar, S. Zaroubi, and A. Dekel, *astro-ph/0102190*.
4. I. D. Karachentsev, V. E. Karachentseva, and S. L. Parnovsky, *Astron. Nachr.* **314**, 97 (1993).
5. I. D. Karachentsev, V. E. Karachentseva, Yu. N. Kudrya, and S. L. Parnovsky, *Astron. Nachr.* **316**, 369 (1995).
6. I. D. Karachentsev, V. E. Karachentseva, Yu. N. Kudrya, *et al.*, *Bull. SAO* **47**, 5 (1999).
7. I. D. Karachentsev, V. E. Karachentseva, Yu. N. Kudrya, and S. L. Parnovskii, *Astron. Zh.* **77**, 175 (2000a) [*Astron. Rep.* **44**, 150 (2000a)].
8. I. D. Karachentsev, V. E. Karachentseva, Yu. N. Kudrya, *et al.*, *Bull. SAO* **50**, 5 (2000b).
9. A. Kogut, C. Lineweaver, G. F. Smoot, *et al.*, *Astrophys. J.* **419**, 1 (1993).
10. T. Lauer and M. Postman, *Astrophys. J.* **425**, 418 (1994).
11. P. B. Lilje, A. Yahil, and B. J. T. Jones, *Astrophys. J.* **307**, 91 (1986).
12. S. L. Parnovsky, I. D. Karachentsev, V. E. Karachentseva, and Yu. N. Kudrya, in *Abstract Book of IAU 24th General Assembly, Manchester, 2000*, p. 31.
13. P. J. E. Peebles, *The Large Scale Structure of the Universe* (Princeton Univ. Press, Princeton, 1980).
14. L. Staveley-Smith and R. D. Davies, *Mon. Not. R. Astron. Soc.* **241**, 787 (1989).
15. M. A. Strauss and J. A. Willick, *Phys. Rep.* **261**, 271 (1995).
16. J. A. Willick, *astro-ph/0003232*.
17. J. A. Willick and M. A. Strauss, *Astrophys. J.* **507**, 64 (1998).
18. J. A. Willick, M. A. Strauss, A. Dekel, and T. Kolatt, *Astrophys. J.* **486**, 629 (1997).

*Translated by A. Dambis*

# Ultrahigh Energy Cosmic Ray Acceleration in Seyfert Galactic Nuclei

A. V. Uryson\*

*Lebedev Physical Institute, Russian Academy of Sciences, Leninskii pr. 53, Moscow, 117924 Russia*

Received January 30, 2001; in final form May 20, 2001

**Abstract**—We propose a model for the particle acceleration to energy  $E \approx 10^{21}$  eV in Seyfert galactic nuclei. The model is based on the theory of active galactic nuclei by Vilkoviskij *et al.* (1999). The acceleration takes place in hot spots of relativistic jets, which decay in a dense stellar kernel at a distance of 1–3 pc from the center. The maximum energy and chemical composition of the accelerated particles depend on the jet magnetic-field strength. Fe nuclei acquire the largest energy,  $E \approx 8 \times 10^{20}$  eV, if the jet field strength is  $B \approx 16$  G. At a field strength  $B \sim 5$ –40 G, the nuclei with  $Z \geq 10$  acquire energy  $E \geq 2 \times 10^{20}$  eV; the lighter nuclei are accelerated to  $E \leq 10^{20}$  eV. In a field  $B \sim 1000$  G, only the particles with  $Z \geq 23$  gain energy  $E \geq 10^{20}$  eV. The protons are accelerated to  $E < 4 \times 10^{19}$  eV, and they do not fall within the energy range concerned at any field strength  $B$ . Interactions with infrared photons do not affect the accelerated-particle escape from the sources if the galactic luminosity  $L \leq 10^{46}$  erg s<sup>-1</sup> and if the angle between the normal to the galactic plane and the line of sight is sufficiently small, i.e., if the galactic-disk axial ratio is comparatively large. The particles do not lose their energy through magnetodrift radiation if their deflection from the jet axis does not exceed 0.03–0.04 pc at a distance  $R \approx 40$ –50 pc from the center. The synchrotron losses are small, because the magnetic field frozen in the galactic wind at  $R \leq 40$ –50 pc is directed (as in the jet) predominantly along the motion. If this model is correct, then the detected protons are nuclear fragments or are accelerated in other sources. The jet magnetic fields can be estimated by using the cosmic-ray energy spectrum and chemical composition. © 2001 MAIK “Nauka/Interperiodica”.

Key words: *cosmic rays, nonthermal radiation*

## INTRODUCTION

Cosmic rays (CRs) with energies ( $4 \times 10^{19}$ – $3 \times 10^{20}$ ) eV have been detected with various facilities (Hillas 1998). The existence of such particles raises the question as to where and how they are accelerated to such high energies. Cocoons of radio galaxies (Norman *et al.* 1995), topological-defect annihilation (Berezinsky and Vilenkin 1997), quasars (Farrar and Biermann 1998), gamma-ray bursts (Totani 1998), massive primordial particle decays (Kuzmin and Rubakov 1998), and interactions of H-dibaryons predicted by quantum chromodynamics with the Earth's atmosphere (Koshelev 1999) have been proposed as the possible particle sources. Previously (Uryson 2001; Uryson 1996, 1999a, 1999b), we directly identified the sources by assuming that CRs were deflected only slightly by intergalactic magnetic fields and that the possible sources were no more than 100 Mpc away (for the Hubble constant  $H = 75$  km s<sup>-1</sup> Mpc<sup>-1</sup>). As the possible sources, we considered radio galaxies from the catalogs by Spinrad *et al.* (1985) and Kuhr *et al.* (1981), X-ray pulsars (as the strongest ones) from the catalog

by Popov (2000), and BL Lac objects and Seyfert galaxies from the catalog by Veron (1998). For our analysis, we took the extensive air showers triggered by particles with errors in the arrival direction in equatorial coordinates ( $\Delta\alpha, \Delta\delta$ )  $\approx 3^\circ$  [the effect of the error on the identification of sources was analyzed previously (Uryson 1999b)]: 48 showers detected with the AGASA facility (Takeda *et al.* 1999), one Navera Park shower [Watson 1995; its error was calculated by Farrar and Biermann (1998)], and four Yakutsk showers [Afanas'ev *et al.* 1996; the errors were calculated previously (Uryson 1999b)]. For the showers that arrived from different Galactic latitudes, we calculated the probabilities that the possible sources fell within the triple-error region ( $3\Delta\alpha, 3\Delta\delta$ )  $\approx 9^\circ$  by chance. The showers were selected by latitudes to exclude from our analysis the low-latitude sky regions known as the zones of avoidance of galaxies. The probabilities were found to be low,  $P > 3\sigma$  ( $\sigma$  is the Gaussian distribution parameter), for the showers with  $|b| > 31^\circ$  and Seyfert galaxies with moderate luminosities and radio and X-ray fluxes, as well as for BL Lac objects:  $P \approx 1.47 \times 10^{-3}$  ( $\approx 3.15\sigma$ ) and  $P \approx 1.77 \times 10^{-3}$  ( $\approx 3.10\sigma$ ), respectively. The number of showers with  $|b| > 31^\circ$  was

\*E-mail: uryson@sci.lebedev.ru

26. Previously (Uryson 1999a, 1999b), we searched for the sources using the catalog by Veron (1993) and estimated the probability for BL Lac objects to be  $P < 3\sigma$ . In our recent paper (Uryson 2001), we used the catalog by Veron (1998), in which the statistics of BL Lac objects at  $\delta > -10^\circ$  tripled, 159 compared to 55. This is the reason why the probability estimates for BL Lac objects differ.

Kardashev (1995) found that particles could be greatly accelerated in active galactic nuclei (AGNs); in the vacuum approximation, charged particles near a supermassive black hole are accelerated by an electric field to energy  $E \sim Z \times 10^{27}$  eV. The accelerated particles lose their energy through magnetodrift radiation. As a result, their energy decreases to  $10^{21}$  eV, a value that is high enough to explain the maximum energy  $3 \times 10^{20}$  eV observed in CRs (Bird *et al.* 1995). Particles are injected along the black-hole spin axis. If the black hole has such a magnetosphere that the magnetic field lines do not curve near the poles, then particles with energy  $\sim Z \times 10^{27}$  eV can be present in CRs. Norman *et al.* (1995) considered the conditions under which the energy losses of particles in AGNs near a black hole are so large that the injection of CRs with  $E \approx 10^{20}$  eV is definitely ruled out.

In the model by Kardashev (1995), particles are accelerated in AGNs with extended jets. Among the AGNs (possible CR sources), BL Lac objects have such jets. Jets are generally unseen in moderate-luminosity Seyfert galaxies. Here, we consider the mechanism of CR acceleration to energy  $E \geq 10^{20}$  eV in Seyfert galactic nuclei and show that the accelerated particles can leave the sources without substantial energy losses.

### CR ACCELERATION IN SEYFERT NUCLEI

We use the AGN theory by Vilkoviskij and Karpova (1996) and Vilkoviskij *et al.* (1999) to analyze the CR acceleration in moderate Seyfert nuclei. According to this theory, relativistic jets are formed near a massive black hole in most Seyfert galaxies, but they decay (are significantly, by 90% , absorbed) at a distance of 1–3 pc inside a massive stellar kernel. The jet parameters are: the cross section in the kernel  $S = 3 \times 10^{31}$  cm<sup>2</sup> and the relativistic factor  $\gamma = 10$ . In our model, particles are accelerated at the shock front in a hot spot of the jet. The jet field is parallel to the axis, and the particles are accelerated through scattering by turbulence-produced magnetic-field inhomogeneities to energy

$$E_j \approx Ze\beta_j BR_j \text{ erg}, \quad (1)$$

where  $Ze$  is the particle charge,  $\beta_j$  is the ratio of the jet velocity to the speed of light,  $B$  is the magnetic field

in the hot spot, and  $R_j$  is the spot diameter (Norman *et al.* 1995). For the above jet parameters, the jet velocity and diameter are  $\beta_j \approx 0.99$  and  $R_j \approx 6 \times 10^{15}$  cm, respectively; the maximum particle energy is

$$E_j \approx 1.9 \times 10^{18} ZB \text{ eV}. \quad (2)$$

In the hot-spot magnetic field, a particle loses its energy through synchrotron radiation simultaneously with its acceleration. From the condition of equality between the rates of energy gain and loss, we find that the energy does not exceed (Norman *et al.* 1995)

$$E_s \approx (Mc^2 Ze\beta_j Bct_s)^{1/2} \text{ erg}, \quad (3)$$

where  $M$  is the particle mass;  $t_s$  is (Ginzburg 1987)

$$t_s = (1.58 \times 10^{-15})^{-1} B^{-2} (A/Z)^3 \times Z^{-1} (m_p/m_e)^2 (m_p c^2)^{-1}, \quad (4)$$

where  $m_e$  and  $m_p$  are the electron and proton masses, respectively. For nuclei,  $A/Z \approx 2$ , and their maximum energy is

$$E_{sA} \approx 6.6 \times 10^{20} (Z/B)^{1/2} \text{ eV}. \quad (5)$$

The maximum proton energy is

$$E_{sp} \approx 1.65 \times 10^{20} B^{-1/2} \text{ eV}. \quad (6)$$

In a random magnetic field (Ginzburg 1987), the energy of both protons and nuclei increases by a factor of 1.2.

From the condition  $E_j = E_s$ , we find the field  $B_{CR}$  in which the particles with different numbers  $Z$  gain the maximum energy

$$B_{CR} = (3.5 \times 10^2)^{2/3} Z^{-1/3}. \quad (7)$$

In a field  $B < B_{CR}$ , the maximum particle energy is  $E = E_j$ ; in a field  $B > B_{CR}$ , the energy is  $E = E_{sA}$ .

For protons,  $B_p \approx 19.6$  G and  $E_{\max p} \approx 3.7 \times 10^{19}$  eV; for He nuclei ( $Z = 2$ ),  $B_{\text{He}} \approx 39.5$  G and  $E_{\max \text{He}} \approx 1.5 \times 10^{20}$  eV; and for Fe nuclei,  $B_{\text{Fe}} \approx 16$  G and  $E_{\max \text{Fe}} \approx 8 \times 10^{20}$  eV. The strength of the field frozen in the jet in the model by Vilkoviskij and Karpova (1996) and Vilkoviskij *et al.* (1999) is presently unknown. If the field is within the range  $B \sim 5\text{--}40$  G, then the nuclei with  $Z \geq 10$  gain energy  $E \geq 2 \times 10^{20}$  eV and the lighter nuclei are accelerated to  $E \leq 10^{20}$  eV. In a field  $B \sim 100$  G, the particles with  $cZ > 2$  are accelerated to  $E \geq 10^{20}$  eV. In a field  $B \sim 1000$  G, only the particles with  $Z \geq 23$  gain such energy. Protons are accelerated to  $E < 4 \times 10^{19}$  eV, and they do not fall within the energy range concerned at any  $B$ . Consequently, if this model is correct, then, first, the protons with energy  $E > 4 \times 10^{19}$  eV detected in CRs were not accelerated in Seyfert nuclei and are nuclear fragments or they were accelerated in other sources (probably in BL Lac objects), and, second, the jet magnetic fields can be estimated by using the CR energy spectrum and chemical composition.

## PARTICLE ESCAPE FROM THE SOURCES

The accelerated particles that left the hot spot do not interact with the bow shock generated by the jet in a flow of hot gas, since the wave propagates more slowly than the jet because the gas density is lower than the jet density (Chakrabarti 1988). The particles lose their energy in photopion reactions with infrared photons and through synchrotron and magnetodrift radiation.

The 10–100-pc region is surrounded by a geometrically and optically thick dusty torus that emits infrared photons (Pier and Krolik 1993). Inside the torus, the infrared radiation is absorbed and rescattered by clouds. The photopion losses in this radiation are small if the source luminosity  $L < 10^{46}$  erg s<sup>-1</sup> (Normal *et al.* 1995). The CR sources are identified precisely with such Seyfert galaxies. An accelerated particle does not enter the torus if it flies at such an angle  $i$  to the normal to the galactic plane that  $\tan i < l/h$ , where  $l$  is the inner radius of the torus, and  $h$  is its thickness; i.e., the galactic plane is viewed at a comparatively small angle. The angle  $i$  is characterized by the galactic axial ratio  $e_1/e_2$  (Simcoe *et al.* 1997):  $\cos i = e_2/e_1$ , since  $i = 55^\circ$  at  $e_2/e_1 = 0.6$ , the source galaxies must have a comparatively large  $e_2/e_1$  ratio.

The synchrotron losses in the gas flow are negligible, because its field is directed (as in the jet) predominantly along the motion. The magnetodrift losses of a particle with charge  $Z$  are (Zheleznyakov 1997)

$$-dE/dt = 2/3(Ze)^2 c(E/Mc^2)^4 (\rho_c)^{-2}, \quad (8)$$

where  $\rho_c$  is the radius of curvature of a field line. Hence, the particle energy decreases by half in time

$$T_{\text{curv}} = 7/2(Mc^2)^8 E^{-3} (Ze)^{-2} \rho_c^2 c^{-1}. \quad (9)$$

The particle travels along a field line to a distance  $R_{\text{line}}$ . The particles with energy  $E_{\text{max}}$  traverse this distance in time

$$t \approx R_{\text{line}}/c \approx 4.6 \times 10^9 \text{ s}. \quad (10)$$

The magnetodrift losses are small if the particle will lose no more than half of its energy  $E_{\text{max}}$  while moving along field lines:

$$T_{\text{curv}} > t. \quad (11)$$

The distance  $R_{\text{line}}$  can be determined as follows. An accelerated particle freely leaves the galaxy, reaching a region where the field decreases to such an extent that the particle gyroradius is  $r_L \geq 5$  kpc (Pochepinkin *et al.* 1995) (here, the characteristic sizes of spiral galaxies, to which most Seyferts belong, are assumed to be the same as those of our Galaxy). For ultrarelativistic particles, the gyroradius is  $r_L \approx E/(300ZB)$  (the energy  $E$  is in eV, the field  $B$  is in G, and  $r_L$  is in cm) (Berezinsky *et al.* 1990); for particles

with different  $Z$  and energies  $E = E_{\text{max}}$ , the condition  $r_L \geq 5$  kpc is satisfied in a field  $B \leq 10^{-5}$  G. Assuming that the magnetic field decreases with distance as  $B \sim R^{-3}$  (Vilkoviskij 2000) and that the field is  $B \sim 1$  G at a distance  $R \sim 1$  pc (Rees 1983), we obtain  $R_{\text{line}} \approx 46$  pc. In a dipole magnetic field, the radius of curvature of field lines is  $\rho_c = 4R^2/3a$ , where  $R$  and  $a$  are the distances from the dipole center and axis, respectively (Kardashev 1995). Hence, using (9)–(11), we estimate the maximum deflection from the jet axis of the particles with  $E = E_{\text{max}}$  that traversed a distance  $R \approx 46$  pc with small magnetodrift losses:  $a_p \approx 0.01$  pc for protons,  $a_{\text{He}} \approx 0.03$  pc for He nuclei, and  $a_{\text{Fe}} \approx 0.04$  pc for Fe nuclei.

Let us determine what fraction of the accelerated particles leave the source without magnetodrift losses. The angle of deflection from the jet axis for such particles is

$$\theta \leq a/R_{\text{line}} = 6.5 \times 10^{-4}. \quad (12)$$

Since the particles are scattered isotropically in the wave frame, we calculated the fraction concerned as follows. The angle  $\theta^*$  between the velocity vector and the jet axis in the wave frame is related to the angle  $\theta$  by (Landau and Lifshitz 1990)

$$\begin{aligned} \tan \theta &= (1 - \beta^2)^{1/2} (\beta + \cos \theta^*)^{-1} \sin \theta^* \\ &= 0.14 \sin \theta^* (0.99 + \cos \theta^*) \end{aligned} \quad (13)$$

at  $\beta \approx 0.99$ . For  $\theta < 0.02$ ,  $\sin \theta^* \approx \theta^*$ ,  $\cos \theta^* \approx 1$ , and  $\theta \approx 0.07\theta^*$ . Consequently,  $\theta^* \approx 0.01$ , and the fraction of the particles deflected from the jet axis through angles (12) is  $\eta \approx 0.01/\pi \approx 3 \times 10^{-3}$ ; i.e., approximately one of the 300 accelerated particles leaves the source without magnetodrift losses.

Hence, using the CR flux measured near the Earth, we can estimate the observed ultrahigh-energy cosmic-ray luminosity of the host galaxy  $L_{\text{UHECR}}$ :

$$L_{\text{UHECR}} = \int_E^\infty F_g(E) E dE, \quad (14)$$

where  $F_g(E) = KE^{-\gamma}$  is the differential particle generation spectrum in a Seyfert galaxy. If the high-energy CR spectrum is distorted only slightly by interactions in intergalactic space (this is possible on condition that the sources lie within  $\sim 50$  Mpc), then the spectrum of particle generation in the source  $F_g(E)$  and the observed CR spectrum  $I(E)$  at  $E > 5 \times 10^{19}$  eV have the same shape and  $F_g(E) = KE^{-\gamma}$ ,  $\gamma \geq 3.1$ . The intensity of CRs with energy  $E$  in the Universe is (Berezinsky *et al.* 1990)

$$I(E) = (c/4\pi) F_g(E) n_{\text{Sy}} T_{\text{Mg}}, \quad (15)$$

where  $n_{\text{Sy}} = 2 \times 10^{-77}$  cm<sup>-3</sup> is the density of Seyfert galaxies, and  $T_{\text{Mg}} = 1.3 \times 10^{10}$  years is the age of

the Universe.  $I(E)$  at  $E > 5 \times 10^{19}$  eV measured with various facilities (Watson 1996) is  $\approx 10^{-39} - 10^{-40}$  (cm<sup>2</sup> s sr eV)<sup>-1</sup>. From (14) and (15), we obtain the observed luminosity in CRs with  $E > 5 \times 10^{19}$  eV of the host galaxy  $L_{\text{UHECR}} \approx 10^{39} - 10^{40}$  erg s<sup>-1</sup> ( $\gamma \approx 3.1$ ). The actual luminosity is higher than the observed one by a factor of  $1/\eta$  and is  $L_{\text{UHECR, eff}} \approx 3 \times 10^{41} - 3 \times 10^{42}$  erg s<sup>-1</sup>.

### PARTICLE PROPAGATION IN MAGNETIC FIELDS

Identifying the possible sources, we assumed that the particles were deflected in intergalactic magnetic fields through an angle  $\alpha_0 \leq 9^\circ$ . In the simplest case where a particle with energy  $E$  moves in a plane perpendicular to the field and where the field inhomogeneities may be ignored, our estimate of the field outside clusters (Uryson 1999a) is  $B \leq (2\alpha_0 E)/(300Zr)$ , where  $r$  is the distance between the source and the facility, the energy  $E$  is in eV, the field  $B$  is in G, and  $r$  is in cm. Because of the energy losses in interactions with background radiation, the distance  $r$  traversed by a particle is limited (Greisen 1966; Zatsepin and Kuzmin 1966; Stecker 1998): protons interact with cosmic microwave background radiation, and if  $E < 10^{20}$ , then  $r \approx 40 - 50$  Mpc; at  $E \approx 2 \times 10^{20}$  and  $3 \times 10^{20}$  eV, the distance  $r$  is 30 and 15 Mpc, respectively. Nuclei lose their energy in photodisintegrations in the infrared background and can arrive from large distances: for Fe nuclei with  $E \approx 2 \times 10^{20}$  eV,  $r \approx 100$  Mpc. Using  $r$  for protons, we obtain a field estimate  $B < 2.3 \times 10^{-9}$  G; from  $r$  for Fe nuclei, we derive  $B \leq 2.7 \times 10^{-11}$  G. The inferred constraints on  $B$  agree with theoretical estimates (Kronberg 1994):  $B < 10^{-9}$  G as determined from measurements of the rotation measure for quasars at  $Z = 2.5$ ;  $B \ll 10^{-9}$  G if the ultrahigh-energy protons propagate in interplanetary space rectilinearly; the regular magnetic field, if it exists, has a strength  $B < 10^{-11}$  G.

The field can be much stronger inside galactic clusters: according to Kronberg (1993),  $B \sim 10^{-6} - 10^{-7}$  G at distances up to  $\sim 0.5$  Mpc from the cluster center. Consider the case where the CR source belongs to a cluster. According to Zasov (1999), the sizes of galactic clusters range from  $D \approx 1$  to  $D \approx 5 - 7$  Mpc. If the distance to the cluster is 40 Mpc, then its angular size is  $\alpha_{\text{cl}} \approx 1.4^\circ$  for  $D \approx 1$  Mpc and  $\alpha_{\text{cl}} \approx 10^\circ$  for  $D \approx 7$  Mpc (at larger  $r$ , the cluster angular sizes are smaller). In both cases, the cluster with the source entirely falls within the region of search, because the latter is larger in angular size than the cluster,  $2\alpha_0 \approx 18^\circ > \alpha_{\text{cl}}$ . The particle propagation in

intergalactic space in random fields  $B \sim 10^{-7}$  G was considered by Tanko (1997).

In the Galaxy, the particles move in fields  $B \sim 10^{-6}$  G. In the disk, the magnetic field is regular in the spiral arms and directed along them; and in the halo, the regular field component is perpendicular to the disk; the nonregular field component fluctuates with the main scale  $\delta L \sim 100$  pc,  $\delta B \sim 10^{-6}$  G (Kronberg 1994). Various models are used to describe the large-scale galactic-field structure (Cronin 1996; Stanev 1997). The deflection of a charged particle in a galactic field with a regular component depends on the initial particle direction and can be negligible. In a random magnetic field, the particle deflection does not depend on the initial direction. We estimate the rms angle of particle deflection on path  $d$  in a random field from the relation (Cronin 1996)

$$\psi \approx 1.7^\circ \left( \frac{d}{30 \text{ Mpc}} \right)^{1/2} \left( \frac{\delta L}{1 \text{ Mpc}} \right)^{1/2} \quad (16)$$

$$\times \frac{\delta B}{10^{-9} \text{ G}} \left( \frac{E}{10^{20} \text{ eV}} \right)^{-1} Z \approx 0.014^\circ \left( \frac{E}{10^{20} \text{ eV}} \right)^{-1} Z$$

for a path in the halo of  $d \approx 2$  kpc (the main scale of the halo magnetic field). It follows from (16) that the particles with energy  $E \approx 10^{21}$  eV and charges  $Z \leq 26$  are deflected through angles  $\psi < 0.4^\circ$ , while the particles with  $E \approx 10^{20}$  eV and  $Z \leq 10$  are deflected through  $\psi < 1^\circ$ . These deflections may be disregarded.

Thus, our identifications of the CR sources are valid if, first, the intergalactic magnetic fields outside clusters do not exceed  $B < 10^{-9}$  G; second, the particles arrived from directions where the deflections in a regular galactic magnetic field are small; and, third, the particles with energy  $E \leq 10^{20}$  eV have charges  $Z < 10$ . However, even for large particle deflections in the galactic magnetic field, the identification of possible CR sources is not meaningless: if the sources are actually astrophysical objects, then the particles with  $E > 10^{20}$  eV arrive from them with small deflections, while the particles with  $E > 4 \times 10^{19}$  eV form a halo around their arrival directions. For large shower statistics, Stanev (1997) suggests investigating the large-scale structure of the galactic magnetic field by analyzing the shower arrival directions and the angles between them.

### COSMIC RAYS WITH ENERGY $E > 10^{20}$ eV

In our acceleration model, the maximum energy is proportional to particle charge  $Ze$ , and the CRs with energy  $E \geq 10^{20}$  eV are nuclei. The sources of the nuclei can be up to  $\sim 100$  Mpc away (Stecker 1998). To test the model, we considered eleven showers

with  $E \geq 10^{20}$  eV, seven showers detected with the AGASA facility (Takeda *et al.* 1999), two Navera Park showers [Watson 1995; the errors in the arrival directions were calculated by Farrar and Biermann (1998)], one Yakutsk shower (Afanas'ev *et al.* 1996), and one shower detected with the Fly's Eye facility (Bird *et al.* 1995). The chemical composition of the CRs with energy  $E \geq 10^{20}$  eV is presently unknown. Since the probability estimates for these showers are unsuitable because of the poor statistics and large errors in the arrival directions of some particles, we checked whether moderate Seyfert galaxies up to 100 Mpc away fell within the triple-error region around the arrival directions of these particles. No such galaxy was found in the region of search of two showers, the Yakutsk shower and one of the AGASA showers. However, these showers fell within a zone of avoidance of galaxies, because they arrived from Galactic latitudes  $b = 3 \pm 2^\circ$  and  $-4.8^\circ$ , respectively. For the nine remaining showers, there are Seyfert galaxies in their regions of search: galaxies at redshifts  $z \leq 0.0092$  for seven showers and galaxies at  $z = 0.016$  and  $z = 0.018$ , i.e., up to 72 Mpc away, for two showers. This is consistent with the assumption that the showers could be triggered by nuclei. For seven of these nine showers, BL Lac objects also fell within their field of search; the redshifts of most of them are  $z > 0.1$  or unknown. However, this is consistent with the pattern of CR propagation for the following reasons. If the CRs in BL Lac objects are accelerated to energies  $E \sim 10^{27} Z$  eV (Kardashev 1995), then the particles can arrive as nuclear fragments with  $E \geq 10^{20}$  eV probably from considerably larger distances than 100 Mpc. The redshifts can be unknown because of the absence of obscuring material on the line of sight, which is more likely for objects within  $\sim 100$  Mpc than for distant galaxies. Therefore, BL Lac objects with unknown  $z$  are most likely  $\sim 100$  Mpc away (Kardashev 2000).

## CONCLUSIONS

Our model of CR acceleration to energies  $10^{21}$  eV in hot spots of Seyfert galaxies is based on the AGN theory by Vilkoviskij and Karpova (1996) and Vilkoviskij *et al.* (1999). The magnetic-field strength in the jet is an unknown model parameter. We assumed that the field could take on values in a wide range,  $B \sim 5\text{--}1000$  G. The maximum energy in the model depends on the field strength and is proportional to the particle charge  $Ze$ . The Fe nuclei gain the largest energy,  $E \approx 8 \times 10^{20}$  eV, if the field strength in the jet is  $B \approx 16$  G. For a field  $B \sim 5\text{--}40$  G, the nuclei with  $Z \geq 10$  gain energy  $E \geq 2 \times 10^{20}$  eV; the lighter nuclei are accelerated to  $E \leq 10^{20}$  eV. In a field  $B \sim 1000$  G, only the particles with  $Z \geq 23$  gain

energy  $E \geq 10^{20}$  eV. The protons are accelerated to  $E < 4 \times 10^{19}$  eV and do not fall within the energy range concerned at any  $B$ .

The accelerated particles leave the host galaxy without energy losses under the following conditions. First, they do not lose their energy in photopion reactions if the galactic luminosity is  $L < 10^{46}$  erg s $^{-1}$  (Norman *et al.* 1995). In our previous papers, we identified the CR sources with such galaxies. In addition, the angle between the normal to the galactic plane and the line of sight is small for the host galaxies; i.e., the galactic-disk axial ratio is comparatively large. Second, the particles do not lose their energy through magnetodrift radiation if their deflection from the jet axis does not exceed  $a \leq 0.03\text{--}0.04$  pc at  $R \sim 40\text{--}50$  pc. The synchrotron losses are small if the magnetic field frozen in the galactic wind at  $R \leq 40\text{--}50$  pc is directed (as in the jet) predominantly along the motion.

If this model is correct, then the detected protons with energy  $E > 4 \times 10^{19}$  eV are nuclear fragments or were accelerated in other sources (possibly, in BL Lac objects). In addition, the jet magnetic fields can be estimated by using the CR energy spectrum and chemical composition.

The CR spectra and composition will be measured with the AGASA facility, with the future giant Pierre Auger (Cronin 1992) and EAS-1000 (Fomin *et al.* 1999) facilities, and on satellites (Ormes *et al.* 1997).

## ACKNOWLEDGMENTS

I wish to thank N.S. Kardashev and Yu.N. Vetukhnovskaya for a discussion of the processes in AGNs and E.Ya. Vilkoviskij for a discussion of the jet parameters and formation conditions. I am also grateful to the referee for constructive remarks.

## REFERENCES

1. B. N. Afanasiev, M. N. Dyakonov, V. P. Egorova, *et al.*, in *Proceedings of the International Symposium on Extremely High Energy Cosmic Rays: Astrophysics and Future Observatories*, Ed. by M. Nagano (Inst. of Cosmic-Ray Research, Tokyo, 1996), p. 32.
2. V. Berezhinsky and A. Vilenkin, *Phys. Rev. Lett.* **79**, 5202 (1997).
3. V. S. Berezhinskiĭ, S. V. Bulanov, V. L. Ginzburg, V. A. Dogiel, and V. S. Ptuskin, *Cosmic-Ray Astrophysics*, Ed. by V. L. Ginzburg (Nauka, Moscow, 1990).
4. D. Bird, S. C. Corbato, H. Y. Dai, *et al.*, *Astrophys. J.* **441**, 144 (1995).
5. S. K. Chakrabarti, *Mon. Not. R. Astron. Soc.* **235**, 33 (1988).

6. J. W. Cronin, Nucl. Phys. B (Proc. Suppl.) **28**, 213 (1992).
7. J. W. Cronin, in *Proceedings of the International Symposium on Extremely High Energy Cosmic Rays: Astrophysics and Future Observatories*, Ed. by M. Nagano (Inst. of Cosmic-Ray Research, Tokyo, 1996), p. 2.
8. G. R. Farrar and P. L. Biermann, Phys. Rev. Lett. **81**, 3579 (1998).
9. Y. A. Fomin, N. N. Kalmykov, G. B. Christiansen, *et al.*, in *Proceedings of the 26th International Cosmic Ray Conference, ICRC, Salt Lake City, 1999*, Vol. 1, p. 526 (1999).
10. V. L. Ginzburg, *Theoretical Physics and Astrophysics* (Nauka, Moscow, 1987; Pergamon, Oxford, 1979).
11. K. Greisen, Phys. Rev. Lett. **16**, 748 (1966).
12. M. Hillas, Nature **395**, 15 (1998).
13. N. S. Kardashev, Mon. Not. R. Astron. Soc. **276**, 515 (1995).
14. N. S. Kardashev, private communication (2000).
15. N. I. Koshelev, Pis'ma Zh. Éksp. Teor. Fiz. **70**, 483 (1999) [JETP Lett. **70**, 491 (1999)].
16. P. P. Kronberg, Rep. Prog. Phys. **57**, 325 (1994).
17. H. Kuhr, A. Witzel, and I. I. K. Pauliny-Toth, Astron. Astrophys., Suppl. Ser. **45**, 367 (1981).
18. V. A. Kuz'min and V. A. Rubakov, Yad. Fiz. **61**, 1122 (1998) [Phys. At. Nucl. **61**, 1028 (1998)].
19. L. D. Landau and E. M. Lifshitz, *The Classical Theory of Fields* (Nauka, Moscow, 1990; Pergamon, Oxford, 1975).
20. C. A. Norman, D. B. Melrose, and A. Achterberg, Astrophys. J. **454**, 60 (1995).
21. J. F. Ormes, L. M. Barbier, K. Bogue, *et al.*, in *Proceedings of the 25th International Cosmic Ray Conference, ICRC, Durban, 1997*, Vol. 5, p. 273 (1997).
22. E. A. Pier and J. H. Krolik, Astrophys. J. **418**, 673 (1993).
23. D. N. Pochevkin, V. S. Ptuskin, S. I. Rogovaya, *et al.*, in *Proceedings of the 24th International Cosmic Ray Conference, ICRC, Rome, 1995*, Vol. 3, p. 136 (1995).
24. S. B. Popov, <http://xray.sai.msu.ru/~polar/> (2000).
25. M. J. Rees, Mon. Not. R. Astron. Soc. **228**, 47 (1987).
26. R. Simcoe, K. K. McLeod, J. Schachter, *et al.*, Astrophys. J. **489**, 615 (1997).
27. H. Spinrad, S. Djorgovski, J. Marr, *et al.*, Publ. Astron. Soc. Pac. **97**, 932 (1985).
28. T. Stanev, Astrophys. J. **479**, 290 (1997).
29. F. W. Stecker, Phys. Rev. Lett. **80**, 1816 (1998).
30. M. Takeda, N. Hayashida, K. Honda, *et al.*, Astrophys. J. **522**, 225 (1999).
31. G. A. M. Tanko, in *Proceedings of the 25th International Cosmic Ray Conference, ICRC, Durban, 1997*, Vol. 4, p. 481 (1997).
32. T. Totani, Astrophys. J. Lett. **502**, L13 (1998).
33. A. V. Uryson, Pis'ma Zh. Éksp. Teor. Fiz. **64**, 71 (1996) [JETP Lett. **64**, 77 (1996)].
34. A. V. Uryson, Zh. Éksp. Teor. Fiz. **116**, 1121 (1999a) [JETP **89**, 597 (1999a)].
35. A. V. Uryson, Izv. Akad. Nauk, Ser. Fiz. **63**, 624 (1999b).
36. A. V. Uryson, Astron. Astrophys. Trans. **20**, 347 (2001).
37. M. P. Veron-Cetty and P. Veron, ESO Scientific Report No. 13 (1993).
38. M. P. Veron-Cetty and P. Veron, <http://dbsrv.gsfc.nasa.gov/heasarc/veron98> (1998).
39. É. Ya. Vil'koviskii, private communication (2000).
40. É. Ya. Vil'koviskii and O. G. Karpova, Pis'ma Astron. Zh. **22**, 168 (1996) [Astron. Lett. **22**, 148 (1996)].
41. E. Y. Vil'koviskij, S. N. Efimov, O. G. Karpova, *et al.*, Mon. Not. R. Astron. Soc. **309**, 80 (1999).
42. A. Watson, in *Particle and Nuclear Astrophysics and Cosmology in the Next Millenium*, Ed. by E. W. Kolb and R. D. Peccei (World Scientific, Singapore, 1995), p. 126.
43. A. Watson, in *Proceedings of the International Symposium on Extremely High Energy Cosmic Rays: Astrophysics and Future Observatories*, Ed. by M. Nagano (Inst. of Cosmic-Ray Research, Tokyo, 1996), p. 362.
44. A. V. Zasov, private communication (1999).
45. G. T. Zatsepin and V. A. Kuz'min, Pis'ma Zh. Éksp. Teor. Fiz. **4**, 114 (1966) [JETP Lett. **4**, 78 (1966)].
46. V. V. Zheleznyakov, *Radiation in Astrophysical Plasma* (Yanus-K, Moscow, 1997).

*Translated by V. Astakhov*

## A Deficit of Type I X-ray Bursts from Low-Accretion-Rate Binaries: Data from the TTM/COMIS Telescope Onboard the Mir–Kvant Observatory

A. N. Emelyanov<sup>1,2\*</sup>, V. A. Aref'ev<sup>1</sup>, E. M. Churazov<sup>2,1</sup>, M. R. Gilfanov<sup>2,1</sup>, and R. A. Sunyaev<sup>2,1</sup>

<sup>1</sup> Space Research Institute, Russian Academy of Sciences, Profsoyuznaya ul. 84/32, Moscow, 117810 Russia

<sup>2</sup> Max-Planck-Institut für Astrophysik, Karl Schwarzschild Strasse 1, 86740 Garching bei München, Germany

Received July 12, 2001

**Abstract**—We analyze 175 sessions of Galactic-center observations with the TTM/COMIS telescope onboard the Mir–Kvant observatory from 1987 until 1998. Because of its wide field of view ( $\sim 15^\circ \times 15^\circ$ ), much of the Galaxy and, hence, a large number of X-ray sources were simultaneously within the telescope aperture. During the observations, 47 X-ray bursts were detected, 33 of which are most likely type I bursts related to unstable helium burning on the surfaces of neutron stars. All the detected type I bursts were identified with known X-ray sources; the pre- and post-burst luminosities of these sources measured with the TTM telescope were high. No bursts were detected from voids, i.e., from sources whose luminosities in quiescence did not exceed the TTM detection threshold. This result allows us to constrain the combination of the number of binary sources with low accretion rates and the properties of X-ray bursts from such sources, in particular, the peak luminosity during bursts and the frequency of their occurrence.

© 2001 MAIK “Nauka/Interperiodica”.

**Key words:** *Mir–Kvant, Roentgen, TTM, neutron stars, X-ray binaries, bursters, accretion, type I bursts*

### INTRODUCTION

In 1975, the SAS-3 and Ariel satellites discovered bursting X-ray sources with burst recurrence periods from several hours to several days and burst durations from several seconds to several tens or even hundreds of seconds. Such sources were called X-ray bursters. The burster flux between bursts varied slowly, and the luminosity was  $\sim 10^{36}$ – $10^{37}$  erg s<sup>-1</sup>. Woosley and Taam (1976) and, independently, Marashi and Cavaliere (1977) assumed that these X-ray bursts were attributable to unstable thermonuclear burning on the surface of a neutron star (NS) with a weak magnetic field. The radiation between bursts is mainly attributable to gas accretion onto the NS. On the NS surface, hydrogen turns into helium through the CNO cycle. As helium accumulates on the NS surface, favorable conditions arise for a thermonuclear flash to occur when the rate of energy release exceeds the rate of energy removal. The bursts that result are characterized by a sharp rise and a subsequent slower decline in the X-ray flux. Their distinctive feature is also a gradual softening of the spectrum at the flux decline phase. Such bursts were called type I bursts.

After the discovery of MXB 1730-335, which was called the Rapid Burster (Lewin 1976) and which exhibited a continuous series of bursts with a recurrence

period of  $\sim 100$  s, it became clear that to provide such a burst period required a very high accretion rate, which was not confirmed by observations. A more thorough analysis revealed that all bursts from the Rapid Burster could be separated into two classes (Hoffman *et al.* 1978). Some of the bursts were classified as type I bursts, i.e., those related to unstable helium burning; the remaining bursts were called type II bursts. When averaged over a sufficiently long period, the energy emitted in type II bursts turned out to exceed the energy emitted in type I bursts by approximately a factor of 100. The ratio of the gravitational energy released during mass accretion onto the NS surface to the energy of thermonuclear helium burning has the same order of magnitude. Thus, it was concluded that type II bursts are associated with unsteady mass accretion onto a NS and bear no relation to thermonuclear burning.

Here, we mainly investigate classical bursters, in which X-ray bursts are related to helium burning. About 50 X-ray bursters are currently known, most of which lie toward the Galactic center or in the Galactic plane (see, e.g., van Paradijs and White 1995; in't Zand 2001). Detailed overviews of the observational data and theoretical models were given by Lewin *et al.* (1993) and Bildsten (1998, 2000).

\*E-mail: emelyanov@hea.iki.rssi.ru

A catalog of X-ray bursts as compiled from the TTM/Mir–Kvant data (1987–1998)

no.	Pointing R.A.; DEC	Date of observation UT	Time of observation UT	$f_b^{\text{im}}/f_{\text{avr}}^{\text{im}}$	Burst source
1	255.022; -49.355	Mar. 24, 1989	19 <sup>h</sup> 32 <sup>m</sup> 10 <sup>s</sup> –19 <sup>h</sup> 32 <sup>m</sup> 17 <sup>s</sup>	9.2 ± 2.4	4U 1702–429
2	249.015; -39.852	Mar. 25, 1989	19 4 2–20 4 10	11.6 ± 3.4	4U 1702–429
3	267.192; -37.840	Mar. 31, 1989	19 56 12–19 56 27	3.8 ± 0.4	GX 354–0
4	266.913; -30.889	Apr. 01, 1989	19 4 6–19 4 13	15.1 ± 4.5	SLX 1744–300
5	264.108; -41.633	Apr. 02, 1989	17 56 28–20 56 35	36.1 ± 8.8	4U 1702–429
6	263.086; -27.054	Aug. 16, 1989	14 8 48–17 9 3	10.1 ± 0.9	KS 1731–260
7	262.644; -26.268	Aug. 20, 1989	12 2 37–15 2 44	10.2 ± 0.9	KS 1731–260
8	262.605; -26.455	Aug. 20, 1989	13 31 50–16 31 57	19.4 ± 5.9	MXB 1743–29
9	266.598; -32.203	Aug. 22, 1989	3 46 48–3 47 3	23.2 ± 9.3	MXB 1743–29
10	266.584; -32.398	Aug. 22, 1989	5 32 51–4 32 58	12.3 ± 3.3	A 1742–294
11	266.587; -32.711	Aug. 22, 1989	8 31 4–8 31 19	8.0 ± 0.6	GX 354–0
12	267.037; -32.776	Aug. 23, 1989	7 27 44–7 27 51	8.5 ± 1.9	A 1744–361
13	262.544; -26.464	Aug. 31, 1989	1 52 53–1 53 0	5.0 ± 0.7	KS 1731–260
14	262.610; -26.485	Aug. 31, 1989	3 12 5–3 12 12	6.8 ± 0.7	KS 1731–260
15	263.119; -26.568	Sept. 04, 1989	2 44 37–2 44 44	5.5 ± 0.9	KS 1731–260
16	269.731; -33.653	Sept. 09, 1989	4 47 29–4 47 36	10.4 ± 1.3	GX 354–0
17	269.736; -33.713	Sept. 09, 1989	7 45 28–7 45 43	6.9 ± 0.7	GX 354–0
18	265.957; -29.760	Oct. 23, 1992	23 21 20–23 21 27	7.2 ± 1.3	A 1742–294
19	266.313; -29.649	Mar. 16, 1994	13 39 42–13 39 57	21.2 ± 10.3	SLX 1744–300
20	265.989; -29.893	Mar. 18, 1994	13 25 21–13 25 36	27.7 ± 13.6	MXB 1743–29
21	265.932; -29.446	Mar. 19, 1994	12 27 8–12 27 15	4.1 ± 0.5	GX 354–0
22	266.295; -29.627	May 06, 1994	7 36 0–7 36 15	10.7 ± 2.7	A 1742–294
23	266.045; -29.743	May 09, 1994	12 23 47–12 24 10	7.9 ± 1.1	Rapid Burster
24	266.045; -29.743	May 09, 1994	12 28 11–12 28 18	6.7 ± 1.7	Rapid Burster
25	266.045; -29.743	May 09, 1994	12 30 51–12 30 58	8.9 ± 1.7	Rapid Burster
26	266.045; -29.743	May 09, 1994	12 37 41–12 37 46	7.9 ± 1.2	Rapid Burster
27	266.045; -29.743	May 09, 1994	12 42 19–12 42 26	9.4 ± 1.7	Rapid Burster
28	266.123; -29.811	May 12, 1994	14 15 53–14 16 8	6.9 ± 1.2	Rapid Burster
29	266.123; -29.811	May 12, 1994	14 18 17–14 18 32	6.1 ± 0.7	KS 1731–260
30	266.123; -29.811	May 12, 1994	14 23 29–14 23 44	9.2 ± 1.3	Rapid Burster
31	266.055; -29.828	May 12, 1994	15 55 47–15 55 54	9.1 ± 2.4	Rapid Burster
32	266.055; -29.828	May 12, 1994	16 0 51–16 1 6	15.9 ± 2.8	Rapid Burster
33	266.133; -29.869	May 15, 1994	3 56 2–3 56 17	3.4 ± 0.4	GX 354–0
34	266.073; -29.838	May 15, 1994	5 29 23–5 29 30	6.5 ± 1.7	Rapid Burster
35	266.073; -29.838	May 15, 1994	5 36 11–5 36 26	11.7 ± 2.6	A 1742–294
36	266.410; -29.625	Aug. 29, 1994	17 34 27–17 34 34	2.8 ± 0.3	GX 3+1
37	266.408; -29.882	Aug. 31, 1994	19 4 22–19 4 37	4.3 ± 0.5	GX 354–0
38	266.111; -29.573	Sept. 28, 1994	3 10 13–3 10 28	5.7 ± 0.9	KS 1731–260
39	266.037; -29.547	Apr. 02, 1994	18 55 1–18 55 8	8.8 ± 1.9	KS 1731–260
40	266.038; -29.507	Apr. 02, 1994	20 18 2–20 18 9	5.4 ± 0.8	GX 354–0
41	266.038; -29.507	Apr. 02, 1994	20 24 2–20 24 17	8.7 ± 1.6	A 1742–294
42	265.695; -29.734	Sept. 17, 1995	6 15 7–6 15 22	3.3 ± 0.4	KS 1731–260
43	265.695; -29.734	Sept. 18, 1995	11 28 47–11 28 54	5.3 ± 0.6	GX 354–0
44	266.802; -28.452	Feb. 06, 1996	2 24 17–2 24 32	27.3 ± 1.2	GRO J 1744–280
45	266.712; -28.510	Feb. 06, 1996	16 19 31–16 19 38	2.7 ± 0.2	GRO J 1744–280
46	266.801; -28.601	Mar. 01, 1996	20 5 9–20 5 24	3.2 ± 0.2	GRO J 1744–280
47	266.583; -28.442	Mar. 04, 1996	15 49 51–15 50 6	2.6 ± 0.2	GRO J 1744–280

Note:  $f_b^{\text{im}}$  is the source flux during a burst in the image (bursts),  $f_{\text{avr}}^{\text{im}}$  is the source flux in the session-averaged image.

#### OBSERVATIONS AND ANALYSIS

The Kvant module with astrophysical instruments onboard was docked with the Mir Space Station in 1987. Its payload included four instruments sensitive to photons in the energy range from 2 to 800 keV:

TTM/COMIS, HEXE, GSPC, and Pulsar X-1. TTM/COMIS (Shadow-Mask Telescope/ Coded Mask Imaging Spectrometer) was a coded-aperture telescope that could image the sky in the X-ray band.

The height of the Mir orbit was  $\sim 400$  km, its in-

clination was  $52^\circ$ , and the orbital period was 92 min. Since the charge-particle background was too strong at high latitudes and when the Brazilian anomaly was crossed, only the equatorial segment of the orbit was used for observations, and the integration time on a single turn did not exceed 26 min. The Mir orientation could be maintained over this period with an accuracy of the order of one arcminute. At each instant of time, only a  $20^\circ$ -wide band of the sky along the Mir orbital plane was observable (this restriction was imposed by the solar-panel orientation). Since the orbital plane precessed with a period of 2.5 months, in general, only regions around the north and south celestial poles were inaccessible to the Mir instruments.

The TTM X-ray telescope (Brinkman *et al.* 1985) used a coded mask as the entrance aperture to determine the source positions. The instrument operated in the energy range 2–30 keV with a  $15^\circ \times 15^\circ$  total field of view. The detector geometric area was  $655 \text{ cm}^2$ . The nominal angular resolution per mask cell was  $\sim 2$  arcmin, and the TTM energy resolution was 18–20% at energy 6 keV. The TTM detector was a multi-wire proportional counter that recorded the energy, coordinates, and arrival times of X-ray photons.

In our analysis, we used 175 sessions (from  $\sim 1500$ ) of TTM observations when the telescope was pointed toward the Galactic-center region. The total exposure time in these observations was  $\sim 1.7 \times 10^5 \text{ s}$ . Since the TTM star tracker was inoperational beginning in 1989, the accurate pointing of the telescope was determined from the positions of bright X-ray sources with known coordinates. The TTM source location accuracy of bright X-ray sources was higher than  $\sim 30$  arcsec.

Information on the charged-particle background and on the TTM detector load was recorded by five counters whose data were read every 8 s. It is this information that was used to search for X-ray bursts. Figure 1 shows the typical light curve during a session of Galactic-center observations recorded by these counters: the X-ray photon and charged-particle count rates are shown in panels (a) and (b), respectively. The increase in charged-particle count rate at the end of the session stemmed from the fact that the satellite approached high latitudes, at which the charged-particle background was appreciably higher. An increase in charged-particle count rate caused a decrease in detector efficiency because of the dead time and, accordingly, a smooth decrease in X-ray photon count rate by the end of the session, which is clearly seen in panel (a). When searching for X-ray bursts, we fitted the photon count rate by a fourth-degree polynomial (smooth curve). Spikes by more than five standard deviations above the analytic fit were singled out for a more thorough analysis.

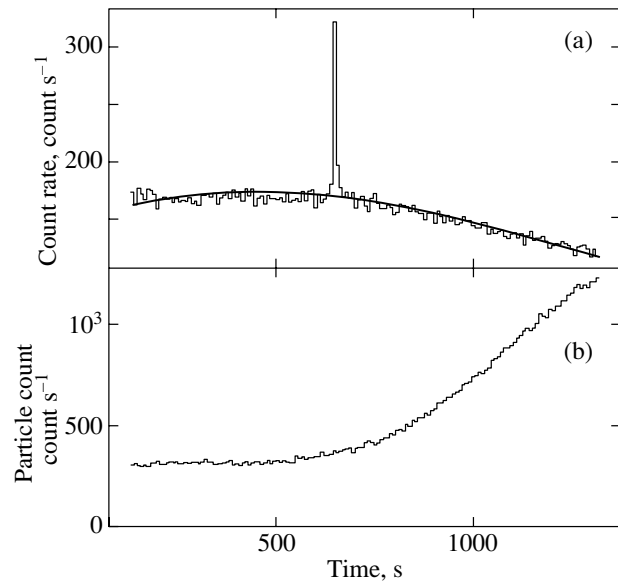


**Fig. 1.** The light curve during a session of Galactic-center observations: (a) the X-ray photon count rate and (b) the charged-particle count rate (see the text for a detailed explanation). The burst seen on the light curve belongs to the burster GX 354-0.

First, we analyzed the behavior of the charged-particle background in an effort to exclude false triggerings unrelated to X-ray bursts. Subsequently, we constructed an image from the observational data over the entire session and during a burst. A comparison of the source fluxes during a burst and over the entire session allowed the burst source to be uniquely identified. In particular, the burst detected during the session shown in Fig. 1a is associated with the well-known burster GX 354-0 (see Fig. 2).

A catalog of detected bursts is presented in the table: it gives burst numbers, TTM pointings during sessions (the position of the TTM field of view at epoch 2000), session dates, burst detection times and durations, and ratios of the flux during a burst ( $f_b^{\text{im}}$ ) to the average source flux during the entire session ( $f_{\text{avr}}^{\text{im}}$ ). Note that although the TTM time resolution was 1 s, we used information with a time resolution of 8 s to construct images and to analyze the light curves. This is because the telemetric channel capacity was limited; information on no more than 224 events per second were transmitted to Earth through this channel. The typical count rates during observations of the Galactic-center region containing several very bright sources and, in particular, during an X-ray burst appreciably exceeded this value. As a result, some of the X-ray events and detailed information on their temporal structure were lost during data transmission to the Earth. Therefore, we determined

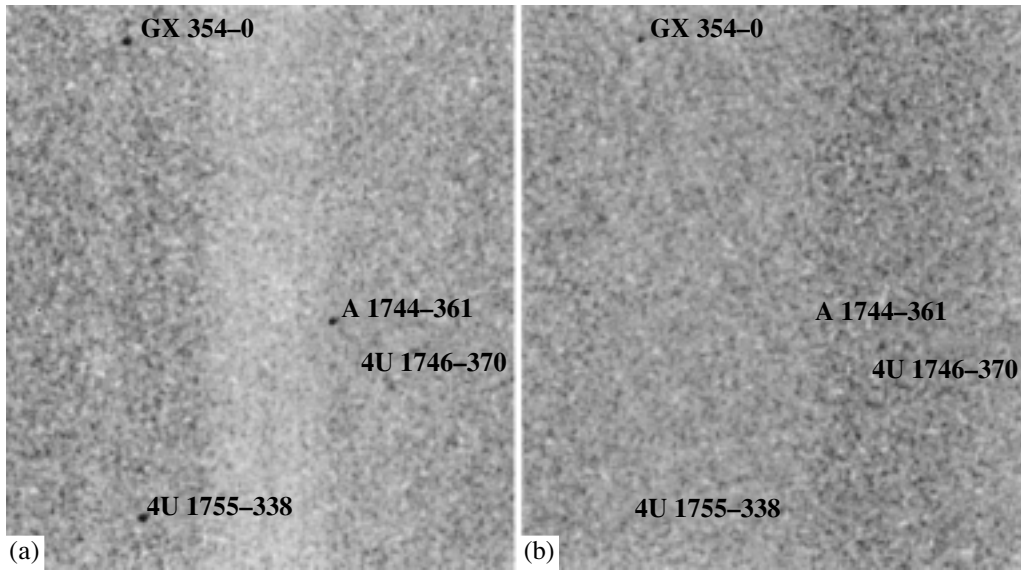


**Fig. 2.** Images of the Galactic-center region: (a) the session-averaged image ( $\sim 20$  min); (b) the burst image (averaged over 8 s). A burst from the burster GX 354-0 is clearly seen in the 8-s-averaged image.

the burst beginning and end by using readings from onboard TTM counters (see above) with a resolution of 8 s. A correction for the losses related to the telemetric channel capacity was made by comparing the onboard counter readings and the 8-s-averaged photon count rate in the telemetric information.

As we see from the table, 47 bursts were detected during the observations: 33 type I bursts, 10 bursts from MXB 1730–335 (Rapid Burster), and 4 bursts from the transient pulsar GRO J1744–280, which also exhibits flaring activity (Bildsten and Brown 1997; Strohmayer *et al.* 1997). Here, the classification of bursts as type I bursts is based only on the identification of bursts with known classical bursters. We do not perform a detailed analysis of the burst spectral evolution, which is of no crucial importance in the context of our study. Note that the TTM telescope detected one burst from A 1744–361. Judging by published data, this is the first detection of a burst from A 1744–361, which strongly suggests the existence of an accreting neutron star in this source.

Apart from the 47 bursts listed in the table, we found features on the light curves in two more events, which suggest the presence of X-ray bursts. However, we found no convincing peaks in the images constructed at the burst time that were indicative of a cosmic nature of these bursts: either these bursts are related to charged-particle background variations or the TTM sensitivity is too low to localize the burst source. These two events were rejected and are not considered below.

## DISCUSSION

According to the standard model of type I X-ray bursts, helium accumulates on the stellar surface during mass accretion onto a neutron star, which results in explosive energy release when a critical surface density,  $C_{cr}$ , is reached. The critical surface density depends on the accretion rate, on the chemical composition of the accreted matter, and on the temperature of deep NS shells (Bildsten 1998, 2000). At high accretion rates approaching the Eddington value, the helium shell heats up, and stable burning without bursts begins. The brightest binaries in the Galactic-center region, such as, for example, GX 5–1, are definitely not sources of X-ray bursts. At lower accretion rates, unstable burning is virtually inevitable. The sources with medium accretion rates (luminosities  $\leq 0.01$ – $0.1L_{Edd}$ ) are classical bursters. A sizeable fraction of the bursts from such sources have a peak luminosity of the order of the Eddington luminosity. The critical surface density  $C_{cr}$  not only becomes lower but even increases with decreasing accretion rate. Therefore, binaries with even lower accretion rates can potentially be the sources of rare but, possibly, stronger type I bursts. In quiescence, the luminosity of such sources is too low (because of accretion) to be detectable by TTM at a distance of  $\sim 8.5$  kpc. During a burst, however, if the peak luminosity is comparable to the Eddington luminosity, such sources can be easily detected. If the luminosity function is such that the number of low-accretion-rate (low-luminosity) sources is very large, then, in addition to bursts from comparatively bright (in quiescence) sources, the TTM telescope must

detect bursts from voids. As was noted above, the sources of all the bursts detected by TTM are also visible in quiescence. The absence of bursts from voids allows us to impose constraints on the number of low-accretion-rate sources and on the time it takes for them to accumulate helium for a burst. Below, we briefly discuss these constraints.

### *The TTM Sensitivity to Sources in Quiescence (as Inferred from the Image)*

The duration of a TTM observing session was typically 15–20 min. When observing regions without bright X-ray sources, the TTM sensitivity (in 20 min of observations) was  $\sim 7$ – $10$  mCrab ( $5\sigma$ ). In the TTM energy range (2–20 keV), 1 mCrab is  $\sim 3 \times 10^{-11}$  erg s $^{-1}$  cm $^{-2}$ . However, when observing the Galactic-center region, several very bright sources, such as GX 5–1, GX 3+1, and GX 9+1, were within the TTM field of view. An increase in the X-ray photon count rate and a saturation of the telemetric channel caused the sensitivity to decrease appreciably. The sensitivity (during a single session) when observing the Galactic-center region was typically  $\sim 15$ – $20$  mCrab at the center of the field of view. For a source at a distance of 8.5 kpc, this value (15 mCrab) corresponds to a luminosity  $\sim 4 \times 10^{36}$  erg s $^{-1}$  and an accretion rate  $\sim 3 \times 10^{-10} M_{\odot}$ /year (when the conversion efficiency of the rest mass of accreted material to radiation is 0.2). Weaker sources cannot be reliably detected during a single observing session. It should be noted that the transformation coefficient of the TTM flux to the bolometric luminosity depends on the spectral shape of the source and the low-energy absorption associated with neutral or molecular gas on the line of sight. The uncertainty in this transformation can reach a factor of 2 or 3. However, for order-of-magnitude estimates, this accuracy is quite sufficient.

### *The TTM Sensitivity to X-ray Bursts (as Inferred from the Light Curves and the Image)*

As was already noted above, we searched for X-ray bursts by analyzing the TTM X-ray photon count rates with an 8-s resolution. The detection threshold of 5 standard deviations (the excess over the smooth analytic fit) roughly corresponds to an increase in the source flux by 200–300 mCrab, depending on the background conditions and on the source position within the TTM field of view. For a source at the center of the TTM field of view, the sensitivity in the image reconstructed during a burst (in 8 s) is  $\sim 20\%$  lower, 300–400 mCrab.

Most of the observed type I bursts have a peak luminosity that account for a fraction  $f = 0.1$ – $1$  of the Eddington luminosity for a neutron star (Lewin

*et al.* 1993, 1995). For a burst that maintains the Eddington luminosity for 8 s, the TTM telescope can reliably detect such a burst (both in the light curve and in the image) provided that the distance to the source does not exceed 9.5 kpc.

We can estimate the fraction of the bursters whose bursts must be reliably detected with TTM by assuming that the burst has the Eddington luminosity and that the distribution of low-mass X-ray binaries follows the distribution of visible stars in the Galaxy. As the distribution of stars in the Galaxy, we may choose the three-component model by Bahcall and Soneira (1986), which consists of a spheroid, a disk component, and a bulge. Most of the bursters lie toward the Galactic center or in the Galactic plane (van Paradijs 1995). When observing the Galactic-center region, according to the three-component model, the volume bounded by the  $15^{\circ} \times 15^{\circ}$  TTM field of view and by a distance of 9.5 kpc contains 0.28 of the total mass of the Galactic stars. Allowance for the decrease in sensitivity to the edge of the field of view yields 0.17 of the total Galactic mass. Thus, we conclude that when observing the Galactic center, the TTM telescope simultaneously monitored  $\approx 17\%$  of all the potential burst sources in the Galaxy.

### *Constraints on the Number of Low-Accretion-Rate Sources*

As was said above, all type I bursts (33 events) detected by TTM were identified with sources whose fluxes in quiescence were significant. No burst was detected from a source whose flux in quiescence did not exceed the TTM detection threshold. Let us estimate the expected number of such sources.

The number of bursts from sources with fluxes in quiescence above the TTM detection threshold is

$$N_{b,p} = \int_0^{\infty} \frac{dM}{dr} dr \int_{4\pi r^2 S_p}^{\infty} P_b \times (L, L_b > 4\pi r^2 S_b) \frac{dN}{dL} dL, \quad (1)$$

where  $dM/dr$  is the source density distribution (per unit distance) in distance  $r$  within the TTM field of view,  $S_p$  is the TTM detection threshold for a source in quiescence,  $dN/dL$  is the luminosity function of sources in quiescence, and  $P_b (L, L_b > 4\pi r^2 S_b)$  is the generation rate of X-ray bursts (with fluxes above the burst detection threshold  $S_b$ ) by a source with luminosity  $L$  in quiescence.

The number of bursts from sources with fluxes in quiescence below the TTM detection threshold is, respectively,

$$N_{b,e} = \int_0^{\infty} \frac{dM}{dr} dr \int_0^{4\pi r^2 S_p} P_b \quad (2)$$

$$\times (L, L_b > 4\pi r^2 S_b) \frac{dN}{dL} dL.$$

Below, we consider not the absolute values of  $N_{b,p}$  and  $N_{b,e}$  but their ratio.

The simplest estimate can be obtained by assuming that all sources are at the same distance (e.g., at the Galactic-center distance, 8.5 kpc) and that all the emerging X-ray bursts have approximately equal luminosities of the order of the Eddington luminosity (such bursts must be detected by TTM up to distances  $\sim 9.5$  kpc). In that case,

$$\frac{N_{b,e}}{N_{b,p}} = \frac{\int_0^{4\pi r^2 S_p} P_b(L) \frac{dN}{dL} dL}{\int_{4\pi r^2 S_p}^{\infty} P_b(L) \frac{dN}{dL} dL}. \quad (3)$$

This simplified expression depends only on the source luminosity function and on the rate of burst generation by sources with specified luminosities. This expression can be further simplified by assuming that a fixed amount of accreted matter is required for a burst to occur, i.e.,  $P_b(L) \propto \dot{M}/\Delta M \propto L$ . In that case,

$$\frac{N_{b,e}}{N_{b,p}} = \frac{\int_0^{4\pi r^2 S_p} L \frac{dN}{dL} dL}{\int_{4\pi r^2 S_p}^{\infty} L \frac{dN}{dL} dL}. \quad (4)$$

In this approximation, the ratio of the numbers of bursts from weak and strong sources reduces to the ratio of the total rates of accretion onto the set of all weak and strong sources, respectively. At  $N_{b,p} = 33$  and  $N_{b,e} < 3^1$ , this estimate leads us to conclude that the total rate of accretion onto sources with luminosities below  $\sim 4 \times 10^{36}$  erg s $^{-1}$  is at least a factor of 10 lower than the total rate of accretion onto stronger sources; i.e., relation (4) reflects the contribution of bright and faint sources to the total Galactic luminosity. The luminosity function can be fitted by a power law with a slope  $\sim 1.5$ :  $dN/dL \propto L^{-1.5}$  (Grimm *et al.* 2001) up to luminosities of  $10^{38}$  erg s $^{-1}$ , above which the luminosity function falls sharply. In reality, the upper integration limit must be chosen even lower ( $L \sim 5 \times 10^{37}$  erg s $^{-1}$ ), because no X-ray bursts occur at higher luminosities (accretion rates). In that case,  $N_{b,e}/N_{b,p} \approx 0.3$ ; i.e., it is several times higher than the upper limit estimated from observations. Thus, given our simplifications, the observed deficit of bursts from weak sources either suggests a flatter luminosity function or allows

<sup>1</sup>The absence of bursts from weak sources over the observing period implies that, at 95% confidence, the mean expected number of bursts from such sources over this period does not exceed 3.

the generation rate and properties of bursts from low-accretion-rate sources to be judged.

There are several reasons why bursts from low-accretion-rate sources can be absent. Below, we consider the most obvious ones.

(1) First, a situation is possible where there are simply no sources with accretion rates lower than some value. For example, even for a comparatively weak magnetic field on the NS surface, the source can pass to a propeller state (Illarionov and Sunyaev 1975). In this state, matter is thrown away from the star and does not reach its surface. For a magnetic-field strength  $B \sim 10^8$  G and for a NS spin period  $P \sim 10^{-2}$  s, the propeller effect arises at a luminosity of  $\sim 4 \times 10^{34}$  erg s $^{-1}$ .

(2) Another natural explanation is a sharp increase in the accreted-matter surface density required for the generation of a burst (Ayasli and Joss 1982; Wallace *et al.* 1982). In reality, the absence of bursts from weak sources imposes a constraint only on the product of the burst occurrence frequency and the number of weak sources, provided that the characteristic burst parameters, such as the peak X-ray flux and the burst duration, do not strongly depend on the luminosity in quiescence.

(3) Finally, the peak X-ray luminosity of bursts from weak sources may be appreciably lower than the peak luminosity of bursts from classical bursters. For example, when observing the source EXO 0748–676 (Gottwald *et al.* 1986, 1987), whose luminosity varied approximately by a factor of 5, the peak luminosity of the detected bursts was found to generally decrease with decreasing luminosity in quiescence. A similar pattern was observed when studying some other sources. In the calculations by Taam *et al.* (1993), this behavior of the peak fluxes was explained by a complex and irregular pattern of sequential X-ray bursts on the NS surface accompanied by the incomplete consumption of thermonuclear fuel. It followed from the calculations that this regime was realized at accretion rates higher than several  $10^{-10} M_{\odot}$  per year. At lower accretion rates, bursts occurred more regularly; their peak luminosity increased appreciably. The theoretical pattern of burst generation at low accretion rates is very complex, and there is no unique answer to the question of what the characteristic parameters of bursts from weak sources are.

Thus, we can slightly reformulate the results of our TTM observations: all sources from which bursts were observed have luminosities in quiescence within the range from several  $10^{36}$  to several  $10^{37}$  erg s $^{-1}$  (to estimate the luminosity, we used the known distances to several best studied sources and assumed the distances to the remaining sources to be 8.5 kpc). Thus, we reach a conservative conclusion that of

$\sim 30$  detected bursts from sources with luminosities  $L \sim 10^{37} \text{ erg s}^{-1}$  in the luminosity band  $\Delta L \sim L$ , we detected no burst with a comparable (or higher) peak luminosity from sources with lower luminosities in quiescence.

The above estimates are very rough. We only wanted to show that a more thorough analysis of the detection statistics of X-ray bursts from bright and faint sources was needed. Such an analysis can give important information for constructing models of unstable thermonuclear burning on weakly accreting neutron stars. Since the time between bursts for such sources can be very large, even long-duration observations of individual sources cannot provide the necessary information. A different approach based on the simultaneous monitoring of many sources is required to search for and study bursts from weak sources. Consequently, we need observations by X-ray telescopes with wide fields of view that cover large areas of the sky, in contrast to typical observations of small sky areas containing the well-known burster. The efficiency of telescopes in searches for bursts from low-accretion-rate sources is determined by three factors: the sensitivity to bursts, the size of the field of view, and the total integration time. Assuming the distribution of binary sources to roughly follow the mass distribution in the Galaxy, the expected number of bursts is proportional to the product of the observing time by the mass of the matter within the telescope field of view and at the distance determined by the telescope sensitivity to bursts. Since the Galactic center is the region of the highest concentration of sources in the Galaxy, it makes sense to talk about observations exactly of this region. At present, the best results can be obtained by using data from the BeppoSAX wide-field camera (Jager *et al.* 1997).

The BeppoSAX wide-field camera (WFC) is sensitive to photons in the energy range 1.8–28 keV and has a  $20^\circ \times 20^\circ$  field of view (FWHM), although a source can be detected with a lower sensitivity within a  $40^\circ \times 40^\circ$  total field of view (Jager *et al.* 1997). The BeppoSAX sensitivity at a  $5\sigma$  level is  $\sim 200$  mCrab in 8 s. Consequently, it can detect a burst (with the Eddington luminosity) at a distance of  $\sim 11.7$  kpc. Taking into account its field of view, we find that it observes  $\approx 0.4\text{--}0.5M_{\text{gal}}$ . The total exposure time of the WFC Galactic-center observations was  $4 \times 10^6$  s from 1996 until 2000 (in't Zand 2001), during which more than 2000 bursts were detected from low-mass X-ray binaries:  $\sim 400$  bursts belong to the Rapid Burster MXB 1730–335 and  $\sim 200$  bursts belong to the bursting pulsar GRO J1744–280 (Ubertini 2000). The WFC telescope detected a total of  $\approx 1500$  type I bursts from 35 classical bursters (compared to  $\approx 30$  bursts detected by TTM), which accounts for  $\sim 75\%$  of the total number of bursters

(in't Zand 2001). Thus, the WFC/BeppoSAX data provide the most comprehensive information on bursts from weak sources. Indeed, this telescope detected several bursts from sources whose fluxes in quiescence were below the detection threshold (in't Zand *et al.* 1998). Given the total number of bursts detected by the WFC telescope, the detection of several bursts from voids is consistent with the TTM results: it follows from a comparison of the TTM and WFC burst detection statistics that the expected number of bursts from weak sources during the TTM observations is  $\approx 0.1\text{--}0.2$ . Below, we discuss the possibility of using the burst occurrence statistics to obtain information on the time of matter accumulation on the NS surface.

#### *The Mass of the Matter Accumulated by the Source before a Burst*

In this section, we discuss the possibility of determining (from experimental data) the mass of the matter accumulated on the NS surface that is required for the generation of an X-ray burst. Assume that the distance to the burst source is known. For bursts whose peak luminosities reach the Eddington level, the distance can be determined directly from observations of the burst itself. For typical bright bursters, the mass of the accumulated matter can be calculated from the flux in quiescence,  $F_X = L_X/(4\pi D^2) = \eta \dot{M} c^2$ , and the time interval  $\tau$  between sequential bursts, i.e.,  $\Delta M \approx \tau(F_X 4\pi D^2/\eta)$ . For very weak sources, the time between sequential bursts is too large (it can exceed several months or even several tens of years), and it is not possible to observe sequential bursts. However, this information can be obtained by analyzing the detection statistics of bursts from sources with various luminosities in quiescence. A simple expression for the accumulated mass is derived if two assumptions are made: the source luminosity function  $dN/dL$  in quiescence is known, and, irrespective of the source luminosity, the bursts have sharp fronts and equal peak luminosities. Denote the number of bursts from sources with luminosities (in quiescence) in the range from  $L$  to  $L + dL$  detected by the telescope when observing a given area of the sky in a certain time interval by  $dN_b/dL$ . It is then clear that

$$\Delta M(L) \propto L \frac{dN/dL}{dN_b/dL} \Delta t. \quad (5)$$

When determining the form of  $\Delta M(L)$ , we can use the set of all telescope observations, irrespective of the exposure time and the telescope pointing.<sup>2</sup> The only

<sup>2</sup>A more detailed analysis is required to determine the numerical coefficient of the luminosity dependence of the accumulated mass  $[\Delta M(L)]$ .

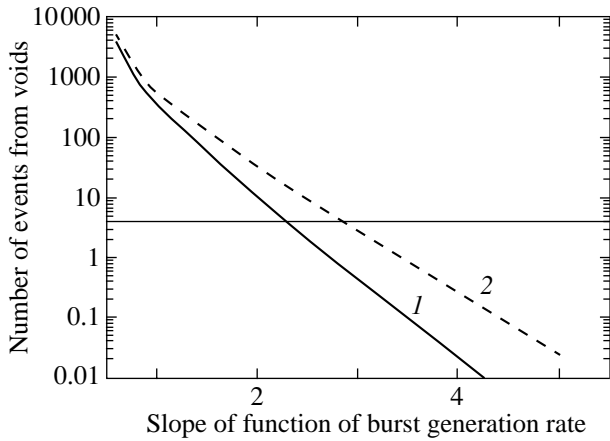


**Fig. 3.** The number of expected bursts from voids versus slope of the function of burst generation rate: (1) for  $L_{\text{gran}} = 10^{38} \text{ erg s}^{-1}$  and (2) for  $L_{\text{gran}} = 5 \times 10^{37} \text{ erg s}^{-1}$ .

requirement is a wide field of view of the telescope lest a single peculiar source give a dominant contribution to the total number of observed bursts.

In principle, such information can be obtained from the WFC data. Clearly,  $\Delta t / (dN_b / dL)$  is the reciprocal of the X-ray burst generation rate  $P_b(L)$  [formulas (1)–(3)]. Thus, if we estimate  $P_b(L)$  more accurately than when we derived formula (4), then we obtain an estimate of the mass accumulated by the source before the generation of bursts using a power-law fit to the luminosity function with an index  $\sim -1.5$  (Grimm *et al.* 2001).

To a first approximation, we can obtain such an estimate by using the BeppoSAX results on bursts from persistent sources and on bursts from voids (in't Zand 2001). Assume that the burst generation rate is represented as  $L^\beta$  for  $L < L_{\text{gran}}$ , where  $L_{\text{gran}}$  is the luminosity (close to the Eddington luminosity) up to which X-ray bursts are observed. Substituting the three-component model by Bahcall and Soneira (1986), the power luminosity function with a slope of  $-1.5$ , and the proposed function of burst generation rate in formulas (1) and (2) and performing integration over the region observed by BeppoSAX within its sensitivity range, we then obtain the expected number of bursts from voids as a function of the parameter  $\beta(L_{\text{gran}})$ . Figure 3 shows the curves for the expected number of bursts from voids for limiting luminosities of  $10^{38} \text{ erg s}^{-1}$  (curve 1) and  $5 \times 10^{37} \text{ erg s}^{-1}$  (curve 2). We see that  $\beta$  at which the observed number of bursts from voids is reached is  $\approx 2.5$ . In that case,  $\Delta M(L) \propto L^{-3.0}$ . This result is consistent with theoretical calculations, which predict a sharp increase in the accumulated mass required for the

generation of a burst at low accretion rates and a decrease in the amount of the accreted matter required for the generation of a burst at high accretion rates (Bildsten 1998, 2000). The intensities of the bursts themselves also change (increase for long integration times and decrease for short integration times).

However, there are several technical difficulties that limit the efficiency of such an analysis: (1) the WFC telescope carried out observations in separate, short time intervals, and we cannot rule out the possibility that the source luminosity was slightly higher than at the time when no observations were performed; (2) the upper limits on the source luminosity in quiescence were not very stringent (for a source at a distance of 8.5 kpc, the upper limit on the luminosity in quiescence is  $\approx 10^{36} \text{ erg s}^{-1}$ ). The most effective strategy seems to be continuous observations of large sky areas with X-ray monitors to detect the bursts themselves and to roughly localize them supplemented with direct observations of the source with high-sensitivity telescopes to accurately determine its luminosity in quiescence. Such a problem can be effectively solved by the Spectrum–X–Gamma observatory, which includes both the MOXE all-sky monitor and several high-sensitivity telescopes, JET–X or SODART.

## CONCLUSIONS

During our TTM/Mir–Kvant observations of the Galactic-center region, we detected 47 X-ray bursts, most of which can be classified as type I bursts associated with unstable helium burning on the NS surface. One of the bursts was detected from the source A 1744–361. Judging by published data, this is the first detection of a burst from A 1744–361, which strongly suggests the existence of an accreting neutron star in this source.

All the detected bursts were identified with known X-ray sources; the pre- and post-burst luminosities of these sources measured by the TTM telescope was fairly high. No burst was detected from voids, i.e., from sources whose luminosities in quiescence did not exceed the TTM detection threshold. The absence of bursts from weak sources allows us to constrain the combination of the number of binary sources with low accretion rates and the properties of X-ray bursts from such sources, more specifically, the peak luminosity during bursts and the frequency of their occurrence. The occurrence statistics of bursts from low-accretion-rate sources can be analyzed in detail by the Spectrum–X–Gamma observatory, which includes the MOXE all-sky monitor and several high-sensitivity telescopes, JET–X or SODART.

## ACKNOWLEDGMENTS

We wish to thank S. Mol'kov and A. Lutovinov for valuable advice and remarks, V.G. Rodin, A.V. Prudkoglyad, and the staff of the Flight Control Center, which operated the Mir Station and the instrumentation. We are also grateful to A.N. Ananenkova for a preliminary telemetric data reduction. This study was supported in part by the Russian Foundation for Basic Research (project nos. 00-15-96649 and 01-02-17295).

## REFERENCES

1. S. Ayasli and P. Joss, *Astrophys. J.* **256**, 637 (1982).
2. N. Bahcall and R. Soneira, *Astrophys. J.* **311**, 15 (1986).
3. L. Bildsten, astro-ph/9709094 (1997); in *The Many Faces of Neutron Stars*, Ed. by R. Buccheri, J. van Paradijs, and M. A. Alpar (Kluwer, Dordrecht, 1998).
4. L. Bildsten, in *Rossi2000: Astrophysics with the Rossi X-ray Timing Explorer* (NASA Goddard Space Flight Center, Greenbelt, 2000), p. E65.
5. L. Bildsten and E. Brown, *Astrophys. J.* **477**, 897 (1997).
6. A. Brinkman, J. Dam, W. Mels, *et al.*, in *Non-Thermal and Very High Temperature Phenomena in X-ray Astronomy*, Ed. by G. C. Perola and M. Salvati (Institute Astronomico, Rome, 1985), p. 263.
7. M. Gottwald, F. Haberl, A. Parmar, and N. White, *Astrophys. J.* **308**, 213 (1986).
8. M. Gottwald, F. Haberl, A. Parmar, and N. White, *Astrophys. J.* **323**, 575 (1987).
9. S. Grebenev, A. Lutovinov, M. Pavlinskiĭ, *et al.*, Preprint Pr-2031, IKI RAN (Inst. for Space Research, Russian Academy of Sciences, Moscow, 2000).
10. Grimm, M. Gifanov, and R. Sunyaev, 2001 (in press).
11. J. Hoffman, H. Marshall, and W. Lewin, *Nature* **271**, 630 (1978).
12. A. Illarionov and R. Sunyaev, *Astron. Astrophys.* **39**, 185 (1975).
13. J. in't Zand, J. Heise, J. Muller, A. Vazzano, M. Cocchi, L. Natalaucci, and P. Ubertini, *The Active X-ray Sky: Results from BeppoSAX and RXTE*, Ed. by L. Scarsi *et al.* (Elsevier, Amsterdam, 1998); J. in't Zand, astro-ph/0104299 (2001).
14. R. Jager, W. Mels, A. Brinkman, *et al.*, *Astron. Astrophys., Suppl. Ser.* **125**, 557 (1997).
15. W. Lewin, *IAU Circ.*, No. 2922 (1976).
16. W. Lewin, J. van Paradijs, and R. Taam, *Space Sci. Rev.* **62**, 223 (1993).
17. W. Lewin, J. van Paradijs, and R. Taam, in *X-ray Binaries*, Ed. by W. Lewin *et al.* (Cambridge Univ. Press, Cambridge, 1995), p. 175.
18. L. Marashi and A. Cavaliere, *Highlights Astron.* **4** (1), 127 (1997).
19. T. Strohmayer, K. Jahoda, B. Giles, and U. Lee, *Astrophys. J.* **486**, 355 (1997).
20. P. Ubertini, in *Proceedings of the Integral Science Working Meeting no. 17, 2000*.
21. J. van Paradijs, *X-ray Binaries*, Ed. by W. Lewin, J. van Paradijs, and E. van der Heuvel (Cambridge Univ. Press, Cambridge, 1995), p. 536.
22. J. van Paradijs and N. White, *Astrophys. J. Lett.* **447**, L33 (1995).
23. R. Wallace, S. Woosley, and T. Weaver, *Astrophys. J.* **258**, 696 (1982).
24. S. Woosley and R. Taam, *Nature* **263**, 534 (1976).

*Translated by V. Astakhov*

## Correlation between Break Frequency and Power-Density Spectrum Slope for the X-ray Source Cygnus X-2: RXTE/PCA Data

S. I. Kuznetsov\*

*Space Research Institute, Russian Academy of Sciences, Profsoyuznaya ul. 84/32, Moscow, 117810 Russia*  
*CEA, DSM/DAPNIA/SAP Centre d'Etudes Nucleaires de Saclay, 91191 Gif-sur-Yvette Cedex, France*

Received June 25, 2001

**Abstract**—We present RXTE observations of the X-ray source Cyg X-2 during 1996–1999. Its power-density spectra in the 0.1–128-Hz band are fitted by a model that takes into account the power-law spectral behavior at frequencies below and above the break frequency, with an introduction of one or more Lorenz lines to describe the peaks of quasi-periodic oscillations that correspond to the horizontal branch of the Z track. The RXTE observations revealed a positive correlation between the break frequency and the indices of the two parts of the spectrum. The spectrum steepens with increasing break frequency both above and below the break frequency. © 2001 MAIK “Nauka/Interperiodica”.

Key words: X-ray and gamma-ray sources, Cygnus X-2

### INTRODUCTION

Cygnus X-2 belongs to low-mass binaries with accreting neutron stars and is one of the brightest X-ray sources. By its spectral characteristics, Cyg X-2 belongs to the class of Z-type sources (Hasinger and van der Klis 1989), which are characterized by a Z-shaped track in the color–color diagram. In this interpretation, the spectral properties are presented in the hard–soft color indices, each of which is the harder-to-softer flux ratio in the corresponding energy band. The Z-shaped track is commonly divided into three parts called branches: the horizontal (HB, the upper part of the diagram), normal (NB, the intermediate part), and flaring (FB, the lower part) branches. The position along the Z track is generally believed to be associated with an increase in the rate of mass accretion in the direction from HB to FB. Six sources are currently known to exhibit Z tracks in the color-color diagram: Scorpius X-1, Cygnus X-2, GX 17+2, GX 5-1, GX 340+0, and GX 349+2.

The power-density spectra (Fourier transforms of the flux) of Z-type sources exhibit low-frequency (5–100 Hz) quasi-periodic oscillations (QPOs) of the X-ray flux. The names of the QPOs correspond to the branch with which their origin is identified: horizontal- (HBO), normal- (NBO), and flaring-branch (FBO) oscillations. HBOs (15–100 Hz) can also be detected in the NB spectral state. However, as one recedes from HB, the significance of

the QPO peaks decreases, and they become undetectable. When moving along the Z track in its NB–FB segment, a QPO peak in the range 5–20 Hz (NBO/FBO) emerges in the power-density spectra.

All three types of QPOs characteristic of the low-frequency part (< 100 Hz) of the power-density spectrum have been detected for the source Cyg X-2. The NBO and FBO frequencies are very close to the break frequency, which introduces a large uncertainty in its determination. For this reason, we excluded from our analysis those observations in which NBO/FBOs were detected.

### DATA AND OBSERVATIONS

For our time analysis, we used the archival data of the PCA (Proportional Counter Array) instrument (Jahoda *et al.* 1996) onboard the RXTE observatory (Bradt *et al.* 1993) retrieved from the Goddard Space Flight Center Electronic Archive.

The X-ray source Cyg X-2 was observed at the RXTE observatory during nine series of directed observations (10063, 10065, 10066, 10067, 20053, 20057, 30046, 30418, 40017): in March, August, October 1996, June, July, September 1997, July 1998, and in separate sessions from July until October 1998 and from January until August 1999. The observations of Cyg X-2 over this period correspond to three different observational epochs of RXTE/PCA (2, 3, and 4 in the adopted classification), for which the boundaries of the PCA energy channels were changed.

\*E-mail: sik@hea.iki.rssi.ru

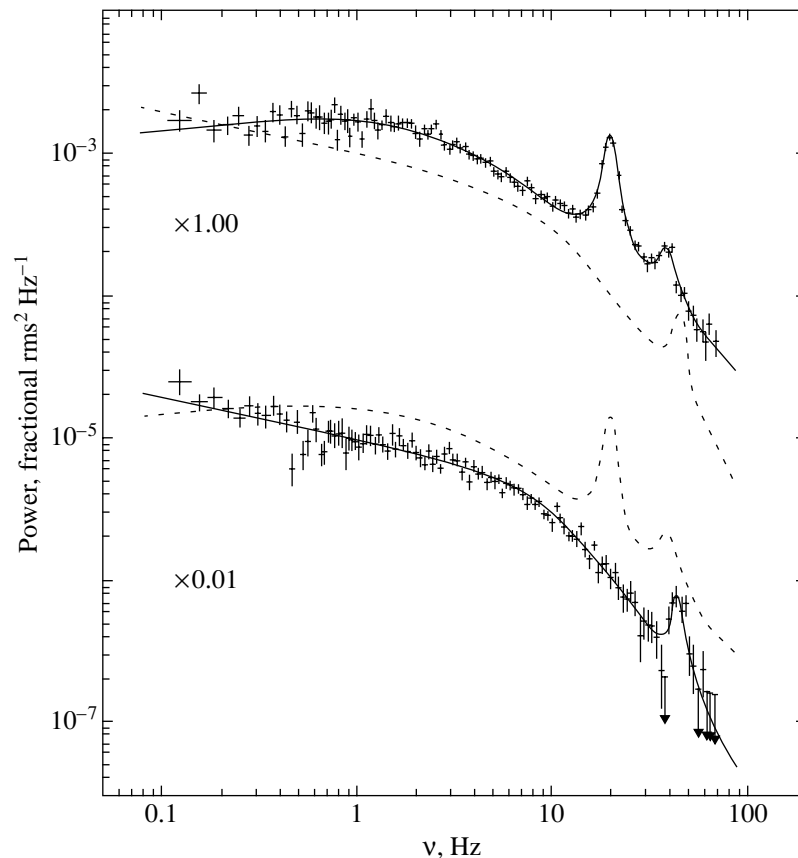


**Fig. 1.** Two power-density spectra for Cyg X-2 in the 5–60-KeV energy band. The power of the lower spectrum was reduced by a factor of 100. The spectra are fitted by the break model and by Lorenz lines (solid curves); the dotted lines represent scalable fits to each of the spectra. The peaks in the upper and lower spectra correspond to the first and second harmonics of HBOs and only to its first harmonic, respectively.

To construct the power-density spectra, we used observations with a resolution of  $\sim 122 \mu\text{s}$  ( $2^{-13}$  s) from the 14th to 249th PCA energy channels. This range corresponds to the flux of detectable photons up to  $\sim 60$  keV, whose lower limit begins from  $\sim 4.3$  keV,  $\sim 5.0$ – $5.3$  keV, and  $\sim 5.8$  keV for epochs 2, 3, and 4, respectively. In this energy band, the detection of QPOs corresponding to the horizontal branch of the Z track is most significant. The power-density spectra were obtained by the standard method of Fast Fourier Transform (van der Klis 1989).

We combined the observational data that were not represented by a single format for all channels from 14th to 249th. Of all the observations, we used only those during which the angle between the source direction and the horizon of the Earth was more than  $10^\circ$  and the PCA axis was offset from the target by no more than  $0.02^\circ$ . Among the observations of Cyg X-2, all five proportional counters were not always switched on to record events. If the operating condition of one of the counters changed during a continuous observation (whose duration did not ex-

ceed the duration of one orbit and was, on the average,  $3 - 3.5 \times 10^3$  s), then the short time interval during which the total count rate changed abruptly was excluded from the analysis. Because of this filtering, the total usable observational time for Cyg X-2 was more than  $4 \times 10^5$  s.

To analyze the low-frequency ( $< 100$  Hz) variability of Cyg X-2, we constructed power-density spectra in the range 0.03125–128 Hz. No corrections were made for background radiation and for dead time (attributable to the instrumental delay in recording events).

## RESULTS

Fitting the power-density spectra by a constant and by a power law at frequencies below and above the break frequency did not yield acceptable results (according to the  $\chi^2$  test). The main reason was the absence of a sharp break and the uncertainty in the measurement of its position in the power-density spectrum. The model in which, at frequencies much

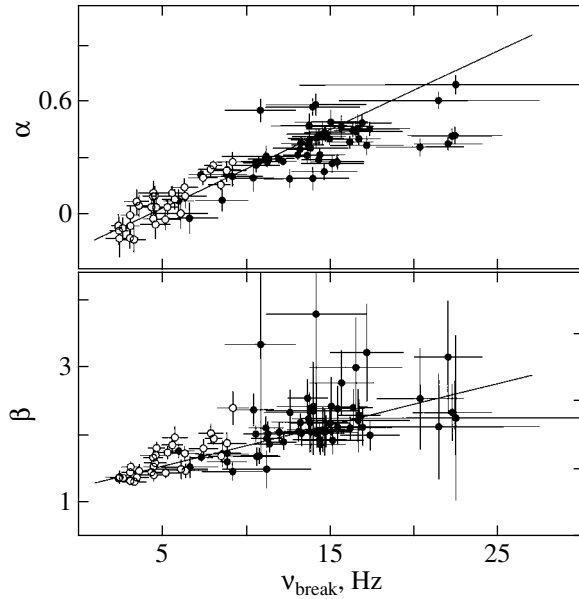


**Fig. 2.** Model indices  $\alpha$  and  $\beta$  versus break frequency. In the upper panel, the index corresponds to the fitting range at frequencies below the break; the lower panel shows an additional index that is introduced to fit a steepening of the spectrum above the break frequency. The best-fit parameters for those power-density spectra that, apart from the fundamental HBO harmonic, contain the second harmonic are indicated by open circles. The solid line represents a straight-line fit to the data. For the data shown in the upper and lower panels, the straight line was drawn by taking into account errors in the break frequency and in the index  $\beta$ , respectively.

higher ( $\nu/\nu_{\text{break}} \gg 1$ ) and much lower ( $\nu/\nu_{\text{break}} \ll 1$ ) than the break, each part of the spectrum could be fitted by its own power law and in which the transition between them was not jumpylike proved to be more suitable:

$$P = C \frac{\nu^{-\alpha}}{1 + (\nu/\nu_{\text{break}})^{\beta}}. \quad (1)$$

Thus,  $P \propto \nu^{-\alpha}$  at  $\nu/\nu_{\text{break}} \ll 1$  and  $P \propto \nu^{-\alpha-\beta}$  at  $\nu/\nu_{\text{break}} \gg 1$ .

The power-density spectra were fitted in the 0.1 – 128 Hz band by this model with the additional introduction of one or two Lorenz lines to allow for the peaks of QPOs and their harmonics. To take into account the PCA dead-time effect, which causes the total level to be shifted to the negative region [because of this effect, the Poissonian noise level subtracted from all spectra differs from 2.0 in Leahy units; see van der Klis (1995) for more details], we added a constant to the general model.

Figure 1 shows typical power-density spectra of Cyg X-2 for various measured break frequencies  $\nu_{\text{break}}$ . The upper spectrum was constructed from the observations on August 31, 1996 (7:04–8:00

UTC), and has the following best-fit parameters:  $\nu_{\text{break}} = 3.1 \pm 0.3$ ,  $\alpha = -0.13 \pm 0.04$ ,  $\beta = 1.45 \pm 0.03$ ,  $\nu_{\text{Lorenz}} = 20.17 \pm 0.05$ ,  $\nu_{2\text{Lorenz}} = 39.0 \pm 0.4$ ,  $\chi^2 = 236$  (217 d.o.f.). The lower power-density spectrum was obtained on March 24, 1996 (2:27–3:19 UTC), which was scaled by a factor of 0.01 and has the following parameters:  $\nu_{\text{break}} = 12 \pm 1$ ,  $\alpha = 0.30 \pm 0.03$ ,  $\beta = 2.0 \pm 0.2$ ,  $\nu_{\text{Lorenz}} = 45.0 \pm 0.7$ ,  $\chi^2 = 242$  (220 d.o.f.). In Fig. 1, we clearly see a difference between the two spectra. The best fits to each of the spectra (solid curves) are shown on the corresponding scale.

For all the selected data, we obtained satisfactory best-fit parameters. The break frequency turned out to positively correlate with the indices for the low-frequency and high-frequency parts of the power-density spectrum (0.3–128 Hz). In Fig. 2, the indices  $\alpha$  and  $\beta$  of model (1) are plotted against break frequency  $\nu_{\text{break}}$ , although in reality, the power-law spectral slope for  $\nu/\nu_{\text{break}} \gg 1$  tends to  $-\alpha - \beta$ , and the correlation is preserved. The open circles in Fig. 2 indicate the data whose power-density spectra exhibit two QPO peaks. The ratio of the peak frequencies is close to 2. As the break frequency increased, the significance of the HBO peaks reduced. The filled circles indicate the same data in which only the main QPO peak was detected and the second harmonic (probably) of the main peak was either undetectable or its significance was at a confidence level lower than  $3\sigma$ .

The data in Fig. 2 were fitted by straight lines. For each of the indices, we derived the following parameters:  $\alpha \approx -0.18 + 0.04\nu_{\text{break}}$ ;  $\beta \approx 1.23 + 0.06\nu_{\text{break}}$ .

## DISCUSSION

For the Z-type sources (to which Cyg X-2 belongs), the typical power-law index for the part of the spectrum above the break frequency lies within the range  $\sim 1.5$ – $2.0$  (van der Klis 1995). In papers on a time analysis of the low-frequency part of the power-density spectrum ( $< 100$  Hz) for Cyg X-2 (e.g., Kuulkers 1999), the variability of the source below the break frequency is assumed to be constant and is fitted by a constant. We see from Fig. 2 that the indices are equal to their assumed values for the spectra with break frequencies below  $\sim 10$  Hz. This range of break frequencies roughly corresponds to the position of the source on the horizontal branch of the Z track. For the other spectral states (NB and FB), the break frequency is difficult to determine because of the emergence of NBOs/FBOs at close frequencies or because of the absence of a visible break in the power-density spectrum (a power-law spectrum in the range 0.1–128 Hz).

Here, we analyzed all the available RXTE observations of Cyg X-2. The correlation between the power-law indices below and above the break frequency has been found for the first time. One might expect a similar correlation to be a common property of the Z-type sources.

#### ACKNOWLEDGMENTS

This study was supported by a French GDR PCHE grant, which made my visit to the Service d'Astrophysique possible. The work was supported in part by the Russian Foundation for Basic Research (project no. 00-15-96649). I used the RXTE archival data retrieved from the High Energy Astrophysics Science Archive Research Center (HEASARC), provided by the NASA/Goddard Space Flight Center. I wish to thank L. Titarchuk, B. Stone, Ph. Laurent, N. White, G. Swank, F. Newman, and J. Repaci for the opportunity to work with the RXTE archival data

on compact disks. I am also grateful to M. Revnivtsev for valuable remarks.

#### REFERENCES

1. H. Bradt, R. Rotschild, and J. Swank, *Astron. Astrophys., Suppl. Ser.* **97**, 335 (1993).
2. G. Hasinger and M. van der Klis, *Astron. Astrophys.* **225**, 79 (1989).
3. K. Jahoda, J. Swank, A. Giles, *et al.*, *Proc. SPIE* **2808**, 59 (1996).
4. E. Kuulkers, R. Wijnands, and M. van der Klis, *Mon. Not. R. Astron. Soc.* **308**, 485 (1999).
5. M. van der Klis, in *Timing Neutron Stars*, Ed. by H. Ögelman and E. P. J. van der Heuvel (Kluwer, Dordrecht, 1989), NATO ASI Ser., Vol. 360, p. 27.
6. M. van der Klis, in *Lives of the Neutron Stars*, Ed. by M. Alpar, Ü. Kiziloğlu, and J. van Paradijs (Kluwer, Dordrecht, 1995), NATO ASI Ser., Vol. 450, p. 301.

*Translated by V. Astakhov*

## A 59-Second Period in the Very High Energy Gamma-Ray Emission from the Geminga Pulsar

Yu. I. Neshpor\* and A. A. Stepanyan

*Crimean Astrophysical Observatory, p/o Nauchnyi, Crimea, 334413 Ukraine*

Received June 07, 2001

**Abstract**—An analysis of our observations of the Geminga object with the GT-48 ground-based gamma-ray telescope has shown that its very-high-energy gamma-ray flux is modulated with a 59-s period. The 59-s period and its time derivative previously inferred from satellite data have been confirmed. According to our data, the period was 61.94 s in 1997 at MSD = 50573. The statistical significance of this result is  $(1-4.5) \times 10^{-4}$ . © 2001 MAIK “Nauka/Interperiodica”.

Key words: *pulsars, ground-based gamma-ray astronomy, gamma-ray photons*

### INTRODUCTION

The Geminga object was discovered as a very-high-energy gamma-ray source from the SAS-2 satellite about thirty years ago (Kniffen *et al.* 1975). It had long been unidentifiable with a particular astrophysical object, because the accuracy of determining the coordinates with a spark chamber recording high-energy gamma rays, ( $> 100$  MeV), was low, ( $\sim 1^\circ$ ). This object was first identified with the X-ray source 1E 0630+178 discovered from the Einstein satellite (Bignami *et al.* 1983) and, subsequently, with an optical object (Bignami *et al.* 1987). Observations in other spectral ranges were facilitated by the discovery of a 0.237-s periodicity in the X-ray flux (Halpern and Holt 1992). It became clear that the Geminga object is a pulsar. Knowledge of the period made it possible to construct the light curves from SAS-2, COS-B, and EGRET high-energy gamma-ray flux measurements (Bignami and Caraveo 1992; Hermsen *et al.* 1992; Mattox *et al.* 1992; Bertsch *et al.* 1992). According to data from the Gamma-I telescope, the total pulsating 300–5000-MeV flux is  $(1.1 \pm 0.3) \times 10^{-6} \text{ cm}^{-2} \text{ s}^{-1}$  (Akimov *et al.* 1993). Pulsating emission with a 0.237-s period was also found in the very-high-energy gamma-ray data obtained with Cherenkov detectors (Bowden *et al.* 1993; Vishvanath *et al.* 1993). For a long time, no radio pulsations could be detected. The pulsating nature of the radio emission was established through a complex analysis of observations at the Astrospace Center of the Lebedev Physical Institute, Russian Academy of Sciences (Kuz'min and Lisovskii 1997;

Shitov and Pugachev 1997; Malofeev and Malov 1997).

It should be noted that an analysis of the SAS-2 gamma-ray data pointed to flux variability with a 59 s period (Thomson *et al.* 1977). Two years later, the COS-B satellite discovered a periodicity in the high-energy gamma-ray flux, but the period proved to be 0.2 s longer (Masnou *et al.* 1977). Subsequently, the Einstein (in 1979 and 1981) and Exosat (in 1983) satellites detected periodic X-ray flux variations. The period continuously increased and was  $> 60$  s in 1983. A variable (with a 59-s period) very-high-energy gamma-ray flux recorded with Cherenkov detectors was first noted by Zyskin and Mukanov (1983) based on the 1979 and 1981 observations and, subsequently, by Zyskin (1998) based on the 1983 observations. An analysis of the very-high-energy gamma-ray observations performed from December 1984 through February 1985 by an Indian team of researchers (Kaul *et al.* 1985) also revealed a 60.25-s periodicity. More recent observations of Geminga at the Whipple (Akerlof *et al.* 1993) and HEGRA (Aharonian *et al.* 1999) observatories yielded no positive results, probably because the source is variable. According to Bignami *et al.* (1984), an analysis of the HEAO 3 data confirmed the presence of a periodicity (with a 59-s period) in the gamma-ray emission with energy  $\sim 1$  MeV. However, this result was called into question by Buccheri *et al.* (1985). In 1996 and 1997, the Geminga gamma-ray source was observed with the GT-48 gamma-ray telescope at the Crimean Astrophysical Observatory. Below, we present the results of our analysis of the observational data.

\*E-mail: arnold@crao.crimea.na

## DESCRIPTION OF THE GT-48 GAMMA-RAY TELESCOPE

The GT-48 gamma-ray telescope records gamma rays with energy  $E > 10^{12}$  eV by detecting the Cherenkov flashes produced by the interaction of very-high-energy gamma rays with the atomic nuclei of the Earth's atmosphere. Since the area illuminated by a Cherenkov flash is large, tens of thousands of square meters, weak gamma-ray fluxes ( $\sim 10^{-11}$  cm $^{-2}$  s $^{-1}$ ) can be detected. The main obstacle to the detection and analysis of very-high-energy gamma-ray sources is a substantial background of cosmic rays, which produce Cherenkov flashes in the Earth's atmosphere; the latter are difficult to distinguish from the flashes produced by gamma rays. To cut off most of the flashes produced by the charged cosmic-ray component, new detectors, multielement cameras, are used. The GT-48 camera consists of 37 photomultipliers, which are used to obtain discretized images of Cherenkov flashes.

Up to 99% of background events (flashes) can be cut off by using differences in the parameters of flashes from gamma rays and from the charged cosmic-ray component (background).

The GT-48 gamma-ray telescope consists of two identical altazimuthal mountings (sections), northern and southern, separated by a distance of 20 m in the north-south direction and located at an altitude of 600 m above sea level. Apart from flashes in the atmosphere, Cherenkov detectors are known to record the passage of particles through the camera. Note that the parameters of the flashes produced by local charged particles and recorded by multichannel Cherenkov detectors are similar to those of the Cherenkov flashes in the atmosphere generated by very-high-energy gamma rays. Using dual detectors separated by a distance of 20 m or more and operating in the coincidence mode excludes the detection of charged-particle-triggered events almost completely (Chalenko *et al.* 1997).

The GT-48 gamma-ray telescope differs from other operational telescopes in that it simultaneously records Cherenkov flashes in the ultraviolet, in the wavelength range 200-300 nm. The total area of the GT-48 telescope mirrors is 54 m $^2$ . The facility is driven by a control system with a tracking accuracy of  $\pm 0.1^\circ$ . Observations can be carried out both in the mode of coincidences between the two sections and independently by each section. The flash detection time is recorded with an accuracy of 1 microsecond. A quartz oscillator with a relative accuracy of  $5 \times 10^{-9}$  during the observing period is used as the clock. The GT-48 telescope has been repeatedly described (Vladimirskii *et al.* 1994; Neshpor *et al.* 1998).

## OBSERVATIONAL DATA REDUCTION

The Geminga object ( $\alpha = 6^{\text{h}}33^{\text{m}}37^{\text{s}}$  and  $\delta = 17^\circ 46' 25''$ ) for 1996) was observed with two aligned sections in the coincidence mode with a time resolution of 100 ns using the object tracking method by comparing the observations of the gamma-ray source with those of the cosmic-ray background shifted in time by 40 min. The background observations preceded the source observations, and they were made at the same azimuthal and zenith angles. The excess in the number of recorded on-source events over that of off-source events was attributed to the presence of a gamma-ray flux. This difference turns out to be comparable to or even smaller than the statistical error, because the count rate was low (1 or 2 flashes in 1 s), while the number of flashes from gamma rays was several hundred times smaller than that of background flashes. One must exclude the largest possible number of flashes that are definitely produced by background events. To this end, we used the difference between the parameters of the flashes produced by gamma rays and those of the flashes produced by the cosmic-ray background.

Five and eight 35-min-long observing sessions were carried out in 1996 and 1997, respectively; the total duration of the observations was 175 min in 1996 and 280 min in 1997.

We subjected our data to an initial reduction, which was required to properly calculate the first and second moments of the brightness distribution. To this end, we excluded the flashes whose brightness distribution peaked in the outer ring of photomultipliers and the flashes for which the signal amplitude was larger than the maximum possible value accessible to the analog-to-digital converter at least in one photomultiplier. The derived brightness distribution made it possible to determine the parameters of the Cherenkov flash: effective length  $A$ , width  $B$ , and  $X_c, Y_c$  coordinates of the brightness centroid. Through this initial data reduction, 3867 on-source events and 3826 off-source events were left from the 1996 data; and 5725 and 5690 events, respectively, were left from the 1997 data for the subsequent analysis.

An analysis of these data led us to conclude (Neshpor *et al.* 2001) that there was a flux of gamma rays with energy  $> 1$  TeV pulsating with a 0.237-s period. Monte Carlo simulations yielded a flux of  $(24 \pm 8) \times 10^{-12}$  photons cm $^{-2}$  s $^{-1}$ . Based on these data, we show below that the gamma-ray flux from Geminga varies with a period of  $\sim 60$  s.

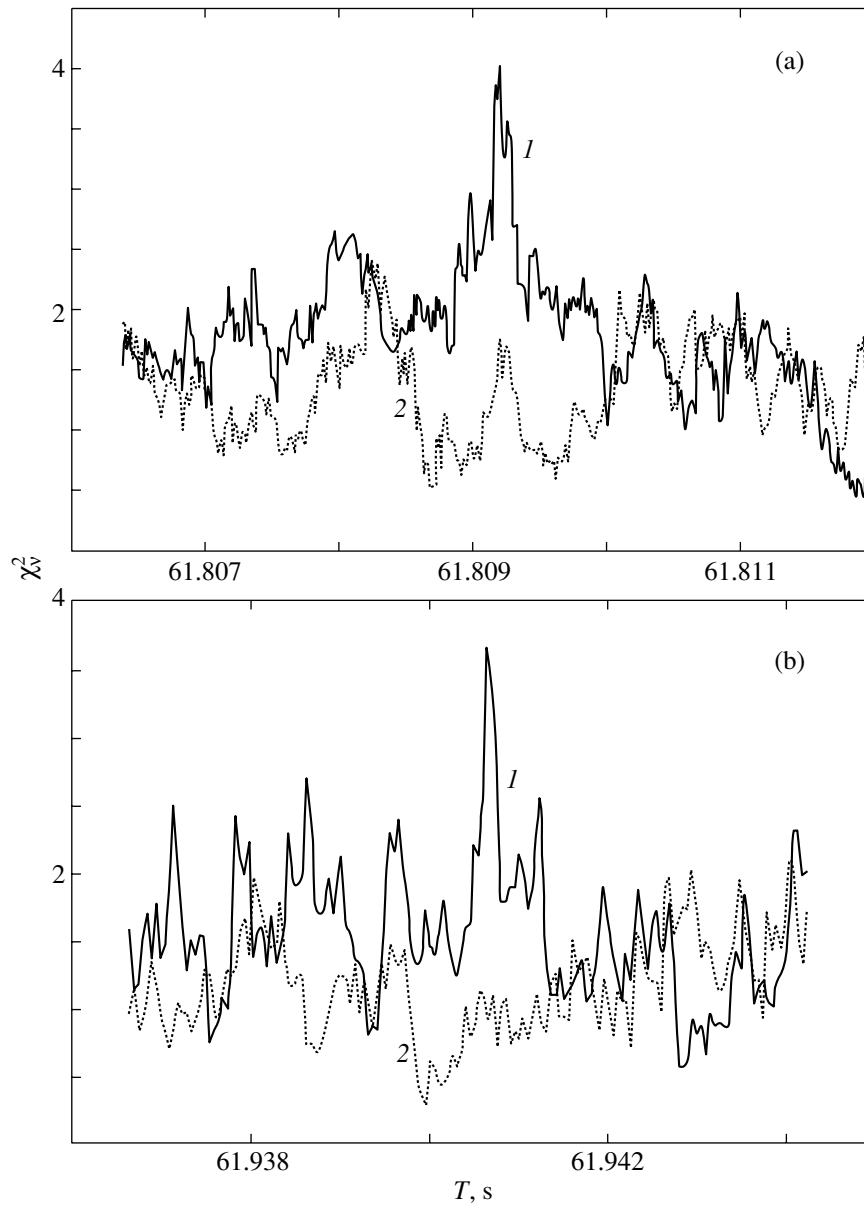


**Fig. 1.** Fragments of the period dependence of  $\chi^2_\nu$ , for  $\nu = 10$ : (a) as constructed from the 1996 data; (b) as constructed from the 1997 data: (1) on-source observations, (2) off-source observations.

### PULSATING GAMMA-RAY EMISSION

We analyzed the observations described above in an effort to find the pulsating component with a 59-s period in the very-high-energy gamma-ray emission. To limit the range of trial periods, we extrapolated the Einstein X-ray measurements in 1979 and 1981 and the EXOSAT X-ray measurements in 1983 (Bignami *et al.* 1984) to 1996 and 1997. A linear least-squares fit yielded the following expression for the period:

$$T(t) = (59.4863 \pm 0.0599) \\ + (0.000401314 \pm 0.00003868)t,$$

where  $t = t(i) - t(0)$ ,  $t(0)$  is the mean detection time on the X-ray satellites, and  $t(i)$  is the current time. The time  $t$  is in Julian days, and the period  $T$  is in seconds. Given the errors, the ranges of expected periods are (61.698–62.302) s in 1996 and (61.826–62.457) s in 1997. We analyzed our data within these ranges of periods. We took into account the time derivative given by

$$\frac{dT}{dt} = \frac{(T(t) - T(0))}{(t(i) - t(0))}.$$

The analysis was performed by the epoch-folding technique for the following selected gamma-ray-like

## Luminosity

Radio $\log L_p$	Optical $\log L_{opt}$	X-ray $\log L_X$	Gamma-ray		Total losses energy $\log \dot{E}$
			$\log L_{h.e.}$	$\log L_{v.h.e.}$	
26.5	27.7	30.6	33.8	32.7	34.5
[1]	[2]	[3]	[4]	[5]	

[1] Kuzmin and Losovskii 1999; [2] Bignami *et al.* 1996; [3] Halpern and Holt 1992; [4] Masnou *et al.* 1981; [5] Neshpor *et al.* 2001.

events: 176 and 103 on- and off-source events in 1996 and 109 and 86 on- and off-source events, respectively, in 1997. For each event, we determined the phase from the specified period and from the corresponding time derivative. The trial period was

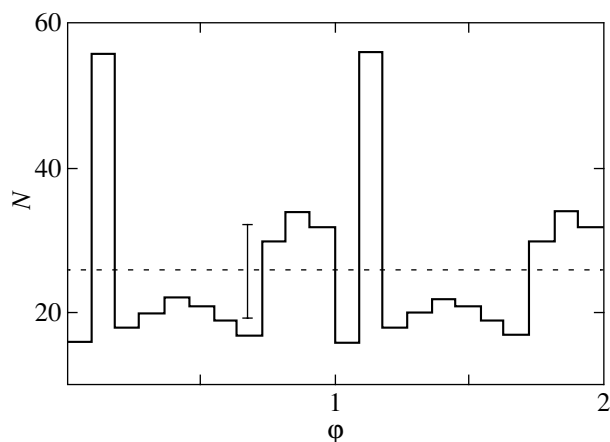


Fig. 2. The total phase histogram as constructed from the 1996–1997 data:  $\varphi$  is the phase in fractions of the period,  $N$  is the number of gamma-ray-like events.

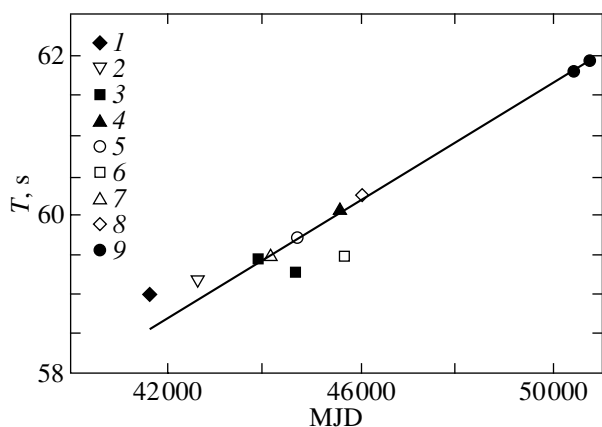


Fig. 3. The time dependence of period as derived from published data: 1—Thomson *et al.* (1977), 2—Masnou *et al.* (1977), 3—Zyskin and Mukanov (1983), 4—Bignami *et al.* (1984), 5—Bignami *et al.* (1984), 6—Zyskin (1988), 7—Bignami *et al.* (1984), 8—Kaul *et al.* (1985), 9—this paper.

varied for the measurements at independence steps of 0.00078 and 0.00056 s in the 1996 and 1997 data, respectively). We broke down the entire period into eleven phase bins and constructed the phase distribution of events (light curve). Figures 1a and 1b show fragments of the dependence of  $\chi^2$  on trial period for the 1996 and 1997 data, respectively. The  $\chi^2$  value peaks at  $T = 61.80921(78)$  s for MJD = 50401 and at  $T = 61.94066(54)$  s for MJD = 50753, as inferred from the 1996 and 1997 data, respectively [the independence step (the last two digits) is given in parentheses]. Figure 1 also shows  $\chi^2$  for the off-source data. We see that in the off-source data, the  $\chi^2$  values show no appreciable peculiarity. The probabilities of a random on-source distribution are, respectively,  $3.3 \times 10^{-6}$  and  $7.5 \times 10^{-6}$ . Given the number of independent trials, these probabilities are  $2.5 \times 10^{-3}$  and  $8.4 \times 10^{-3}$ , respectively. The periods for maximum  $\chi^2$  are obtained for virtually the same time derivative ( $4.3222 \times 10^{-9}$  s s $^{-1}$ ), which allows us to combine the light curves for 1996 and 1997 after applying a small (within the independence step) correction to the periods in different years. As a result, we obtained refined periods: 61.80922(11) and 61.94067(11) s for 1996 and 1997, respectively. The period derivative remains the same. Figure 2 shows the gamma-ray light curve constructed from the combined data of 1996 and 1997. Given the number of trials, the probability of a random phase distribution is  $4.5 \times 10^{-4}$ . The flux of the periodicity at the peak of the light curve is  $(9 \pm 3) \times 10^{-11}$  photons cm $^{-2}$  s $^{-1}$ .

Neshpor *et al.* (2001) found the mean gamma-ray flux with energy  $> 1$  TeV to be  $(2.4 \pm 0.9) \times 10^{-11}$  photons cm $^{-2}$  s $^{-1}$ , implying that 1/3 of the total flux is emitted at the peak of the light curve. The light curve (Fig. 2) suggests that the phase curve has yet another peak, but its confidence level is rather low (0.995).

## CONCLUSIONS

The very-high-energy ( $> 1$  TeV) gamma-ray observations of the Geminga pulsar have allowed the 59-s period and its time derivative to be accurately

determined. Figure 3 shows the published values of the 59-s period for the Geminga pulsar and the straight line drawn with our period derivative. We see that most of the data lie near this straight line. The table gives published data on the pulsar luminosity ( $L$ ,  $\text{erg s}^{-1}$ ) in various spectral ranges under the assumption of their isotropicity. The distance to Geminga was taken to be 160 pc (Bignami *et al.* 1996). These authors also gave the magnitude of the object and the total losses of rotational energy by the neutron star. Note that the intensity of the gamma-ray emission accounts for 20% of the total energy losses at high energies ( $> 100$  MeV) and for a mere 1.5%, i.e., an order of magnitude lower, at very high energies. The origin of the 59-s period is not yet clear. The uncertainty in the results of analyses of the observational data may have not stimulated theoretical research in this regard. The results of our analysis of very-high-energy gamma-ray observations will increase the confidence in the reality of the 59-s period.

#### ACKNOWLEDGMENTS

We wish to thank V.P. Fomin and O.R. Kalekin for helpful discussions and Z.N. Skiruta and S.G. Kochetkov for the assistance in preparing the manuscript for publication.

#### REFERENCES

1. F. A. Aharonian, A. G. Aherperjanian, and J. A. Barrio, *Astron. Astrophys.* **346**, 913 (1999).
2. C. W. Akerlof, A. C. Breslin, M. F. Cawley, *et al.*, *Astron. Astrophys.* **274**, L17 (1993).
3. V. V. Akimov, V. G. Afanas'ev, I. D. Blokhintsev, *et al.*, *Pis'ma Astron. Zh.* **19**, 579 (1993) [*Astron. Lett.* **19**, 229 (1993)].
4. D. L. Bertsch, K. T. S. Brazier, C. E. Fichtel, *et al.*, *Nature* **357**, 306 (1992).
5. G. F. Bignami and P. A. Caraveo, *Nature* **357**, 287 (1992).
6. G. F. Bignami, P. A. Caraveo, and R. C. Lamb, *Astrophys. J. Lett.* **272**, L9 (1983).
7. G. F. Bignami, P. A. Caraveo, and J. A. Paul, *Nature* **310**, 464 (1984).
8. G. F. Bignami, P. A. Caraveo, J. A. Paul, *et al.*, *Astrophys. J.* **319**, 358 (1987).
9. G. F. Bignami, P. A. Caraveo, R. Mignami, *et al.*, *Astrophys. J. Lett.* **456**, L111 (1996).
10. C. C. G. Bowden, S. M. Bradbury, P. M. Chadwick, *et al.*, *J. Phys. G* **19**, L29 (1993).
11. R. Buccheri, N. D'Amico, W. Hermsen, and B. Sacco, *Nature* **316**, 131 (1985).
12. N. N. Chalenko, O. R. Kalekin, Yu. I. Neshpor, and A. A. Stepanyan, *J. Astrophys. Astron.* **18**, 151 (1997).
13. J. P. Halpern and S. S. Holt, *Nature* **357**, 222 (1992).
14. W. Hermsen, B. N. Swanenbyrg, R. Buccheri, *et al.*, *IAU Circ.*, No. 5541 (1992).
15. R. K. Kaul, H. S. Rawat, V. K. Sanecha, *et al.*, in *Proceedings of the 19th International Cosmic Ray Conference, La Jolla, 1985*, Vol. 1, p. 165.
16. D. A. Kniffen, G. F. Bignami, C. E. Fichtel, *et al.*, in *Proceedings of the 14th International Cosmic Ray Conference, München, 1975*, Vol. 1, p. 100.
17. A. D. Kuz'min and B. Ya. Losovskii, *Pis'ma Astron. Zh.* **23**, 323 (1997) [*Astron. Lett.* **23**, 283 (1997)].
18. A. D. Kuz'min and B. Ya. Losovskii, *Pis'ma Astron. Zh.* **25**, 108 (1999) [*Astron. Lett.* **25**, 80 (1999)].
19. V. M. Malofeev and O. J. Malov, *Nature* **389**, 697 (1997).
20. J. L. Masnou, K. Bennett, G. F. Bignami, *et al.*, in *Proceedings of the 12th ESLAB Symposium, Frascati, 1977*, p. 33.
21. J. L. Masnou, K. Bennett, G. F. Bignami, *et al.*, in *Proceedings of the 17th International Cosmic Ray Conference, Paris, 1981*, Vol. 1, p. 177.
22. J. R. Mattox, D. L. Bertsch, C. E. Fichtel, *et al.*, *Astrophys. J. Lett.* **401**, L23 (1992).
23. Yu. I. Neshpor, A. A. Stepanyan, O. R. Kalekin, *et al.*, *Pis'ma Astron. Zh.* **24**, 167 (1998) [*Astron. Lett.* **24**, 134 (1998)].
24. Yu. I. Neshpor, A. A. Stepanyan, Yu. L. Zyskin, *et al.*, *Pis'ma Astron. Zh.* **27**, 266 (2001) [*Astron. Lett.* **27**, 228 (2001)].
25. Yu. P. Shitov and V. D. Pugachev, *New Astron.* **3**, 101 (1998).
26. D. J. Thompson, C. E. Fichtel, and R. C. Hartman, *Astrophys. J.* **213**, 252 (1977).
27. P. R. Vishwanath, G. P. Satyanarayana, P. V. Ramanamurty, *et al.*, *Astron. Astrophys.* **267**, L5 (1993).
28. B. M. Vladimirskii, Yu. L. Zyskin, A. P. Kornienko, *et al.*, *Izv. Krym. Astrofiz. Obs.* **91**, 74 (1995).
29. Yu. L. Zyskin, *Space Sci. Rev.* **49**, 49 (1988).
30. Yu. L. Zyskin and D. B. Mukanov, *Pis'ma Astron. Zh.* **9**, 219 (1983) [*Sov. Astron. Lett.* **9**, 117 (1983)].

*Translated by A. Dambis*

# Nodal and Periastron Precession of Inclined Orbits in the Field of a Rotating Black Hole

N. R. Sibgatullin<sup>1,2,\*</sup>

<sup>1</sup>Moscow State University, Vorob'evy gory, Moscow, 119899 Russia

<sup>2</sup>Max-Planck-Institut für Astrophysik, Karl Schwarzschild Strasse 1, 86740 Garching bei München, Germany

Received June 28, 2001

**Abstract**—The inclination of low-eccentricity orbits is shown to significantly affect orbital parameters, in particular, the Keplerian, nodal precession, and periastron rotation frequencies, which are interpreted in terms of observable quantities. For the nodal precession and periastron rotation frequencies of low-eccentricity orbits in a Kerr field, we derive a Taylor expansion in terms of the Kerr parameter at arbitrary orbital inclinations to the black-hole spin axis and at arbitrary radial coordinates. The particle radius, energy, and angular momentum in the marginally stable circular orbits are calculated as functions of the Kerr parameter  $j$  and parameter  $s$  in the form of Taylor expansions in terms of  $j$  to within  $O[j^6]$ . By analyzing our numerical results, we give compact approximation formulas for the nodal precession frequency of the marginally stable circular orbits at various  $s$  in the entire range of the Kerr parameter.  
© 2001 MAIK “Nauka/Interperiodica”.

Key words: *black holes, precession, disk accretion*

## INTRODUCTION

The X-ray quasi-periodic oscillations (QPOs) discovered in low-mass X-ray binaries (LMXBs) commonly show a variety of modes. In particular, there are horizontal-branch oscillations at low frequencies  $\nu_{\text{HBO}}$  1–100 Hz and two peaks at frequencies  $\nu_1$  and  $\nu_2$  ( $\sim 1$  kHz) in the power spectrum (van der Klis 2000). In many  $Z$ -type sources, as well as in several atoll sources, the frequencies  $\nu_{\text{HBO}}$  exhibit an almost quadratic dependence on  $\nu_2$  (Stella and Vietri 1998; Psaltis *et al.* 1999). For several sources (e.g., for Sco X-1, 4U 1608–52, 4U 1702–43, 4U 1735–44, and XTE J2123–058), the frequency difference  $\nu_2 - \nu_1 \equiv \Delta\nu$  decreases with increasing  $\nu_2$ . At the same time, for many  $Z$ -type (GX 5–1, GX 17+2, Cyg X-2, GX 340+0, GX 349+2) and atoll (4U 0614+09, 4U 1636–52, 4U 1705–44, and Aql X-1) sources, the difference  $\Delta\nu$  is constant, which allows it to be associated with the stellar rotation frequency (van der Klis 2000). The frequency  $\nu_2$  is currently identified with the Keplerian rotation frequency of clumps of matter near a compact object ( $\nu_2 \equiv \nu_{\text{K}}$ ) in almost all interpretations.

Cui *et al.* (1998) pointed out that the nodal precession of circular orbits<sup>1</sup> slightly inclined to the equatorial plane of a black hole could be of importance

in interpreting the stable QPOs: for several black-hole candidates and microquasars, they found the predicted frequencies of nodal precession agree (if the Kerr parameter is chosen in the range 0.37 – 0.9) with the observed QPO frequencies.

Stella and Vietri (1998) justified the formula for the nodal precession frequency  $\nu_{\text{nod}}$  of orbits slightly inclined to the equatorial plane and identified its even harmonics with the frequency  $\nu_{\text{HBO}}$ . The frequency  $\nu_1$  was associated with the periastron rotation frequency  $\nu_{\text{per}} = \nu_{\text{K}} - \nu_r$  of a low-eccentricity orbit (a general-relativity effect). They showed that the theoretical dependence  $\nu_r(\nu_{\phi})$  for an appropriately chosen mass of the object in the range  $1.8 - 2.2M_{\odot}$  was in good agreement with the experimental points in the  $(\nu_2, \Delta\nu)$  plane for various sources with evolving frequencies. In the Kerr solution, the frequency  $\nu_r$  becomes zero in the marginally stable orbit. Therefore, when a radiating clump of matter passes from one Keplerian orbit to another<sup>2</sup> by increasing its rotation frequency, the frequency difference between the peaks  $\Delta\nu = \nu_r$  decreases and even approaches zero in the marginally stable orbit. This tendency was observed for some of the sources (see above).

Morsink and Stella (1999), Stella and Vietri (1998), and Psaltis *et al.* (1999) showed that the theoretical dependences  $\nu_{\text{nod}}(\nu_{\text{K}})$  agreed with the

\*E-mail: sibgat@mech.math.msu.su

<sup>1</sup>Lense–Thirring (1918) effect.

<sup>2</sup>Through turbulent viscosity and radiative deceleration.

measured source frequencies in the  $\nu_2, \nu_{\text{HBO}}$  plane if  $\nu_{\text{HBO}}$  was identified with an appropriate even harmonic of the nodal frequency.

The proper rotation of the source (a neutron star or a black hole) remains a free parameter, and it can be chosen by using the stable frequency observed in LMXBs in the X-ray band during outbursts.

Another free parameter is the orbital inclination  $s$  to the equatorial plane, of a neutron star or a black hole, which significantly affects the observed nodal precession, periastron rotation, and Keplerian frequencies near the marginally stable orbit. Below, we give an example based on our results. If the mass of a black hole or a neutron star is  $M$ , then for the Keplerian frequency in the marginally stable orbit  $\nu_\phi = 1.2 (2.2M_\odot/M)$  kHz, the frequency of nodal precession  $\nu_{\text{nod}}$  is, respectively, 123  $(2.2M_\odot/M)$  Hz at  $s = 0$ ; 93.6  $(2.2M_\odot/M)$  Hz at  $s = 10^\circ$ ; 65.3  $(2.2M_\odot/M)$  Hz at  $s = 30^\circ$ ; 52.6  $(2.2M_\odot/M)$  Hz at  $s = 45^\circ$ ; 45.5  $(2.2M_\odot/M)$  Hz at  $s = 60^\circ$ ; 41.18  $(2.2M_\odot/M)$  Hz at  $s = 80^\circ$ ; and 41.11  $(2.2M_\odot/M)$  Hz at  $s = 90^\circ$ . The nodal precession frequency changes by almost a factor of 3 as the inclination changes from  $\pi/2$  to 0! Thus, by simultaneously measuring three quantities,  $M$ ,  $\nu_{\text{HBO}}$ , and  $\nu_2$ , we can determine the inclination of the marginally stable orbit to the spin axis!

In general, the tilt of an accretion disk to the equatorial plane of a compact object can be finite. The Bardeen–Petterson (1975) hypothesis of the accretion-disk transition into the equatorial plane breaks down even when the radiative forces that twist the inner edge of the disk are taken into account. Pringle (1996) showed that a flat disk was unstable to disturbances in the presence of a central radiation source.

Below, we derive formulas for the Keplerian, nodal precession, and periastron rotation frequencies of low-eccentricity orbits at an arbitrary (finite) orbital inclination to the equatorial plane in the form of Taylor expansions in terms of the Kerr parameter. In contrast to previous studies, in which calculations were performed for selected values of the constant  $Q$  [with an unclear physical meaning, as was noted by de Felice (1980), and coinciding with the square of the total angular momentum only in the weak-field approximation  $Q$ ], we consistently use the smallest latitudinal angle  $\theta_- = s$  reached on a bounded trajectory<sup>3</sup> as a trajectory parameter. At  $s = \pi/2$ , the derived formulas (51) transform into Taylor expansions of the formulas by Okazaki *et al.* (1987). An analysis of our numerical results has

<sup>3</sup>Below,  $s$  is called the inclination angle between the angular velocity vector of a compact object and the orbital surface for short.

yielded compact approximation formulas for the nodal precession frequency of the marginally stable circular orbits in the entire range of the Kerr parameter for several finite orbital inclinations.

In contrast to rotating black holes, an intrinsic quadrupole component appears in the external fields of rapidly rotating neutron stars (NSs). For NSs with a stiff equation of state, this component can be several times larger than the Kerr quadrupole moment. The effect of a non-Kerr NS field induced by rapid NS rotation on the parameters of the marginally stable orbit and energy release in the equatorial boundary layer was analyzed by Sibgatullin and Sunyaev (1998, 2000a, 2000b) using an exact solution for a rotating configuration with a quadrupole moment (Manko *et al.* 1994) [approximate approaches with multipole expansions of the metric coefficients at large radii were developed by Laarakkers and Poisson (1998) and Shibata and Sasaki (1998)]. Our results refer to nonequatorial, nearly circular orbits in the fields of black holes and NSs with a soft equation of state at a moderate rotation frequency (up to 400 Hz). Markovic (2000) considered finite-eccentricity orbits in a Kerr field and in the post-Newtonian approximation for a field with a finite quadrupole moment. The precession of orbits slightly inclined to the equatorial plane in the fields of rotating NSs was numerically calculated by Morsink and Stella (1999) and Stella *et al.* (1999).

## GEODESICS IN THE KERR SOLUTION

It is well known that the equations of geodesics in Riemannian spaces can be written in Hamiltonian form. The corresponding Hamilton–Jacobi equation is

$$Q \equiv (g^{i,j} S_{,i} S_{,j} + 1)/2 = 0, \quad S_{,i} \equiv \frac{\partial S}{\partial x^i}, \quad (1)$$

$$i, j, \dots = 0, 1, 2, 3.$$

The generalized momenta  $p_i = S_{,i}$  are related to the 4-velocity components by the Hamilton equations

$$\frac{dx^j}{d\tau} = \frac{\partial Q}{\partial p_j} = g^{jk} p_k, \quad \frac{dp_j}{d\tau} = -\frac{\partial Q}{\partial x^j} = -\frac{\partial g^{kl}}{\partial x^j} p_k p_l. \quad (2)$$

For the Kerr solution in Boyer–Lindquist coordinates, the contravariant metric components are

$$g^{00} = -\frac{(r^2 + a^2)^2 - \Delta a^2 \sin^2 \theta}{\rho^2 c^2 \Delta}, \quad (3)$$

$$g^{\phi\phi} = \frac{(1 - 2rGM/c^2 \rho^2)}{\Delta \sin \theta},$$

$$g^{0\phi} = \frac{-2ar}{\rho^2 \Delta}, \quad g^{rr} = \frac{\Delta}{\rho^2}, \quad g^{\theta\theta} = \frac{1}{\rho^2}.$$

$$\Delta \equiv r^2 + a^2 - 2rGM/c^2; \quad \rho^2 \equiv r^2 + a^2 \cos^2 \theta.$$

The constant  $a$  is related to the angular momentum of a rotating black hole described by the Kerr solution by the equality  $J = Mac = GM^2 j/c$ , where  $j$  is the dimensionless Kerr parameter. Because of axial symmetry and stationarity, the Hamilton–Jacobi equation (1) for the Kerr metric has two cyclic coordinates,  $t$  and  $\phi$ ; therefore, Eq. (1) with the first integrals  $p_t = -E = \text{const}$  and  $p_\phi = L = \text{const}$  for the Kerr metric can be written as

$$(1 - E^2)((r^2 + a^2)^2 - \Delta a^2 \sin^2 \theta) + 4arLEGM/c^3 + (\rho^2 - 2GMr/c^2) \times L^2/(c \sin \theta)^2 + \Delta^2 S_{,r}^2 + \Delta S_{,\theta}^2 = 2r(r^2 + a^2)GM/c^2. \quad (4)$$

The existence of the complete integral of the Hamilton–Jacobi equation established by Carter (1968) is less obvious:

$$S = -Etc^2 + L\phi + \int \sqrt{\Theta(\theta)}d\theta + \int \sqrt{R(r)}\frac{dr}{\Delta},$$

$$\Theta(\theta) \equiv Q - \cos^2 \theta(a^2 c^2(1 - E^2) + L^2/(\sin \theta)^2), \quad (5)$$

$$R(r) \equiv (cE(r^2 + a^2) - La)^2 - \Delta(r^2 + (L - aEc)^2 + Q). \quad (6)$$

Instead of the constant  $Q$ , we introduce a constant  $s < \pi/2$ , which has the meaning of the minimum angle  $\theta$  (turning point) reached on the bounded trajectory in question [in the notation of Wilkins (1972), the constant  $s \equiv \theta_-$ ; see also Shakura (1987)]. According to (5), the constant  $Q$  can be expressed in terms of  $s$ :

$$Q = \cos^2 s(a^2 c^2(1 - E^2) + L^2/(\sin s)^2). \quad (7)$$

In that case, the angle  $\theta$  on a bounded trajectory varies over the range  $s < \theta < \pi - s$ .

For stable trajectories on the  $r = \text{const}$  surfaces, the following conditions must be satisfied:

$$R(r) = 0, \quad dR(r)/dr = 0 \quad (8)$$

(Bardeen *et al.* 1972; Wilkins 1972).

### THE NEWTONIAN ANALOG OF THE KERR SOLUTION

#### *The Newtonian Analog of the Supercritical Kerr Solution and its Potentials*

In the Newtonian limit,  $E^2 \approx 1 + 2H/c^2$  and  $\Delta \approx r^2 + a^2$ . Substituting these expressions in Eq. (4) yields an approximate Hamilton–Jacobi equation:

$$2H = \frac{L^2}{(r^2 + a^2) \sin^2 \theta} + \frac{r^2 + a^2}{r^2 + a^2 \cos^2 \theta} S_{,r}^2 + \frac{1}{r^2 + a^2 \cos^2 \theta} S_{,\theta}^2 + \frac{4arLGM/c}{(r^2 + a^2)(r^2 + a^2 \cos^2 \theta)} \quad (9)$$

$$- \frac{2GMr}{r^2 + a^2 \cos^2 \theta} + \frac{4(GMra \sin \theta)^2}{(r^2 + a^2 \cos^2 \theta)c^2(r^2 + a^2)}.$$

Note that Eq. (8) describes the trajectories of test particles in the field of a flat disk with the radius  $a$  in special curvilinear coordinates  $r, \theta, \phi$ , which are related to the Cartesian coordinates  $x, y, z$  by

$$r = \frac{1}{2}(\sqrt{x^2 + y^2 + (z - ia)^2} + \sqrt{x^2 + y^2 + (z + ia)^2}), \quad (10)$$

$$a \sin \theta = \frac{1}{2i}(\sqrt{x^2 + y^2 + (z + ia)^2} - \sqrt{x^2 + y^2 + (z - ia)^2}), \quad (11)$$

$$\phi = \arctan y/x.$$

When passing from Cartesian coordinates  $x, y, z$  to orthogonal curvilinear coordinates  $r, \theta, \phi$  using formulas (10) and (11), the nonzero metric tensor components are expressed in terms of the curvilinear coordinates as

$$g_{rr} = \frac{r^2 + a^2 \cos^2 \theta}{r^2 + a^2}, \quad g_{\theta\theta} = r^2 + a^2 \cos^2 \theta, \quad (12)$$

$$g_{\phi\phi} = (r^2 + a^2) \sin^2 \theta.$$

Hamiltonian (9) contains the contravariant metric tensor components (12), and it can be written in the Cartesian coordinates as

$$H = \frac{(p + \mathbf{A}/c)^2}{2} - \Phi.$$

The corresponding Hamilton equations are

$$\frac{dp_k}{dt} = \Phi_{,k} - (p + \mathbf{A}/c) \frac{\partial \mathbf{A}/c}{\partial x^k}, \quad \frac{dx^k}{dt} = p_k + \mathbf{A}_k/c. \quad (13)$$

Eqs. (13) can be rewritten as the equations of motion in a gravitomagnetic field in the quasi-Newtonian approximation

$$\frac{dv}{dt} = \nabla \Phi + \text{curl} \mathbf{A} \times v/c, \quad (14)$$

where the Newtonian potential  $\Phi$  and the gravitomagnetic vector potential  $\mathbf{A}$  in a vacuum satisfy the Laplace equation. The equations of relative motion in a rotating coordinate system can be derived from Eqs. (14) if  $\boldsymbol{\Omega} \times \mathbf{R}$ ,  $\mathbf{R} = (x, y, z)$ , is substituted for  $\mathbf{A}$ . In that case,  $\text{curl} \mathbf{A}/c = -2\boldsymbol{\Omega}$  and the second term on the right-hand side of (13) represents the Coriolis force.

For a flat Kerr disk, the Newtonian potential  $\Phi$  is (Israel 1970; Zaripov *et al.* 1995)

$$\Phi = \frac{GM}{2\sqrt{x^2 + y^2 + (z + ia)^2}} + \frac{GM}{2\sqrt{x^2 + y^2 + (z - ia)^2}}. \quad (15)$$

The vector  $\mathbf{A}$  consists of the components  $-g_{0\alpha}/g_{00}$ ,  $\alpha = 1, 2, 3$  (Landau and Lifshitz 1980). In the Newtonian limit in a vacuum, the vector of the gravitomagnetic field  $\Psi$  can be introduced instead of the vector potential  $\mathbf{A}$ :

$$\text{curl}\mathbf{A} = 2\nabla\Psi. \quad (16)$$

The scalar  $\Psi$  in an axisymmetric case matches the imaginary part of the Ernst complex potential. For the special case of a Kerr disk, the scalar  $\Psi$  is (Zaripov *et al.* 1995):

$$\Psi = \frac{GM}{2i\sqrt{x^2 + y^2 + (z - ia)^2}} - \frac{GM}{2i\sqrt{x^2 + y^2 + (z + ia)^2}}. \quad (17)$$

Clearly, expressions (15) and (17) for  $\Phi$  and  $\Psi$  satisfy the Laplace equation.

As follows from definition (10), the  $r = \text{const}$  surface is neither a sphere nor an ellipsoid.

#### *The Precession of Circular Keplerian Orbits in the Field of a Gravitating Rotating Mass*

For the Newtonian analog of a supercritical Kerr disk,  $a > GM/c^2$ . However, since  $a < GM/c^2$  for black holes, in this subsection, we discard terms of the order of  $a^2$  in expressions (15) and (17) for  $\Phi$  and  $\Psi$  lest the order of accuracy of the model be exceeded. In that case,  $\Phi \approx GM/r$ ,  $\Psi \approx -azGM/r^3$ .

Let us introduce a coordinate system with the origin at the gravitating mass with the  $z$  axis directed along the spin axis. The equations of motion for free particles in this coordinate system are

$$\frac{du}{dt} = -\frac{GMx}{r^3} + \left(6a(yw - zv)\frac{z}{r^5} + 2v\frac{a}{r^3}\right)\frac{GM}{c}, \quad (18)$$

$$\frac{dv}{dt} = -\frac{GM y}{r^3} + \left(6a(zu - xw)\frac{z}{r^5} - 2u\frac{a}{r^3}\right)\frac{GM}{c}, \quad (19)$$

$$\frac{dw}{dt} = -\frac{GMz}{r^3} + \left(6a(xv - yu)\frac{z}{r^5}\right)\frac{GM}{c}. \quad (20)$$

In our approximation, the complete integral of the Hamilton–Jacobi equation is [cf. formulas (5)–(6)]

$$S = -Ht + L\phi + \int \sqrt{\Theta(\theta)}d\theta + \int \sqrt{2R(r)}dr, \quad (21)$$

$$\Theta(\theta) \equiv L^2 \cot^2 s - L^2 \cot^2 \theta.$$

$$R(r) \equiv H + \frac{GM}{r} - \frac{L^2}{2r^2 \sin^2 s} - 2\frac{LaGM}{r^3 c}. \quad (22)$$

In formulas (21) and (22), we chose the turning point for the angle  $\theta$  as a constant: according

to (20),  $\theta$  varies over the range  $s < \theta < \pi - s$ , with  $0 < s < \pi/2$ .

For stable circular trajectories, the equalities  $R(r) = 0$  and  $dR(r)/dr = 0$  must be satisfied. Substituting expression (21) for a fixed radius  $r$  in these equations yields the corresponding energy  $H$  and angular momentum  $L$ :

$$H \approx -\frac{GM}{2r} - a\sqrt{(GMr)^3}\frac{\sin s}{cr^4}, \quad (23)$$

$$L \approx \sin s\sqrt{GMR} - 3aGM\frac{\sin^2 s}{cr}.$$

Consider the precession of circular orbits. From the Hamilton equations  $\dot{\theta} = \partial H/\partial p_\theta$  and  $\dot{\phi} = \partial H/\partial L$ , we have

$$\frac{d\theta}{dt} = \frac{L}{r^2}\sqrt{\cot^2 s - \cot^2 \theta}, \quad (24)$$

$$\frac{d\phi}{dt} = \frac{L}{r^2 \sin^2 \theta} + \frac{2aGM}{r^3 c}. \quad (25)$$

Integrating Eq. (24) yields

$$\begin{aligned} \phi - \phi_0 &= \int \frac{Ldt}{r^2 \sin^2 \theta} + \frac{2aGMt}{r^3 c} \\ &= \int \frac{d\theta}{\sin^2 \theta \sqrt{\cot^2 s - \cot^2 \theta}} + \frac{2aGMt}{r^3 c} \\ &= \arcsin\left(\frac{\cot \theta}{\cot s}\right) + \frac{2aGMt}{r^3 c}. \end{aligned} \quad (26)$$

When changing the variable in formula (26), we used Eq. (24).

Consider the case where all particles at  $t = 0$  were in the  $\sin \phi \sin \theta = \cos \theta \cot s$  plane or, introducing Cartesian coordinates, in the  $y = z \cot s$  plane. According to equality (26), the particles will lie on the  $y \cos(2aGMt/r^3 c) - x \sin(2aGMt/r^3 c) = z \cot s$  surface at time  $t$ . The closer the particles to the rotating gravitating center, the faster their precession. For a given radius  $r$ , the particle motion in an accretion disk can be represented as the rotation of a circumference inclined to the  $z$  spin axis at angle  $s$  with angular velocity  $2aGM/r^3 c$ . In a coordinate system corotating with the circumference, the particle rotates with a Keplerian velocity. Thus, if viscous friction between adjacent orbits is disregarded, a tilted accretion disk cannot be in a steady state.

#### THE ENERGY AND ANGULAR MOMENTUM OF PARTICLES MOVING ALONG GEODESIC ORBITS IN THE KERR SOLUTION ON THE $r = \text{const}$ SURFACES

In this section, for simplicity, we choose a system of units in which  $c = G = M = 1$ . To find stable orbits on the  $r = \text{const}$  surfaces, we must solve the

algebraic equations (8). The corresponding solutions in the  $s = \pi/2$  equatorial plane were found by Ruffini and Wheeler (1970) for  $j = 1$  and by Bardeen *et al.* (1972) for arbitrary  $j$ . For  $s = 0$  and arbitrary  $j$ , the particle angular momentum  $L$  is zero. The corresponding expression for the energy was derived by Lightman *et al.* (1975). *Inclined* orbits were investigated by Wilkins (1972). For charged rotating black holes, the selected tilted bound geodesics were studied by Johnston and Ruffini (1974). Finally, Shakura (1987) derived formulas for the energy and angular momentum at arbitrary  $j$  and  $s$  by a complex, indirect method. Below, we show that deriving expressions for  $E$  and  $L$  from Eqs. (8) can be reduced to solving a quadratic equation and factorizing the numerator and denominator in the resulting fraction (to be subsequently canceled by a common factor).

Let us introduce new unknowns instead of  $E$  and  $L$ :

$$x_c \equiv \frac{E}{L}, \quad y_c = \frac{E^2 - 1}{L^2}. \quad (27)$$

Eqs. (8) can then be written as

$$y_c a_1 + x_c a_2 + (x_c^2 - y_c)(a_1 + a_3) + a_0 = 0, \quad (28)$$

$$y_c b_1 + x_c b_2 + (x_c^2 - y_c)(b_1 + b_3) + b_0 = 0, \quad (29)$$

$$b_i \equiv \frac{\partial a_i}{\partial r} \Big|_{j,s}, \quad i = 0, 1, 2, 3.$$

Here,

$$\begin{aligned} a_0 &= -(r^2 - 2r + \Delta \cos^2 s), \\ a_1 &= r^4 + 2j^2 + j^2 r + j^2 \Delta \cos^2 s, \\ a_2 &= -4jr, \quad a_3 = -p\Delta, \quad p \equiv r^2 + j^2 \cos^2 s. \end{aligned} \quad (30)$$

Eliminating  $y_c$  from Eqs. (28) and (29) yields the quadratic equation

$$\begin{aligned} x_c^2(a_1 b_3 - a_3 b_1) + x_c(a_2 b_3 - a_3 b_2) \\ + a_0 b_3 - a_3 b_0 = 0, \end{aligned}$$

whose solution is given by

$$x_c = \frac{E}{L} = \frac{A + qB}{D \sin s}, \quad q \equiv \sqrt{r - j^2 \cos^2 s/r}. \quad (31)$$

In formula (31), we use the notation

$$\begin{aligned} A &\equiv j \sin s(3r^4 - 4r^3 + j^2 r^2 \cos^2 s(j^2 r^2 - r^4)), \\ B &\equiv rp\Delta, \end{aligned} \quad (32)$$

$$\begin{aligned} D &= -a_1 b_3 + a_3 b_1 = (r^2 - j^2 \cos^2 s) \\ &\times (r^2 + j^2)^2 - 4j^2 r^3 \sin^2 s. \end{aligned} \quad (33)$$

The numerator and denominator in (31) can be factorized as

$$A + qB = r((r^2 + j^2)q + 2jr \sin s) \quad (34)$$

$$\begin{aligned} &\times (j \sin sq + r^2 + j^2 \cos^2 s - 2r), \\ D &= r((r^2 + j^2)q + 2jr \sin s) \end{aligned} \quad (35)$$

$$\times ((r^2 + j^2)q - 2jr \sin s).$$

Therefore, cancelling a common factor in the numerator and denominator in (31), we obtain

$$x_c = \frac{E}{L} = \frac{jq \sin s + r^2 + j^2 \cos^2 s - 2r}{(r^2 + j^2)q - 2jr \sin s}. \quad (36)$$

Multiplying Eq. (28) by  $b_1$  and Eq. (29) by  $a_1$  and subtracting (29) from (28) yields

$$\begin{aligned} x_c^2 - y_c &= \frac{1}{L^2} = \frac{x(a_1 b_2 - a_2 b_1) + a_1 b_0 - a_0 b_1}{D} \\ &= \frac{A_1 + qB_1}{D \sin s}, \end{aligned} \quad (37)$$

$$\begin{aligned} A_1 &\equiv 2jrp(2r^4 - 3r^3 + j^2 r^2 + \cos^2 s j^2 (r - j^2)), \\ B_1 &\equiv p^2(r^3 - 3r^2 + j^2 + j^2 r). \end{aligned}$$

The expression  $A_1 + qB_1$  can also be factorized as

$$\begin{aligned} A_1 + qB_1 &= p((r^2 + j^2)q + 2jr \sin s) \\ &\times (2rjq \sin s + r^3 - 3r^2 + j^2 \cos^2 s(r + 1)). \end{aligned} \quad (38)$$

Hence,

$$\begin{aligned} L &= \sqrt{\frac{D \sin s}{A_1 + qB_1}} \\ &= \frac{((r^2 + j^2)q - 2jr \sin s) \sin s}{\sqrt{p(p - 3r + j^2 \cos^2 s/r + 2jqr \sin s)}}. \end{aligned} \quad (39)$$

Using formula (36) for  $E/L$ , we obtain with (39)

$$E = \frac{p - 2r + jq \sin s}{\sqrt{p(p - 3r + j^2 \cos^2 s/r + 2jqr \sin s)}}. \quad (40)$$

Formulas (39) and (40) are the sought-for expressions for the particle energy and angular momentum in inclined circular orbits.

We determine the coordinate radius of the marginally stable orbit,  $r_*$ , from the condition of  $E$  given by (40) being at a minimum. Representing  $r_*$  as a Taylor expansion in terms of  $j$ , we obtain  $r_*$  as a function of  $j, s$ :

$$\begin{aligned} r_* &\approx 6 - 4\sqrt{\frac{2}{3}}j \sin s + \dots \approx 6 - 3.266j \sin s \\ &- j^2(0.5 + 0.1111 \cos 2s) + j^3(-0.2532 \sin s \\ &- 0.0567 \sin 3s) + j^4(-0.1196 + 0.0206 \cos 2s \\ &+ 0.0162 \cos 4s) + j^5(-0.11 \sin s - 0.02 \sin 3s \\ &+ 0.0025 \sin 5s) \dots \end{aligned} \quad (41)$$

At  $s = 0$ , the first expansion terms for  $r_*$  are

$$\begin{aligned} r_* &\approx 6 - 0.6111j^2 - 0.0828j^4 - 0.211j^6 \\ &- 0.0066j^8 - 0.0023j^{10} + \dots \end{aligned}$$

Substituting the Taylor expansion (41) in (39) and (40) yields Taylor expansions for the binding energy and angular momentum in the marginally stable orbit:

$$\begin{aligned}
1 - E_* &\approx 0.0572 + 0.0321j \sin s + j^2(0.0131 \\
&- 0.0087 \cos 2s) + j^3(0.0143 \sin s - 0.002 \sin 3s) \\
&+ j^4(0.0065 - 0.006 \cos 2s + 0.0003 \cos 4s) \\
&+ j^5(0.0087 \sin s - 0.002 \sin 3s) \dots, \\
\frac{L_*}{\sin s} &\approx 3.4641 - 0.9428j \sin s - j^2(0.1123 \\
&+ 0.1443 \sin^2 s) - j^3(0.1178 \sin s + 0.0175 \sin^3 s) \\
&+ j^4(-0.0138 - 0.0878 \sin^2 s + 0.0138 \sin^4 s) \\
&+ j^5(-0.0327 \sin s \\
&+ 0.0467 \sin^3 s + 0.016 \sin^5 s) \dots
\end{aligned} \quad (42)$$

We supplement expansions (41) and (42) with the values of the corresponding functions at  $j = 1$  numerically constructed by least squares for an arbitrary fixed orbital inclination to the black-hole spin axis:

$$\begin{aligned}
1 - E_* &\approx 0.4222 - 0.8314 \cos^2 s + 0.264 \cos^4 s \\
&+ 0.8605 \cos^6 s - 0.656 \cos^8 s, \\
r_* &\approx 1 + 6.2005 \cos^4 s \\
&- 7.1816 \cos^8 s + 5.1365 \cos^{12} s, \\
L_* &\approx \sin s (1.1876 + 2.5913 \cos^2 s \\
&- 0.9948 \cos^4 s + 0.494 \cos^6 s).
\end{aligned} \quad (43)$$

Note that for  $s = 0$  and  $j = 1$ , the radius of the marginally stable orbit is  $1 + \sqrt{3} + \sqrt{3 + 2\sqrt{3}} \approx 5.2745$  (in units of  $GM/c^2$ ).

#### PERIASTRON AND NODAL PRECESSION OF ORBITS ON THE $r = \text{const}$ SURFACES

Choose the angle  $\theta$  as a parameter on a bounded trajectory. It then follows from (5)–(7) that

$$\begin{aligned}
\frac{d\phi}{d\theta} &= \frac{(2jEr + L(\Delta/\sin^2 \theta - j^2))}{\Delta\sqrt{\Theta}}, \\
-\Theta &\equiv \left( \frac{\sin^2 s}{\sin^2 \theta} - 1 \right) \left( \sin^2 \theta j^2(1 - E^2) + \frac{L^2}{\sin^2 s} \right), \\
\frac{dt}{d\theta} &= \frac{(-2jrL + E((r^2 + j^2 \cos^2 \theta)\Delta + 2r(r^2 + j^2))}{\Delta\sqrt{\Theta}}.
\end{aligned} \quad (44)$$

Expressions (39) and (40) for the energy and angular momentum in circular orbits must be substituted in these formulas for  $E$  and  $L$ .

Integrating the right-hand parts of expressions (44) over  $\theta$  from  $s$  to  $\pi/2$  yields an expression for a quarter of the change in azimuthal angle  $\Delta\phi$  and for a

quarter of the period  $T$  in which the particle runs from a minimum latitudinal angle  $s$  to its maximum  $\pi - s$  and back. The integration result can be expressed in terms of the elliptic functions that contain  $E$ ,  $L$ , and  $s$  as parameters [instead of the constant  $Q$ , we inserted the constant  $s$  into formula (7), which has the meaning of orbital inclination to the black-hole spin axis). Using the notation for the complete elliptic integrals of the first,  $K(k)$ ; second,  $E(k)$ ; and third,  $\Pi(n, x)$ , kinds, we have

$$\begin{aligned}
T &= 4A \left( K(k) \left( jL - j^2E + (Er^2 + Ej^2 - jL) \right. \right. \\
&\times \left. \left. \frac{(r^2 + j^2)}{\Delta} \right) + (K(k) - E(k)) \frac{E}{A^2(1 - E^2)} \right); \\
\Delta\phi &= 4A(L\Pi(-\cos^2 s, k) + j(2rEj - j^2L)K(k)), \\
A &\equiv (L^2/\sin^2 s + j^2(1 - E^2))^{-1/2}; \quad (45) \\
k &\equiv \cos^2 s j^2(1 - E^2)A^2.
\end{aligned}$$

In contrast to Johnston and Ruffini (1974), who first wrote the corresponding formulas in the form of elliptic integrals for any  $j$ , in formulas (45), we inserted explicit expressions for all quantities in terms of the smallest angle  $\theta_- \equiv s$  in the orbit. Expressions (39) and (40) must be substituted for  $E$  and  $L$ , respectively.

For low-eccentricity orbits<sup>4</sup> ( $\delta r = \epsilon \sin \xi$ ,  $\epsilon \ll r$ ), it follows from the Hamilton–Jacobi equation (4) that

$$\begin{aligned}
\frac{d\xi}{d\theta} &= \frac{\sqrt{-R''/2}}{\sqrt{\Theta}}, \quad R'' \equiv \frac{d^2R}{dr^2} \\
&= -2(6(1 - E^2)x^2 - 6x \\
&+ (1 - E^2)j^2 \sin s^2 + \frac{L^2}{\sin^2 s}).
\end{aligned} \quad (46)$$

From Eq. (46) for the periastron rotation frequency  $\nu_r$ , we have

$$\nu_r = \frac{\Delta\xi}{T} = 4A \frac{\sqrt{R''/2}}{T} K(k). \quad (47)$$

Note that the frequencies  $\Delta\phi/2\pi T$  and  $1/T$  are commonly denoted by  $\nu_\phi$  and  $\nu_\theta$ , respectively, so the sought-for nodal precession frequency is  $\nu_{\text{nod}} = \nu_\phi -$

<sup>4</sup>Syer and Clarke (1992) considered the possible existence of stationary disks in the equatorial plane in which the particle orbits were constant-eccentricity ellipses. Clearly, allowance for general-relativity effects will result in the intersection of orbital trajectories in such disks, because the orbital periastron precesses. However, in the Newtonian theory, unstable disturbance modes with a radially variable eccentricity disturbance exist in such disks (Lyubarskij *et al.* 1994). Arbitrary accretion-disk disturbances apparently produce spiral waves in the disk structure (Spruit 1987).

$\nu_\theta$ . The periastron precession frequency of an orbit is  $\nu_{\text{per}} = \nu_\phi - \nu_r$  (Merloni *et al.* 1999).

To clearly present the result, let us derive asymptotic formulas from (45) and (47) in the form of Taylor expansions in powers of  $j$  by taking into account the dependence of the first integrals  $E$ ,  $L$ , and  $Q$  on  $j$  and  $s$  given by formulas (39), (40), and (7).

The constants  $E$  and  $\tilde{L}$  enter into the formulas for  $\Delta\phi$  and  $\Delta T$  via the ratios  $E/\tilde{L}$  and  $(1 - E^2)/L^2, Q/L^2$ . Let us write out the series expansions of these ratios with the accuracy that will be required to calculate the nodal precession frequency  $(\Delta\phi/2\pi - 1)/T$  up to terms of the order of  $j^3$  inclusive:

$$\begin{aligned} \frac{E}{\tilde{L}} &= \frac{r-2}{r^{3/2} \sin s} + j \frac{3r-4}{r^3} \\ &+ j^2 \frac{(r+0.5r^2 + \sin^2 s(8+7r-1.5r^2))}{r^{9/2} \sin s} + \dots, \\ \frac{1-E^2}{L^2} &= \frac{r-4}{r^3 \sin^2 s} + j \frac{8(r-2)}{r^{9/2} \sin s} + \dots, \\ \frac{Q}{L^2} &= \cot^2 s \left( 1 + j^2 \frac{(r-4) \sin s}{2r^3} - \right. \\ &\quad \left. - j^3 \frac{4(r-2) \sin s}{r^{9/2}} + \dots \right). \end{aligned} \quad (48)$$

Using (48), we obtain from expressions (45) and (47) for  $\Delta\phi$ ,  $T$ , and  $\Delta\xi$

$$\begin{aligned} \frac{\Delta\phi}{2\pi} - 1 &= \frac{2j}{r^{3/2}} - \frac{j^2}{2r^3} 3(r-4) \sin s \\ &+ \frac{j^3}{r^{9/2}} (2 - 1.5r + (18 - 7.5r) \sin^2 s) + \dots, \\ \frac{T}{2\pi} &= r^{3/2} + 3j \sin s + \frac{j^2}{4r^{3/2}} \\ &\times (8 + 3r + (24 - 9r) \sin^2 s) + \dots, \\ \left( \frac{\Delta\xi}{2\pi} \right)^2 &= \frac{r-6}{r} + \frac{12j}{r^{5/2}} (r-2) \sin s + \frac{j^2}{r^4} \times \\ &\times \left( \frac{3}{2} r^2 + 15r - 12 - \sin^2 s (r-4) \left( \frac{15}{2} r - 21 \right) \right) \\ &+ \dots \end{aligned} \quad (49)$$

In the limit  $s \rightarrow 0$ , when the spin axis becomes parallel to the tangential plane to the accretion-disk surface, the following formulas hold:

$$\begin{aligned} \frac{\Delta\phi}{2\pi} - 1 &= \frac{2j}{r^{3/2}} + \frac{j^3}{r^{9/2}} (2 - 1.5r) \\ &+ \frac{3j^5}{r^{15/2}} \left( \frac{3}{2} - \frac{7}{4} r + \frac{19}{32} r^2 \right) + \dots, \\ \frac{T}{2\pi} &= r^{3/2} + \frac{j^2}{4r^{3/2}} (8 + 3r) \end{aligned}$$

$$+ \frac{3j^4}{64r^{9/2}} (7r^2 - 48r + 80) + \dots$$

$$\begin{aligned} \left( \frac{\Delta\xi}{2\pi} \right)^2 &= \frac{r-6}{r} + \frac{3j^2}{2r^4} (r^2 + 10r - 8) \\ &+ \frac{3j^4}{32r^7} (-352 + 576r - 286r^2 + 9r^3) + \dots \end{aligned} \quad (50)$$

From formulas (49) for the Keplerian frequency  $\nu_\phi$ , the nodal precession frequency  $\nu_{\text{nod}}$ , and the periastron rotation frequency  $\nu_r$  of a low-eccentricity orbit around the black-hole spin direction, we derive the compact formulas

$$\begin{aligned} 2\pi\nu_\phi &= \frac{\Delta\phi}{T} = \frac{1}{r^{3/2}} \left( 1 + \frac{(2-3\sin s)j}{r^{3/2}} \right. \\ &\quad \left. + \frac{((12+9r)\sin^2 s - 8 - 9r)j^2}{4r^6} + \dots \right); \\ 2\pi\nu_{\text{nod}} &= (\Delta\phi - 2\pi)/T \approx \frac{2j}{r^3} - j^2 \frac{1.5\sin s}{r^{7/2}} \\ &\quad + j^3 \frac{-2 - 3r + (6 + 1.5r)\sin^2 s}{r^6} + \dots, \\ (2\pi\nu_r)^2 &= \frac{r-6}{r^4} + \frac{6j}{r^{11/2}} \sin s (r+2) \\ &\quad + \frac{j^2}{r^7} (12 + 20r - 3\sin^2 s(1+r)(10+r)) + \dots \end{aligned} \quad (51)$$

The first term in the formula for nodal precession was found by Lense and Thirring (1918) (see also Wilkins 1972). In a coordinate system rotating with the frequency  $\nu_{\text{nod}}$ , the Keplerian orbit is stationary.

In the limit  $s \rightarrow 0$ , when the black-hole spin axis becomes tangential to the disk surface, we can derive the following expansions for the nodal precession frequency, the periastron rotation frequency, and the Keplerian meridional frequency from formulas (45) and (47) using (50)<sup>5</sup>

$$\begin{aligned} 2\pi\nu_{\text{nod}} &= (\Delta\phi - 2\pi)/T \approx \frac{2j}{r^3} \left( 1 - j^2 \frac{3r+2}{2r^3} \right. \\ &\quad \left. + j^4 \frac{8 + 54r + 27r^2}{16r^6} + \dots \right), \\ (2\pi\nu_r)^2 &= \frac{r-6}{r^4} + \\ &\quad + \frac{4j^2}{r^7} - \frac{3j^4}{r^{10}} (r^3 + 128r^2 + 172r + 32) + \dots, \\ 2\pi\nu_\theta &= \frac{1}{r^{3/2}} - \frac{j^2}{4r^{9/2}} (3r + 8) \end{aligned} \quad (52)$$

<sup>5</sup>Caution must be exercised when passing to the limit  $s \rightarrow 0$ ; for example, when  $s \rightarrow 0$ ,  $L/(\sqrt{\Theta} \sin^2 \theta) \rightarrow \delta(\sin \theta)$ , where  $\delta(x)$  denotes the Dirac  $\delta$  function.

$$+ \frac{j^4}{64r^{15/2}}(16 + 336r + 15r^2) + \dots$$

To compare formulas (51) and (52) with observations, we should eliminate the radius from them and express the frequencies  $\nu_{\text{nod}}$  and  $\nu_r$  as functions of the Keplerian frequency  $\nu_\phi$ . The functions  $\nu_{\text{nod}}(\nu_\phi)$  and  $\nu_r(\nu_\phi)$  may be said to be given by (51) and (52) in parametric form. An increase in  $\nu_2$  and a decrease in the frequency difference between the two peaks  $\nu_2 - \nu_1$  during observations implies the transition of a radiating clump to an orbit closer to the black hole and the approach of its orbit to the marginally stable orbit. When observations are accumulated, formulas (51) and (52) make it possible to determine the orbital inclination to the spin axis of a slowly rotating black hole or neutron star. When analyzing the energy release in the boundary layer and in an extended disk for a rapidly rotating neutron star, we should take into account the appearance of an intrinsic quadrupole moment that exceeds the Kerr one (see Sibgatullin and Sunyaev 1998, 2000a, 2000b). We emphasize that formulas (51) and (52) are not related to the weak-field approximation and are valid up to the marginally stable orbit.

If the disk lies almost in the equatorial plane of a black hole ( $s = \pi/2$ ), then formulas (51) give Taylor expansions of the formulas by Okazaki *et al.* (1987) and Kato (1990) (see also Merloni *et al.* 1999):

$$\begin{aligned} 2\pi\nu_\phi &= \frac{1}{r^{3/2} + j}, \\ 2\pi\nu_{\text{nod}} &= \frac{1 - \sqrt{1 - 4j/r^{3/2} + 3j^2/r^2}}{r^{3/2} + j}, \\ (2\pi\nu_r)^2 &= \frac{1 - 6/r + 8j/r^{3/2} - 3j^2/r^2}{(r^{3/2} + j)^2}. \end{aligned} \quad (53)$$

#### The Nodal Frequency of the Marginally Stable Orbit for an Arbitrary Orbital Inclination $s$

The following relations (Sibgatullin and Sunyaev 1998, 2000a) hold for the marginally stable orbit in the equatorial plane in a Kerr field, in which the reciprocal radius of the marginally stable orbit acts as a parameter:

$$\begin{aligned} j &= \frac{4\sqrt{x} - \sqrt{3 - 2x}}{3x}, \quad E = \sqrt{\frac{3 - 2x}{3}}, \\ L &= \frac{2}{3\sqrt{3x}}(2\sqrt{x}\sqrt{3 - 2x} + x), \quad x \equiv 1/r. \end{aligned}$$

Let us substitute these expressions in (53):

$$\omega_\phi = \frac{3x^{3/2}}{3 - \sqrt{x}\sqrt{3 - 2x} + 4x},$$

$$2\pi\omega_{\text{nod}} = \omega_\phi(1 + \sqrt{\frac{2}{3}}(\sqrt{x} - \sqrt{3 - 2x})), \quad \nu_r = 0. \quad (53a)$$

If the parameter  $x$  is eliminated from (53a), then we derive the following dependence by least squares:

$$\begin{aligned} \omega_{\text{nod}} &\approx 0.1872(\omega_\phi - \sqrt{6}/36) \\ &+ 1.7246(\omega_\phi - \sqrt{6}/36)^2 + 1.2064(\omega_\phi - \sqrt{6}/36)^3. \end{aligned} \quad (53b)$$

We emphasize that formula (53b) accurately describes the limiting dependence of the nodal precession frequency on Keplerian frequency at  $s = \pi/2$  in the marginally stable orbit over the entire  $\nu_\phi$  range from 1/26 to 0.5, which corresponds to the range of Kerr parameters from  $-1$  to  $1$ . To derive dimensional dependences, we must make the following substitutions in all formulas:  $23.1\omega_{\text{nod}} = \nu_{\text{nod}}(M/1.4M_\odot)$ ,  $23.1\omega_\phi = \nu_\phi(M/1.4M_\odot)$ , ..., where, hereafter, all frequencies are given in kHz.

To determine the nodal precession frequency of the marginally stable orbit for an arbitrary orbital inclination  $s$ , we use formulas (45) in which for  $E, L, r$ , we substitute their expressions in the marginally stable orbit as functions of  $j$  and  $s$ , (41) and (42). Below, we give the highly accurate approximation dependences for the nodal precession frequency and the Keplerian frequency of the marginally stable orbit, in kHz, on the Kerr parameter in the entire  $j$  range ( $-1 \leq j \leq 1$ ) that we derived by analyzing our numerical calculations for various inclinations of this orbit to the black-hole spin axis:

$$\begin{aligned} s = 0: \quad \nu_{\text{nod}}^* &\approx \frac{1.4M_\odot}{M}(0.2139j + 0.0448j^3 \\ &+ 0.0308j^5 + 0.007j^7), \\ \nu_\phi &\approx \frac{1.4M_\odot}{M}(1.5716 + 0.1933j + 0.1539j^2 \\ &+ 0.0712j^3 + 0.0852j^4 + 0.0533j^5); \\ s = 10^\circ: \quad \nu_{\text{nod}}^* &\approx \frac{1.4M_\odot}{M}(0.2139j + 0.0431j^2 \\ &+ 0.0674j^3 + 0.054j^4 + 0.0004j^5 - 0.0414j^6 \\ &+ 0.038j^7 + 0.0432j^8), \\ \nu_\phi &\approx \frac{1.4M_\odot}{M}(1.5716 + 0.3875j + 0.2206j^2 \\ &+ 0.0675j^3 + 0.1681j^4 + 0.1289j^5); \\ s = 30^\circ: \quad \nu_{\text{nod}}^* &\approx \frac{1.4M_\odot}{M}(0.2139j + \frac{0.1394j^2}{1 - 0.82j}), \\ s = 45^\circ: \quad \nu_{\text{nod}}^* &\approx \frac{1.4M_\odot}{M}(0.2139j + \frac{0.1923j^2}{1 - 0.87j}), \\ s = 60^\circ: \quad \nu_{\text{nod}}^* &\approx \frac{1.4M_\odot}{M}(0.2139j + \frac{0.2499j^2}{1 - 0.92j}), \end{aligned}$$

$$s = 80^\circ : \nu_{\text{nod}}^* \approx \frac{1.4M_\odot}{M} \left( 0.2139j + \frac{0.2535j^2}{1 - 0.976j} \right). \quad (54)$$

Note that, in contrast to the preceding formulas, the last two formulas in (54) approximate the numerical data in the range  $-1 \leq j \leq 0.99$ .

The corresponding limiting dependence of the nodal precession frequency on Keplerian frequency for  $s = \pi/6, \pi/4, \pi/3, 4\pi/9$  can be derived from numerical calculations by least squares (here,  $\tilde{\omega}_\phi \equiv \omega_\phi - \sqrt{6}/36$ ):

$$\begin{aligned} s = 30^\circ : \quad & \omega_{\text{nod}} \approx 0.3189\tilde{\omega}_\phi + 0.5205(\tilde{\omega}_\phi)^2 \\ & + 4.37(\tilde{\omega}_\phi)^3, \quad 0.049 \leq \omega_\phi \leq 0.171; \\ s = 45^\circ : \quad & \omega_{\text{nod}} \approx 0.2416\tilde{\omega}_\phi + 1.5953(\tilde{\omega}_\phi)^2 \\ & - 0.2723(\tilde{\omega}_\phi)^3, \quad 0.044 \leq \omega_\phi \leq 0.257; \\ s = 60^\circ : \quad & \omega_{\text{nod}} \approx 0.2031\tilde{\omega}_\phi + 1.7744(\tilde{\omega}_\phi)^2 \\ & + 0.5149(\tilde{\omega}_\phi)^3, \quad 0.041 \leq \omega_\phi \leq 0.414; \\ s = 80^\circ : \quad & \omega_{\text{nod}} \approx 0.1846\tilde{\omega}_\phi + 1.7929(\tilde{\omega}_\phi)^2 \\ & + 1.0862(\tilde{\omega}_\phi)^3, \quad 0.039 \leq \omega_\phi \leq 0.485. \end{aligned} \quad (54a)$$

In formulas (54a), we give the ranges of Keplerian frequencies that correspond to the range of Kerr parameters from  $-1$  to  $+1$ . Consider an example. Let the black-hole mass be  $2.2M_\odot$  and the Keplerian rotation frequency be  $1.2$  kHz. Since the rotation frequency in the innermost Keplerian orbit of a nonrotating black hole with  $M = 2.2M_\odot$  is  $23.1 \times 1.4/2.2 \times \sqrt{6}/36 \approx 1$  kHz,  $\tilde{\omega}_\phi = 0.2 \times 2.2/(1.4 \times 23.1) \approx 0.0136$ . According to (54a), the nodal precession frequency of the marginally stable orbit is:  $\nu_{\text{nod}} \approx 41.1$  Hz for  $s = \pi/2$ ;  $\nu_{\text{nod}} \approx 52.6$  Hz for  $s = \pi/4$ ;  $\nu_{\text{nod}} \approx 65.3$  Hz for  $s = \pi/6$ ;  $\nu_{\text{nod}} \approx 93.6$  Hz for  $s = \pi/18$ ; and  $\nu_{\text{nod}} \approx 123$  Hz for  $s \rightarrow 0$ . We see that the nodal precession frequency significantly depends on the orbital inclination and changes by a factor of 4 as the inclination changes! If the nodal precession frequency is identified with the horizontal-branch oscillation frequency  $\nu_{\text{HBO}}$ , then it becomes possible to determine the inclination of the marginally stable orbit from the known black-hole mass, the Keplerian frequency, and the nodal precession frequency. The figure shows the  $\nu_{\text{nod}} = f(\nu_\phi)$  curves for inclinations  $s = 0, s = \pi/18, s = \pi/6, s = \pi/4, s = \pi/2$ . The frequencies are given in kHz. For an arbitrary mass, the corresponding plots are obtained by stretching the axes by a factor of  $2.2 \times M_\odot/M$ . At  $j \ll 1$ , the nodal precession frequency of the marginally stable orbit is related to the Keplerian frequency by

$$\omega_{\text{nod}} \approx \frac{2}{2 + 9 \sin s} \tilde{\omega}_\phi. \quad (54b)$$

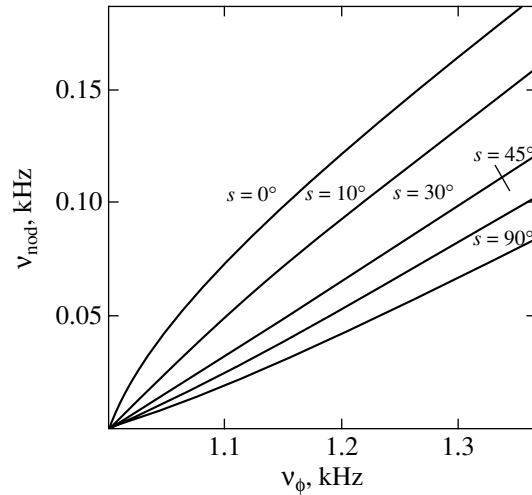


Figure.

At a fixed inclination  $s$ , the precession frequency  $\nu$  in the marginally stable orbit monotonically increases with  $j$  and reaches a maximum at  $j = 1$ . For the mass  $M = 1.4M_\odot$  and  $s = 0$ , it is 296 Hz.

The larger the inclination  $s$  at fixed  $j$ , the larger the precession frequency  $\omega_{\text{nod}}$ . As an illustration, let us write out the approximation formula for  $\nu_{\text{nod}}$  at  $j = 0.998$  [Thorne (1974) number]<sup>6</sup>:

$$\nu_{\text{nod}} \approx 0.29 + 0.7783 \sin s + \frac{17.1094 \sin^6 s}{1 + 1.35 \sin^4 s} \text{ in kHz}. \quad (55)$$

## CONCLUSIONS

According to the ideas explicitly formulated by Bardeen and Petterson (1975) and Bardeen (1977), a geometrically tilted accretion disk is most commonly modeled as a set of rings with the center at the coordinate origin that smoothly turn with changing radius under the effect of viscous torques and gravitomagnetic forces. This approach underlies the existing theories of tilted accretion disks [Papaloizou and Pringle (1983) and Markovic and Lamb (1998, 2000) for small disk deviations from the equatorial plane; Pringle (1992, 1997) for finite disk deviations from the equatorial plane], which are based on a vector equation for the conservation of angular momentum. Some ideas developed by Shakura and Sunyaev

<sup>6</sup>Studying the evolution of a black hole under the effect of disk accretion in the equatorial plane, Thorne adduced arguments that the Kerr parameter cannot be larger than 0.998 in this case when the radiation from inner disk regions is taken into account. Since the black hole mostly captures photons with a negative angular momentum (opposite to the black-hole rotation), the black-hole spinup by disk accretion is counteracted by its spindown via the predominant capture of the photons propagating against the rotation.

(1973, 1976) for flat disks can be used to study the physics of tilted accretion disks. Van Kerkwijk *et al.* (1998) explained the puzzling spindown and spinup of some X-ray pulsars by the fact that the accretion-disk tilt in the inner regions could become larger than 90 degrees!

The effects considered above take place for the inner nonstationary part of the disk, where viscous torques may be disregarded. Matter is not accumulated in the marginally stable orbit because of its instability. In contrast to the statement by Stella *et al.* (1999) that the orbital inclination weakly affects the nodal precession frequency, our detailed analysis shows that this effect is significant. There are probably preferential inclinations of the marginally stable orbits [for the inner orbits of the disk can turn through a finite angle because of the intense radiation (Van Kerkwijk *et al.* 1998)], and there is no need to introduce even harmonics of the nodal frequency to reconcile observations with theory.

#### ACKNOWLEDGMENTS

I wish to thank Prof. Sunyaev, who drew my attention to the problem considered and for fruitful discussions.

#### REFERENCES

1. J. M. Bardeen, W. H. Press, and S. Teukolsky, *Astrophys. J.* **178**, 347 (1972).
2. J. M. Bardeen and J. A. Petterson, *Astrophys. J. Lett.* **195**, L65 (1975).
3. B. Carter, *Phys. Rev.* **174**, 1559 (1968).
4. W. Cui, S. N. Zhang, and W. Chen, *Astrophys. J. Lett.* **492**, L53 (1998); astro-ph/9811023.
5. F. de Felice, *J. Phys. A* **13**, 1701 (1980).
6. W. Israel, *Phys. Rev. D* **2**, 641 (1970).
7. S. Kato, *Publ. Astron. Soc. Jpn.* **42**, 99 (1990).
8. W. Laarakkers and E. Poisson, *Astrophys. J.* **512**, 282 (1999); gr-qc/9709033 (1997).
9. L. D. Landau and E. M. Lifshitz, *The Classical Theory of Fields* (Nauka, Moscow, 1980; Pergamon, Oxford, 1975).
10. J. Lense and H. Thirring, *Phys. Z.* **19**, 156 (1918).
11. A. F. Lightman, W. N. Press, R. H. Price, and S. A. Teukolsky, *Problem Book on Relativity and Gravitation* (Princeton Univ. Press, Princeton, 1975).
12. Y. E. Lyubarskij, K. A. Postnov, and M. E. Prokhorov, *Mon. Not. R. Astron. Soc.* **266**, 583 (1994).
13. V. C. Man'ko, N. R. Sibgatullin, *et al.*, *Phys. Rev. D* **49**, 5144 (1994).
14. D. Markovic, astro-ph/0009450.
15. D. Markovic and F. K. Lamb, astro-ph/0009169.
16. D. Markovic and F. K. Lamb, *Astrophys. J.* **507**, 316 (1998); astro-ph/9801075.
17. A. Merloni, M. Vietri, L. Stella, and D. Bini, *Mon. Not. R. Astron. Soc.* **304**, 155 (1999); astro-ph/9811198.
18. M. Johnston and R. Ruffini, *Phys. Rev. D* **10**, 2324 (1974).
19. Sh. M. Morsink and L. Stella, *Astrophys. J.* **513**, 827 (1999); astro-ph/9808227.
20. A. T. Okazaki, S. Kato, and J. Fukue, *Publ. Astron. Soc. Jpn.* **39**, 457 (1987).
21. J. C. B. Papaloizou and J. E. Pringle, *Mon. Not. R. Astron. Soc.* **202**, 1181 (1983).
22. J. A. Petterson, *Astrophys. J.* **214**, 550 (1977).
23. J. E. Pringle, *Mon. Not. R. Astron. Soc.* **258**, 811 (1992).
24. J. E. Pringle, *Mon. Not. R. Astron. Soc.* **281**, 357 (1996).
25. J. E. Pringle, *Mon. Not. R. Astron. Soc.* **292**, 136 (1997).
26. D. Psaltis, R. Wijnands, J. Homan, *et al.*, *Astrophys. J.* **520**, 763 (1999); astro-ph/9903105.
27. R. Ruffini and J. A. Wheeler, *Bull. Am. Phys. Soc.* **15** (11), 76 (1970).
28. N. I. Shakura, *Pis'ma Astron. Zh.* **13**, 245 (1987) [*Sov. Astron. Lett.* **13**, 99 (1987)].
29. N. I. Shakura and R. A. Sunyaev, *Astron. Astrophys.* **24**, 337 (1973).
30. N. I. Shakura and R. A. Sunyaev, *Mon. Not. R. Astron. Soc.* **175**, 613 (1976).
31. M. Shibata and M. Sasaki, *Phys. Rev. D* **58**, 104011 (1998).
32. N. R. Sibgatullin and R. A. Sunyaev, *Pis'ma Astron. Zh.* **24**, 894 (1998) [*Astron. Lett.* **24**, 774 (1998)].
33. N. R. Sibgatullin and R. A. Sunyaev, *Pis'ma Astron. Zh.* **26**, 813 (2000a) [*Astron. Lett.* **26**, 699 (2000a)].
34. N. R. Sibgatullin and R. A. Sunyaev, *Pis'ma Astron. Zh.* **26**, 899 (2000b) [*Astron. Lett.* **26**, 772 (2000b)].
35. H. C. Spruit, *Astron. Astrophys.* **184**, 173 (1987).
36. L. Stella, astro-ph/0011395.
37. L. Stella and M. Vietri, *Astrophys. J. Lett.* **492**, L59 (1998); astro-ph/9709085.
38. L. Stella, M. Vietri, and Sh. M. Morsink, *Astrophys. J. Lett.* **524**, L63 (1999); astro-ph/9907346.
39. D. Syer and C. J. Clarke, *Mon. Not. R. Astron. Soc.* **255**, 92 (1992).
40. S. Thorne Kip, *Astrophys. J.* **191**, 507 (1974).
41. M. van der Kliss, astro-ph/0001167.
42. M. H. van Kerkwijk, Deeptho Chakrabarty, J. E. Pringle, and R. A. M. Wijers, *Astrophys. J. Lett.* **499**, L27 (1998); astro-ph/9802162.
43. D. C. Wilkins, *Phys. Rev. D* **5**, 814 (1972).
44. M. N. Zaripov, N. R. Sibgatullin, and A. Chamorro, *Prikl. Mat. Mekh.* **59** (5), 750 (1995).

*Translated by V. Astakhov*

## Analysis of IUE Spectra for the Star V1016 Ori

É. A. Vitrichenko\*

*Space Research Institute, Russian Academy of Sciences, Profsoyuznaya ul. 84/32, Moscow, 117810 Russia*

Received June 13, 2001

**Abstract**—We analyze IUE spectra of the star 1016 Ori. Together with previously obtained visible spectra, they have allowed the wavelength range from 1150 to 7000 Å to be studied. Atmospheric parameters of the star were refined:  $\log g = 4.5(1)$ ,  $T_{\text{eff}} = 30000(1000)$  K, and  $\xi_t = 15(5)$  km s<sup>-1</sup>. We measured the equivalent widths of  $\sim 500$  lines and used them to compute the chemical composition. It turned out that the He, B, Mg, P, and S abundances were nearly solar; Ne, Ti, and Cr were overabundant; and C, N, O, Al, Si, Mn, Fe, Ni, and Zn were underabundant. © 2001 MAIK “Nauka/Interperiodica”.

### INTRODUCTION

The IUE satellite obtained  $\sim 100000$  spectra at short wavelengths unobservable from the ground. The IUE data archive is publicly available and is stored in a usable form (ASCII files).

Previously, the chemical composition of the star V1016 Ori has been studied by using visible spectra (Cunha and Lambert 1992, 1994; Vitrichenko and Klochkova 2000). The elemental abundances turned out to be anomalous. For example, the light elements were found to be underabundant by  $\sim 0.3$  dex in both studies. According to Ismailov (1988), the star exhibits a helium overabundance.

It is highly desirable to use IUE spectra to compare the results of spectral analysis for ultraviolet and visible lines.

### SPECTRA AND THEIR REDUCTION

Table 1 provides data on all the spectra of V1016 Ori that we could find in the IUE archive. Columns 1 and 2 list mid-exposure heliocentric Julian dates and IUE numbers, respectively. The cameras used are given in the next column. The SWP camera took spectra in the wavelength range 1150–2000 Å, while the LWR and LWP cameras obtained spectra in the range 1900–3200 Å. Below, the former and latter ranges are called uv1 and uv2, respectively. Column 4 contains dispersions: L denotes low dispersion, 6 Å per pixel; H denotes high dispersion, 0.05 Å per pixel for the SWP camera and 0.2 Å per pixel for the other two cameras. Column 5 gives apertures. The letter L denotes an entrance

aperture in the shape of an ellipse with  $10 \times 20$  arcsec axes, and the letter S denotes a circular entrance aperture 3 arcsec in diameter.

Photometric phases of the star are listed in the next column. Since the minimum begins at phase 0.990, none of the spectra falls within the region of the minimum. The phases are followed by exposures in seconds. In the last column, the letter D marks defective spectra unsuitable for analysis, and the plus sign mark those spectra that were used in the subsequent analysis.

Some of the spectra in Table 1 were used to analyze the interstellar extinction (Franco 1982; Bohlin and Savage 1981) and to investigate boron lines in B-type stars (Profitt 2001). The line equivalent widths in the spectrum of V1016 Ori have not been measured previously.

The spectrum reduction involved averaging two spectra for the uv1 and uv2 ranges. The first and second ranges were filtered with 0.2-Å and 0.4-Å-wide windows, respectively. Numerical experiments show that with this filtering, the spectral resolution decreases only slightly (by 5–10%), but the signal-to-noise ratio increases severalfold. To reduce our spectra to continuum, we measured the observed spectrum at  $\sim 20$  points that were relatively free from spectral lines, calculated an eighth-degree polynomial fit by least squares, and divided the observed spectrum by this fit. The continuum-reduced spectrum was compared in several parts with the synthetic spectrum computed using the STARS software package and corrected by taking into account the differences revealed by this comparison. As a result, the continuum was drawn with an accuracy

\*E-mail: vitrich@nserv.iki.rssi.ru.

**Table 1.** A list of spectra

JD 2440000+	No.	Camera	Dispersion	Aperture	Phase	Exposure, s	Notes
3921.609	03783s	LWR	L	S	0.875	18.7	
3921.612	03783	LWR	L	L	0.875	5.6	
3921.642	04282s	SWP	L	S	0.875	360	
3921.645	04282	SWP	L	L	0.875	6.8	D
4289.437	07990s	SWP	H	S	0.496	360	D
4291.453	08005	SWP	H	L	0.527	270	
4822.368	11252	LWR	L	L	0.641	17.5	
4822.371	11252s	LWR	L	S	0.641	9.7	
4822.377	14667	SWP	H	L	0.641	310	
8518.020	21274	LWP	H	L	0.121	360	
9284.917	49002	SWP	H	S	0.841	2100	+
9284.945	26614	LWP	H	S	0.841	1800	+
9284.976	49003	SWP	H	S	0.842	2100	+
9285.006	26615	LWP	H	S	0.842	2400	+
9425.373	50204	SWP	H	S	0.988	900	D
9777.660	54001	SWP	H	L	0.371	120	

$\sim 5\%$ , which is not enough for it to be used to measure the line equivalent widths. Therefore, we determined a local continuum near each line.

Figure 1 shows a portion of the average spectrum for V1016 Ori (lower curve). The synthetic spectrum (upper curve) computed with the STARSP software package (Tsymbol 1995) is given for comparison. It was computed by using the VALD line list (Kupka *et al.* 1999). Ions and line wavelengths are indicated at the top. The first two digits were discarded. Interstellar ions and wavelengths are given at the bottom with a label IS.

The most interesting observed line is Ly $\alpha$ , which bears no resemblance to the synthetic line. The observed line is much broader and deeper than the synthetic one. This is most likely because the Ly $\alpha$  photons are scattered in the circumstellar medium. The

other Orion Trapezium stars exhibit the same phenomenon, implying that the Ly $\alpha$  photons are scattered in the Orion Nebula rather than in the immediate vicinity of the star.

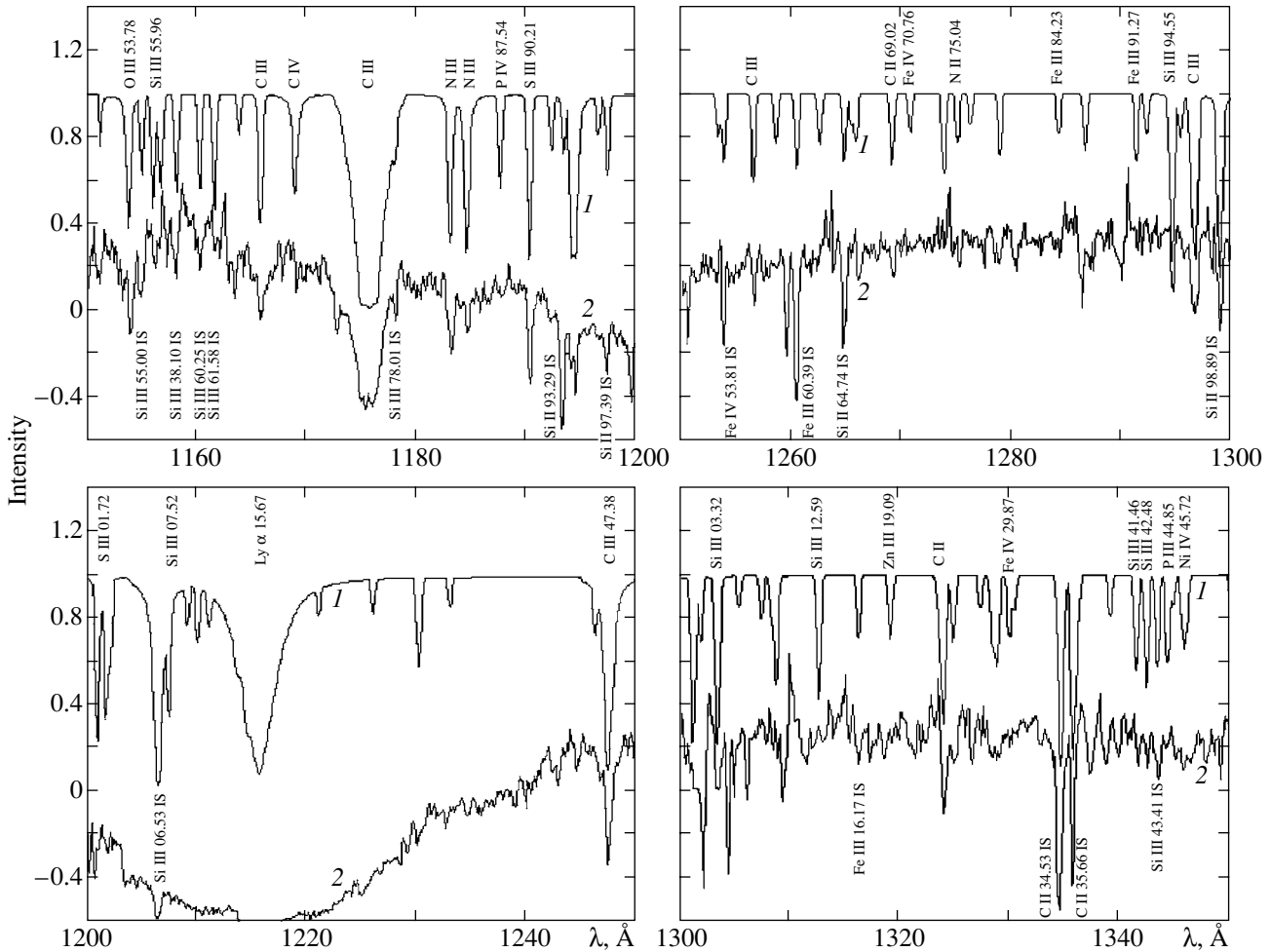
When measuring the line equivalent widths, we singled out a  $\sim 1\text{-}\text{\AA}$ -wide portion of the spectrum centered on the expected line position. Here, two difficulties arise. For the uv1 lines of the star, the mean radial velocity is 39(14) km s $^{-1}$ . The error of a single measurement is given in parentheses. Since the velocity of interstellar lines is 8(11) km s $^{-1}$ , the portion of the spectrum for stellar and interstellar lines had to be centered differently. The second difficulty lies in the large systematic wavelength shift between the uv1 and uv2 spectra, as can be seen from Table 2 and Fig. 2.

Table 2 gives the total number of measured lines for each spectral range. IS mark the columns that refer to interstellar lines. The second row gives the mean continuum level; its deviation from unity characterizes the systematic error, which is seen to be small. The next row gives the parameter of the Gaussian fit to the observed line profile. The error of a single measurement is given in parentheses.

In Fig. 2, the displacement of interstellar lines from laboratory wavelengths is plotted against wavelength. This figure clearly shows an abrupt change

**Table 2.** Statistical data on the uv1 and uv2 ranges

Parameter	uv1 range		uv2 range	
	Star	IS	Star	IS
Number of lines	258	30	85	19
Continuum	0.996		1.002	
$\sigma$ , $\text{\AA}$	0.35(14)	0.32(10)	0.48(21)	0.29(9)
$V_r$ , km s $^{-1}$	39(14)	8(11)	154(19)	115(6)



**Fig. 1.** A portion of the observed spectrum for V1016 Ori (1) and the synthetic spectrum computed with  $T_{\text{eff}} = 30000$  K,  $\log g = 4.5$ ,  $[M/H] = -0.2$ , and  $\xi_t = 15 \text{ km s}^{-1}$  (2). Wavelengths, in Å, and intensities, in fractions of the continuum, are plotted along the horizontal and vertical axes, respectively. The observed spectrum was arbitrarily displaced downward.

in displacement near the boundary of the two spectral ranges. The straight lines were drawn by least squares. The straight line for the uv2 range exhibits an appreciable slope. The equations for these straight lines are

$$\begin{aligned} \Delta\lambda_1 &= 0.043(9) - 0.00004(4)(\lambda - 1150), \\ \Delta\lambda_2 &= 0.86(1) - 0.000211(7)(\lambda - 1900). \end{aligned} \quad (1)$$

Here,  $\Delta\lambda_1$  and  $\Delta\lambda_2$  refer to the uv1 and uv2 ranges, respectively, and the wavelength is given in Å; the errors of the coefficients are given in parentheses.

We see from Eqs. (1) that there is no wavelength dependence of the dispersion for the uv1 range, while for the uv2 range, this dependence is strong. It also follows from these equations that there is a break in the wavelength scale between the two ranges, which for  $\lambda = 1900 \text{ Å}$  is  $0.86 - 0.04 = 0.82(1) \text{ Å}$ . Its most plausible explanation is that the first four points of the uv2 spectrum were missed. The connectedness

of the line measurements within each of the ranges suggests that no points were missed within them.

## REFINING THE ATMOSPHERIC PARAMETERS

We were able to measure  $\sim 300$  lines in the ultraviolet spectra. Since  $\sim 170$  lines were measured in the visible spectra, the total number of lines increased by a factor of  $\sim 3$ , which allows the atmospheric parameters to be reconsidered.

Tables 3–6<sup>1</sup> list the equivalent widths of ultraviolet lines. Table 3 and 4 give, respectively, stellar and interstellar lines in the uv1 range. The interstellar lines differ from the stellar lines in the following. First, occasionally, there are no interstellar lines in

<sup>1</sup>Tables 3–6 are published in electronic form only and are accessible via [ftp://cdsarc.u-strasbg.fr/pub/cats/J\(130.79.128.5\)](ftp://cdsarc.u-strasbg.fr/pub/cats/J(130.79.128.5)) or <http://cdsweb.u-strasbg.fr/pub/cats/J>.

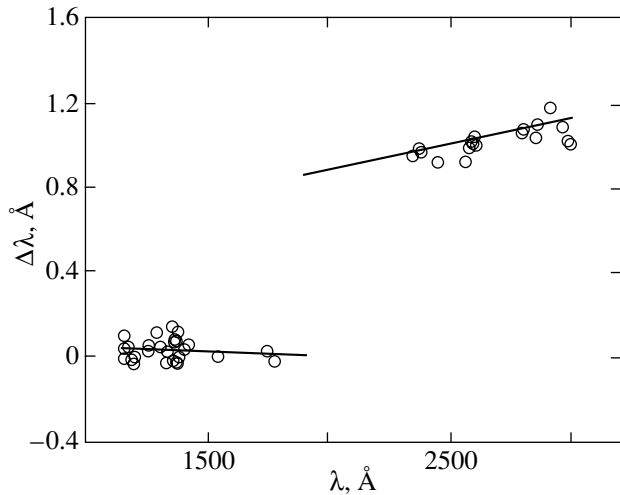


Fig. 2. Wavelength dependence of the interstellar-line displacement from laboratory wavelengths for the uv1 and uv2 ranges.

the synthetic spectrum. Second, the radial-velocity difference between the interstellar and stellar lines is so large (see Table 2) that the line classification is beyond question. Third, the interstellar lines are narrower (see Table 2). Fourth, the interstellar lines often belong to ions with a lower degree of ionization than do the stellar lines. Lists of interstellar lines can be found in Holberg *et al.* (1998). The authors make a note that also pertains to our study: “The identification of features in the IUE echelle spectra is more likely an art than a science.”

Tables 5 and 6 give stellar and interstellar lines in the uv2 range. If a line was rejected as an outlier when computing the chemical composition, a colon is placed near the equivalent width.

We failed to find any circumstellar lines.

Before determining the atmospheric parameters, we carried out numerical experiments aimed at answering the question: How accurate must these parameters be? We chose a grid of models in the vicinity of the atmospheric parameters known from spectroscopic studies and determined the chemical composition for each model from the entire ensemble of line equivalent widths. The problem was formulated as follows: How much does a given atmospheric parameter change so as to obtain a mean change in abundance by 0.1 dex? This is the most typical error.

Our numerical experiments led us to the following conclusions.

Since the elemental abundances computed from lines of species with a lower degree of ionization (e.g., He I, C II, N II, Si III, Cr III, and Fe III) depend weakly on atmospheric parameters, a larger weight must be assigned to these data in an abundance

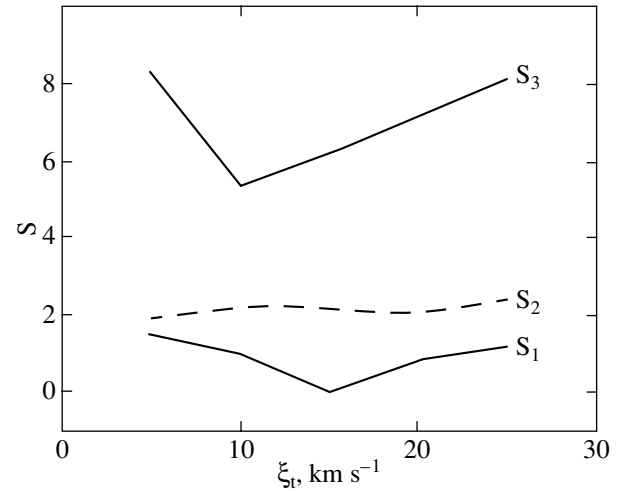


Fig. 3. Functions  $S$  versus microturbulence.

analysis. Conversely, the chemical composition computed from lines of species with a higher degree of ionization (e.g., He II, C III, N III, Si IV, Cr IV, and Fe IV) depend critically on the assumed atmospheric parameters.

Since the chemical composition of the star is anomalous, it would be natural to choose  $\varepsilon_i - \varepsilon_{i+1}$ , the differences between the elemental abundances in two adjacent ionization states, as the criteria that are convenient for refining the atmospheric parameters.

An analysis of these differences allowed us to infer the required accuracy of the atmospheric parameters: the surface gravity, temperature, and microturbulence must be determined with errors no larger than 0.1, 1000 K, and  $5 \text{ km s}^{-1}$ , respectively.

Below, we present the results of our analysis. All models were constructed with  $[M/H] = -0.2$ , which was established in a spectroscopic analysis of the visible spectral range.

**The surface gravity** has previously (Vitrichenko and Klochkova 2000) been estimated from line equivalent widths to be  $\log g = 4.4(2)$ . The discovery of secondary lines (Vitrichenko and Plachinda 2001) has made it possible to determine the masses and radii of the components and, consequently, the surface gravity:  $\log g = 4.6(1)$ . Since the two values are equal, within the error limits, and since the errors themselves are similar, we take  $\log g = 4.5(1)$  in our subsequent calculations. The error is satisfactory.

**The effective temperature.** There is a large set of line equivalent widths for several species, with the line excitation potentials lying within a wide wavelength range. It would be natural to attempt to calculate the effective temperature by using the Boltzmann formula. We performed these calculations and obtained

**Table 7.** Chemical composition of the stellar atmosphere

Species	Sun	Ultraviolet spectral range			Visible spectral range			Entire spectral range		
		[A]	$\sigma$	$N$	[A]	$\sigma$	$N$	[A]	$\sigma$	$N$
He I	-1.05	0.58	0.16	6	-0.15	0.09	8	0.12	0.14	16
He II		0.0	0.3	2	-0.26	0.12	2	-0.1	0.2	4
B III	-9.44	0.2		1				0.2		1
C II	-3.48	-0.1	0.5	5	-0.36	0.03	7	-0.41	0.11	16
C III		-0.03	0.18	10	0.0	0.10	5	0.15	0.14	17
N II	-3.99	-0.3		1	-0.14	0.03	23	-0.19	0.04	28
N III		-0.6	0.5	5	-0.2		1	-0.5	0.4	6
O II	-3.11	0.8		1	-0.29	0.03	52	-0.29	0.04	58
O III		-0.77	0.06	3	0.02		1	-0.58	0.17	4
Ne I	-3.95							0.4		1
Ne II		0.7	0.3	2	0.40	0.07	4	0.55	0.14	6
Mg II	-4.46	-0.06	0.10	2	-0.2		1	-0.08	0.07	3
Al III	-5.57	-0.59	0.19	4	-0.24	0.09	3	-0.43	0.14	7
Si III	-4.49	-0.61	0.12	12	-0.33	0.14	12	-0.45	0.10	24
Si IV		-0.4	0.2	7	0.03	0.10	3	-0.25	0.17	10
P III	-6.59	0.3		1				0.2		1
S III	-4.83	-0.4	0.4	5	0.24	0.14	3	-0.2	0.3	8
S IV		-0.23	0.12	2				-0.18	0.12	2
Ti IV	-7.05	0.8		1				0.9		1
Cr III	-6.37	0.6	0.2	4				0.5	0.2	4
Cr IV		0.5	0.2	4				0.6	0.3	4
Mn IV	-6.65	-0.20	0.02	2				-0.18	0.02	2
Fe III	-4.37	-0.17	0.05	93	0.07	0.04	17	-0.19	0.05	124
Fe IV		-0.46	0.06	78				-0.47	0.07	92
Ni III	-5.79	-0.56	0.11	17				-0.66	0.12	18
Ni IV		-0.31	0.16	13				-0.4	0.2	14
Zn III	-7.44	-0.35	0.06	9	1.04	0.01	2	-0.40	0.09	10

incomprehensible results: the temperature is determined with satisfactory accuracy, but its value lies within the range 40000–50000 K, which is in conflict with the spectrum shape. We leave this result without an explanation.

To determine the temperature using our grid of models, we calculated the following three functions:

$$\begin{aligned}
 S_1 &= |\Sigma(\varepsilon_i - \varepsilon_{i+1})|, \\
 S_2 &= \Sigma|(\varepsilon_i - \varepsilon_{i+1})|, \\
 S_3 &= \Sigma(|\varepsilon_i| + |\varepsilon_{i+1}|).
 \end{aligned}
 \tag{2}$$

The parameter is considered to be properly chosen if all three functions simultaneously reach a minimum. We used a total of nine pairs of species.

The first sum shows the extent to which the abundances determined from two adjacent ionization states disagree. Ideally,  $S_1 = 0$ .

Ideally, the second function is also zero, but here, the outliers of opposite signs are not offset, in contrast to the sum  $S_1$ .

The third sum shows how anomalous the chemical composition is. Clearly, definitely incorrect atmo-

spheric parameters yield a more anomalous chemical composition than do more accurate parameters; therefore, the sum  $S_3$  reaches a minimum at exact parameters.

An analysis of functions (2) shows that  $T_{\text{eff}} = 30000(1000)$  K, which is in good agreement with the spectroscopically determined  $T_{\text{eff}} = 29700(700)$  K. The error is satisfactory. We take  $T_{\text{eff}} = 30000(1000)$  K.

**Microturbulence.** We attempted to determine the microturbulence  $\xi_t$  by a classical method:  $\xi_t$  is chosen in such a way that there is no dependence of the abundance on equivalent width. All attempts of this kind failed: under any reasonable assumptions about  $\xi_t$ , the slope of the straight line is essentially positive.

The method that uses the functions  $S$  proves to be more suitable. Figure 3 shows plots of  $S$  against  $\xi_t$ . An examination of the figure indicates that the function  $S_1$  has a distinct symmetric minimum at  $\xi_t = 15 \text{ km s}^{-1}$ , the function  $S_2$  is flat, and the function  $S_3$  exhibits a clear minimum at  $\xi_t = 10 \text{ km s}^{-1}$ . We take  $\xi_t = 15(5) \text{ km s}^{-1}$ .

## CHEMICAL COMPOSITION

We computed the chemical composition of the star from the equivalent widths of ultraviolet lines and from the set of equivalent widths for the entire spectrum under study. The results of our abundance analysis are presented in Table 7. Also given here for comparison are the results for the visible spectral range.

An examination of Table 7 leads us to conclude that all three abundance determinations are in satisfactory agreement. The number of lines in the last column differs from the sum of the numbers of lines in the two corresponding columns. This difference is associated with the outlier rejection technique. In the first two analyses, a line was rejected if the difference between the abundance derived from this line and the mean abundance derived from all lines exceeded  $2\sigma$ , where  $\sigma$  is the error of a single determination. The last columns give the data that were analyzed by using a less stringent criterion  $2.5\sigma$ , which caused an increase in the number of lines. We rejected  $\sim 5\%$  of all the measured lines.

Below, we make several notes on individual elements.

**Helium.** The He I abundances determined in different spectral ranges differ significantly because of the different outlier rejection techniques used, well-known difficulties in determining equivalent widths, and line saturation. Therefore, the helium abundance is most likely to be nearly solar, as follows from an analysis of the He II lines.

**Boron.** We found one boron line at  $\lambda = 2065.78 \text{ \AA}$  in the spectrum. The boron abundance is nearly solar. This line is peculiar in that its radial velocity is abnormal: it is by  $30 \text{ km s}^{-1}$  lower than the mean velocity for stellar lines. The identification error is highly unlikely, because the line is single and no blends were detected. The paper by Proffitt (2001) is specially devoted to an analysis of boron lines in early B stars.

**Carbon.** For this element, the discrepancy between the abundances determined from two adjacent ionization stages is largest and exceeds the error limits. Carbon is most likely to be underabundant, as inferred from C II, because its abundance depends weakly on atmospheric parameters.

**Nitrogen.** Nitrogen was found to be underabundant from both ionization stages; the abundance determined from N II is more reliable.

**Oxygen** clearly shows a 0.3 dex underabundance, which confirms the result by Cunha and Lambert (1992).

**Neon, titanium, and chromium** exhibit an overabundance by 0.5–0.6 dex. The result is unreliable for titanium, because only one line was measured.

**Magnesium, phosphorus, and sulfur** have solar abundances, but the result is unreliable for phosphorus.

**Aluminum, silicon, manganese, iron, nickel, and zinc** are clearly underabundant. The large zinc overabundance found by Vitrichenko and Klochkova (2000) is an artifact associated with line identification errors.

## CONCLUSIONS

IUE spectra of the star V1016 Ori, together with its previously obtained visible spectra, have allowed us to study the wavelength range from 1150 to 7000  $\text{\AA}$ .

Based on numerical simulations with model atmospheres, we were able to estimate such errors in the stellar atmospheric parameters that led to a systematic error in the abundance by  $\sim 0.1$  dex. These errors for the star in question are: 0.1 for the surface gravity, 1000 K for the temperature, and  $5 \text{ km s}^{-1}$  for the microturbulence.

The atmospheric parameters were refined:  $\log g = 4.5(1)$ ,  $T_{\text{eff}} = 30000(1000)$  K, and  $\xi_t = 15(5) \text{ km s}^{-1}$ .

We measured the equivalent widths of  $\sim 500$  lines and used them to compute the chemical composition. It turned out that the He, B, Mg, P, and S abundances were nearly solar; Ne, Ti, and Cr were overabundant; and C, N, O, Al, Si, Mn, Fe, Ni, and Zn were underabundant.

## ACKNOWLEDGMENTS

I wish to thank the staff of the IUE data archive, who provided the spectra, and V.V. Tsymbal for his STARSP software package. I am grateful to the Vienna VALD Center, which sent a list of ultraviolet lines at my request.

## REFERENCES

1. R. C. Bohlin and B. D. Savage, *Astrophys. J.* **249**, 109 (1981).
2. K. Cunha and D. L. Lambert, *Astrophys. J.* **399**, 586 (1992).
3. K. Cunha and D. L. Lambert, *Astrophys. J.* **426**, 170 (1994).
4. J. Franco, *Astrophys. J.* **255**, 541 (1982).
5. J. B. Holberg, M. A. Barstow, and E. M. Sion, *Astrophys. J., Suppl. Ser.* **119**, 207 (1998).
6. N. Z. Ismailov, *Pis'ma Astron. Zh.* **14**, 327 (1988) [*Sov. Astron. Lett.* **14**, 138 (1988)].
7. F. Kupka, N. E. Piskunov, T. A. Ryabchikova, *et al.*, *Astron. Astrophys.* **138**, 1 (1999).
8. C. R. Proffitt, *Astrophys. J.* **548**, 429 (2001).
9. V. V. Tsymbal, *Astron. Soc. Pac. Conf. Ser.* **108**, 198 (1995).
10. É. A. Vitrichenko and V. G. Klochkova, *Pis'ma Astron. Zh.* **26**, 133 (2000) [*Astron. Lett.* **26**, 104 (2000)].
11. É. A. Vitrichenko and S. I. Plachinda, *Pis'ma Astron. Zh.* **27**, 682 (2001) [*Astron. Lett.* **27**, 581 (2001)].

*Translated by V. Astakhov*

## Surfaces of Zero Kinetic Energy in a General Three-Body Problem

L. G. Luk'yanov\* and G. I. Shirmin

*Sternberg Astronomical Institute, Universitetskii pr. 13, Moscow, 119899 Russia*

Received June 14, 2001

**Abstract**—We generalize the concept of zero-velocity surface and construct zero-kinetic-energy surfaces. In the space of three mutual distances, we determine the regions where motion is possible; these regions are in the shape of an infinitely long tripod. Motions in the three-body problem are shown to be unstable according to Hill. © 2001 MAIK “Nauka/Interperiodica”.

Key words: *celestial mechanics, three-body problem, zero-velocity surfaces, zero-kinetic-energy surfaces*

Solving the three-body problem, just as any other model problem of celestial mechanics, reduces to integrating the system of ordinary differential equations that describe the set of celestial bodies under study. However, the concept of solving the system of equations of motion itself has evolved with time. Since the publication of Newton's book *Mathematical Principles of Natural Philosophy* until the 20th century, the problem had been considered integrable if the general integral of the equations of motion could be expressed in terms of the quadratures of known functions. Only a few problems of celestial mechanics are integrable in quadratures: Kepler's problem, the two-body problem, the photogravitational two-body problem, the problem of two stationary centers, the generalized problem of two stationary centers, the problem of motion in a uniform force field, and the like. The fundamental studies by Bruns, Poincaré, and Painlevé revealed the futility of one-and-a-half-century-long searches for new first integrals of the problem of three or more bodies other than the ten classical integrals representable by algebraic or transcendental single-valued functions. By the beginning of the 20th century, the development of the analytical theory for differential equations had led to a different treatment of integrability: a problem was considered integrable if its general solution could be represented by infinite series converging for given system parameters; the convergence of these series must be absolute and uniform for any real values of time in the entire interval from  $-\infty$  to  $+\infty$ . In the 20th century, attempts were repeatedly made to construct general solutions of the three-body problem in the form of infinite series, including power series of time. These attempts did not produce the desirable result, because

the series had never satisfied the above requirements of absolute and uniform convergence. The principal difficulties were associated with the elimination of the singularities that resulted from possible collisions of gravitating masses. Luck was only on the side of Sundman (1912), who proved the theorem on a general solution of the three-body problem in the form of infinite power series of an auxiliary variable that was similar to time but that regularized pair collisions. Sundman's series have not yet been used in practice, although they give an impeccable (in terms of mathematical rigor) general solution of the three-body problem. The question as to how rapidly these series converge is yet to be explored. On the one hand, as was shown by Belorizky (1933), for a special choice of initial data, Sundman's series converge so slowly that to provide a practically acceptable accuracy requires a portion of the series composed of such a number of terms that is inaccessible to currently available computers. On the other hand, an opposite example is also known: in 1955, Vernik showed that for a different special choice of initial data, the sums of Sundman's series with three significant figures could be calculated in a three-body system by retaining only the first three terms of these series (Balk 1965).

Subsequently, the integrability in celestial mechanics came to be qualitatively treated as the construction of a universal classification of all possible solutions by various properties. It assumes a breakdown of the entire phase space of a dynamical system into several regions containing only the solutions of one class (restricted, periodic, conditionally periodic, asymptotic, and others), which are sought by approximate analytical or numerical methods, if necessary. A characteristic feature of the qualitative methods of celestial mechanics is that their application does not require knowledge of the general solution to the

\*E-mail: ural@sai.msu.ru

equations of motion. In particular, a first integral is widely used to qualitatively analyze the properties of the motion.

The zero-velocity surfaces in a restricted three-body problem were first investigated by Hill in 1878 using the Jacobi integral. The results were published in his fundamental paper on the theory of motion of the Moon (Hill 1905). In his study, he established the possible existence of satellite orbits and orbits bounded by a dumb-bell-shaped surface that enclosed the main bodies and formulated a stability criterion for orbits, which was subsequently called *stability according to Hill*. The zero-velocity surfaces in this problem are called *Hill's surfaces*.

The zero-velocity surfaces have been considered in many other problems. Their analysis in Hill's problem allows the possible existence of satellite motions to be established.

A global qualitative analysis of the general properties of the motion in a two-planet three-body problem was performed by V.G. Golubev (Golubev and Grebenikov 1985). Based on Sundman's famous inequality, V.G. Golubev discovered and studied the class of stable (according to Hill) motions in a two-planet system.

In the problem of two stationary centers, apart from satellite orbits, the zero-velocity surfaces allow restricted motions inside the dumb-bell-shaped region that encloses the two stationary centers to be established. Furthermore, in this case, the motions always take place in some bounded region at negative energy.

The zero-velocity surfaces have a more complex shape in a restricted photogravitational three-body problem (Luk'yanov 1988) and in a restricted variable-mass three-body problem (Luk'yanov 1992). In the photogravitational problem, the families of zero-velocity surfaces at different free parameters admit about a hundred different topological types.

In the two-body problem, the zero-velocity surfaces are very simple. They are concentric spheres with the center in one of the bodies, where the relative motion is always restricted by some sphere at negative energy.

In the general three-body problem, the concept of zero-velocity surface should be replaced by the concept of zero-kinetic-energy surface, i.e., the surface on which the velocities of all three bodies simultaneously become zero. The existence of such surfaces for negative total mechanical energies follows from the energy integral. We know no references in the literature on celestial mechanics to studies of the regions where motion is possible in the general (unrestricted) three-body problem using zero-kinetic-energy surfaces.

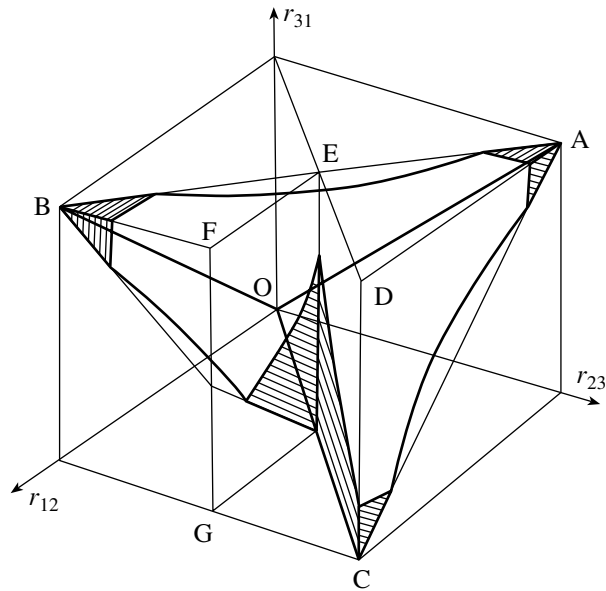


Fig. 1. Zero-kinetic-energy surface.

Constructing zero-kinetic-energy surfaces in the three-body problem in a rectangular (Cartesian) coordinate system involves introducing a nine-dimensional coordinate space for the three bodies. However, the zero-kinetic-energy surfaces can be represented in the three-dimensional space of three mutual distances  $r_{12}$ ,  $r_{23}$ , and  $r_{31}$  between the corresponding bodies  $M_1$ ,  $M_2$ , and  $M_3$ .

Below, we consider a rectangular coordinate system with the  $x$  axis  $r_{12}$ ,  $y$  axis  $r_{23}$ , and  $z$  axis  $r_{31}$ . The part of the space of mutual distances where they are nonnegative and satisfy the following triangle inequalities has the dynamical meaning

$$r_{12} \geq 0, \quad r_{23} \geq 0, \quad r_{31} \geq 0, \quad r_{12} + r_{23} \geq r_{31}, \quad (1)$$

$$r_{23} + r_{31} \geq r_{12}, \quad r_{31} + r_{12} \geq r_{23}.$$

The domain of allowable values (1) in the space of mutual distances is a regular triangular pyramid with an infinite height whose vertex is at the coordinate origin and whose edges are the bisectors of the coordinate planes (pyramid OABC in Fig. 1). The pyramid faces correspond to the arrangement of the bodies on a single straight line; the height corresponds to the arrangement of the bodies at the vertices of an equilateral triangle; and the edges and the coordinate origin correspond to double and triple collisions, respectively.

We write the energy integral in the three-body problem as

$$T - U = h, \quad (2)$$

where  $T$  is the kinetic energy of the system,  $U$  is the force function, and  $h$  is the energy constant ( $h \leq 0$ ).

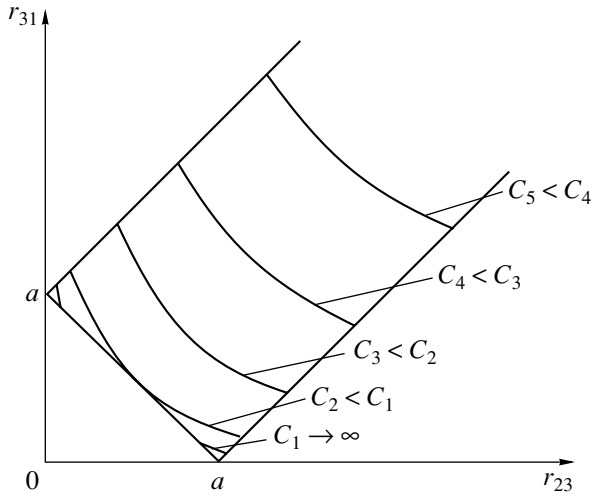


Fig. 2. The sections of zero-kinetic-energy surfaces.

The condition  $T \geq 0$  defines the regions where motion is possible as

$$U \geq C, \tag{3}$$

where

$$U = f \left( \frac{m_1 m_2}{r_{12}} + \frac{m_2 m_3}{r_{23}} + \frac{m_3 m_1}{r_{31}} \right),$$

$f$  is the universal gravitational constant;  $m_1$ ,  $m_2$ , and  $m_3$  are the masses of bodies  $M_1$ ,  $M_2$ , and  $M_3$ , respectively; and  $C = -h$  is an arbitrary constant, which varies over the range  $[0, +\infty)$ .

The zero-kinetic-energy surfaces are

$$F(r_{12}, r_{23}, r_{31}) = f \left( \frac{m_1 m_2}{r_{12}} + \frac{m_2 m_3}{r_{23}} + \frac{m_3 m_1}{r_{31}} \right) = C. \tag{4}$$

The singularities of the family of surfaces (4) are given by the system of three equations

$$\frac{\partial F}{\partial r_{ij}} = -f \frac{m_i m_j}{r_{ij}^2} = 0, \tag{5}$$

where  $i$  and  $j$  take on the values 1, 2, and 3 with  $i \neq j$ .

System (5) has the unique (improper) solution

$$r_{12} = \infty, \quad r_{23} = \infty, \quad r_{31} = \infty. \tag{6}$$

Consequently, if the constant  $C$  is changed from  $+\infty$  to 0 (as was done in the restricted three-body problem when constructing Hill's surfaces), then all surfaces recede from the coordinate origin and from the pyramid edges and contract to an infinitely distant singular point (6) when  $C \rightarrow 0$ .

These surfaces bound the regions where the three bodies can move that are adjacent to the coordinate origin and to the pyramid edges. Figure 1 shows a typical appearance of one of the regions where motion

is possible using the sections by planes that are parallel to the coordinate planes and that pass through points  $A$ ,  $B$ , and  $C$ , as well as the sections by planes  $OCD$  and  $EFG$  (the sections of the region by these five planes are hatched).

It is convenient to represent the entire family of surfaces (4) using the sections by planes parallel to one of the coordinate planes. Consider, for example, the section by plane  $r_{12} = a = \text{const}$ . We then obtain from (4)

$$f m_2 m_3 r_{31} + f m_3 m_1 r_{23} = b r_{23} r_{31}, \tag{7}$$

where  $b = C - f m_1 m_2 / a$ .

This section is a hyperbola, which can be reduced through the transformation  $r_{23} = r'_{23} + \alpha$ ,  $r_{31} = r'_{31} + \beta$  to the form

$$r'_{23} r'_{31} = \gamma, \tag{8}$$

where  $\alpha = f m_2 m_3 / b$ ,  $\beta = f m_3 m_1 / b$ ,  $\gamma = \alpha \beta$ .

Figure 2 shows the sections of the family of surfaces (4) by the  $r_{12} = a$  plane, i.e., hyperbola (7). Not all of the hyperbola but only its part in the domain of allowable values (1) has a physical meaning. Only these parts of the hyperbola are shown in Fig. 2. They lie within the half-band

$$r_{23} + r_{31} \geq a, \quad |r_{23} - r_{31}| \leq a.$$

Similar hyperbolas take place for the sections by the  $r_{23} = \text{const}$  and  $r_{31} = \text{const}$  planes.

For the three-body problem, sections (7) show that the regions where motion is possible are tripods with the vertices at the coordinate origin. Each of the three infinitely long "legs" is adjacent to one of the pyramid edges and is formed by two pyramid faces and surface (4). As the constant  $C$  changes from  $\infty$  to 0, the region where motion is possible changes from the degenerate tripod (of zero volume) formed by the pyramid faces to the entire infinite volume of the pyramid. For  $C \leq 0$ , the motion becomes unrestricted.

We see from Fig. 2 that, in contrast to the restricted three-body problem, the closed surfaces (4) that enclose one, two, or all three bodies do not exist in the general problem. On the contrary, any zero-kinetic-energy surface extends to infinity; therefore, the motions in the three-body problem may be said to be unstable according to Hill.

In the general three-body problem, the zero-kinetic-energy surfaces always allow for the capture and breakup of a close pair and even the exchange — the formation of a new close pair, as well as the recession of one of the bodies to an infinite distance. In this case, double and even triple collisions are possible in principle. Our results are consistent with the classification of final motions by Chazy (1928–1930).

Similar zero-kinetic-energy surfaces exist in the general  $n$ -body problem, but their specific analysis is difficult to perform, because the dimensionality of the space of mutual distances increases. The family of such surfaces also have the only infinitely distant singular point. As  $C$  changes from  $\infty$  to 0, all surfaces monotonically recede from the coordinate origin and contract to an infinitely distant point. For more than three bodies, the motions appear to be also unstable according to Hill.

## REFERENCES

1. M. B. Balk, *Elements of Space Flight Dynamics* (Nauka, Moscow, 1965).
2. D. Belorizky, *J. Obs.* **16**, 109 (1933).
3. J. Chazy, *La théorie de la Relativité et la Mécanique céleste* (Gauthier-Villars, Paris, 1928–1930), Vols. 1, 2.
4. V. G. Golubev and E. A. Grebenikov, *Three-Body Problem in Celestial Mechanics* (Mosk. Gos. Univ., Moscow, 1985).
5. G. W. Hill, *Am. J. Math.* **1**, 284 (1905).
6. L. G. Luk'yanov, *Astron. Zh.* **65**, 1308 (1988) [*Sov. Astron.* **32**, 682 (1988)].
7. L. G. Luk'yanov, *Astron. Zh.* **69**, 640 (1992) [*Sov. Astron.* **36**, 326 (1992)].
8. K. Sundman, *Acta Math.* **36**, 105 (1912).

*Translated by V. Astakhov*